Evaluation and improvement of runoff generation schemes in land surface models for long–term streamflow simulations

AULIA FEBIANDA ANWAR TINUMBANG

2022

Evaluation and improvement of runoff generation schemes in land surface models for long–term streamflow simulations

by

AULIA FEBIANDA ANWAR TINUMBANG

A dissertation submitted in partial fulfillment of the requirement for the degree of Doctor of Philosophy

Department of Civil and Earth Resources Engineering

Kyoto University, Japan

2022

Declaration of authorship

I declare that this thesis, entitled, 'Evaluation and improvement of runoff generation schemes in land surface models for long–term streamflow simulations', and the work presented in it are my own investigation, except where I have consulted the published work of others, this is always clearly attributed. I confirm that this work has not been submitted for a degree or any other qualification at Kyoto University or any other institution.

AULIA FEBIANDA ANWAR TINUMBANG

Acknowledgement

I would like to express my sincere gratitude to Professor Yasuto Tachikawa, Associate Professor Yutaka Ichikawa, Associate Professor Sunmin Kim, Lecturer Kazuaki Yorozu, and Assistant Professor Tomohiro Tanaka from Kyoto University Graduate School of Engineering, as well as Professor Eiichi Nakakita from Disaster Prevention Research Institute, for their kind support, suggestion, and inspiration in order to accomplish this research. In particular, I would like to express my deepest gratitude to Lecturer Yorozu. Since I joined this lab as an undergraduate student, he has been my supervisor. Research work is challenging, but thanks to his great support and guidance, I could enjoy the process of learning. He also patiently taught me how to use all the models I utilized in this study and kindly helped me whenever I had technical difficulties. The completion of my dissertation would not be possible without his expertise, assistance, valuable advice, and encouragement.

I would like to extend my sincere thanks to the Sato Yo Scholarship Foundation. I am incredibly grateful to the Founder, the late Mr. Sato Yo, Representative Director Ms. Masako Fujita, Executive Director Mr. Otsuka Masanori, Ms. Hayashi, Ms. Makino, Ms. Ishikawa, Ms. Yokoi, and all professors in the selection committee. They have supported me financially since I was in the Undergraduate Course until the Doctor Course.

I also would like to express my gratitude to Dr. Tosiyuki Nakaegawa and Dr. Hidetaka Sasaki from Meteorological Research Institute; for providing NHRCM data and its parameters used in this research and for their advice for writing papers. This study has been supported by TOUGOU Program (Integrated Climate Model Advanced Research Program) Theme C and D.

Many thanks to my fellow labmates, alumni, and secretary Ms. Mayumi Iwasa in Hydrology and Water Resources Research Laboratory, Kyoto University. They have supported me greatly and are always willing to help me. I really had a good time since I was assigned to this lab. In particular, the lab trip activity was very fun.

I extend my gratitude to all my colleagues, Ms. Reiko Fujiwara, Prof. Kim Chul–Woo, Prof.

Makoto Kimura, Prof. Junji Kiyono, and all professors in the Undergraduate International Course Program of Civil Engineering Kyoto University. They have guided me since the beginning of my life in Japan and helped me to enjoy student life at Kyoto University.

My life in Japan would have been difficult without my knowledge of the Japanese language. I am grateful to Prof. Taro Iemoto and all my Japanese sensei for teaching me Japanese at Kyoto University. I also want to thank Ms. Tomoko Yoshioka, who always has been helping me learn Japanese since I came to Japan. Without their support, I never thought I could pass the Japanese Language Proficiency Test N1.

Last but not least, I am greatly indebted to my husband, Shota Inoue, for his continued support, encouragement, and understanding when undertaking my research. I also would like to thank all my family in Indonesia, especially my parents, who allowed and supported me to continue studying in Japan. The accomplishment of my study would not have been possible without them.

Abstract

In recent years, many regions worldwide have been affected by unprecedented extreme floods and droughts. The latest assessment report by the Intergovernmental Panel on Climate Change predicts that water–related disasters increase in magnitude and frequency owing to global warming. Previous impact assessment studies sought to project changes in future river discharge using runoff (ROF) output from general circulation models (GCMs) and regional climate models (RCMs). However, many researchers have pointed out that the simulated discharge by runoff from GCMs/RCMs is biased. This bias could be due to precipitation and/or runoff bias. The ROF is estimated using the land surface model (LSM) embedded in GCMs/RCMs. It is necessary to evaluate the performance of LSMs with respect to river discharge, because runoff plays an essential role in river discharge simulation. In addition, it is important to understand the sources of runoff bias in LSMs to enhance model performance. In this study, we aimed to evaluate the runoff generation schemes in LSMs and propose strategies to improve their reproductions of long–term observed streamflow.

The two LSMs utilized in this study were the Simple Biosphere including Urban Canopy (SiBUC) and the Meteorological Research Institute–Simple Biosphere Model (MRI–SiB). Both LSMs have been developed based on a Simple Biosphere (SiB). Sensitivity analysis of runoff characteristics in both LSMs was performed using atmospheric forcing data from MRI-AGCM 3.2S, a GCM with a mesh size of 20 km, and the NHRCM, an RCM with mesh sizes of 5 and 2 km. Numerical experiments for both LSMs were conducted in the upper part of the Ping River Basin in northern Thailand. The basin is one of the main tributaries of the Chao Phraya River. The main dam in the basin is the Bhumibol Dam, which has a total catchment area of approximately 26,400 km^2.

First, we investigated the applicability of runoff generated by both LSMs to streamflow simulation. Comparisons of the water budget showed that the SiBUC tended to estimate higher evapotranspiration and lower runoff than the MRI-SiB. Each LSM generated different runoff

characteristics. The SiBUC estimated higher surface runoff and lower subsurface runoff than the MRI–SiB. Subsurface runoff was the dominant runoff component in the MRI–SiB. Different runoff characteristics impact the simulated streamflow in differing ways. The peak discharge determined by the SiBUC, attributed primarily to surface runoff generation, was produced soon after the peak rainfall. In contrast, peak flow in the MRI–SiB showed a significant delay compared to peak rainfall. As the MRI–SiB is dominated by subsurface runoff, rainwater first infiltrates into soil before it flows into a river, resulting in long lag times. In general, the discharge simulated by the SiBUC was of a higher volume than that simulated by the MRI–SiB because of the higher estimation of runoff. This study showed that even though the same forcing data was imposed on both LSMs, the estimated runoff and simulated discharge differed for each LSM.

We examined the runoff generation schemes in the two LSMs in detail to determine the reasons for the different runoff characteristics. Extensive research on the intercomparison of LSMs has been conducted. Many studies have demonstrated a considerable spread in runoff output among different LSMs. However, it is not clear whether this spread is related to model parameters (such as those that describe soil properties) or model structures (such as governing equations used to describe the processes underlying soil–water flow). Identifying sources of uncertainty is challenging owing to the complexity of and different ways in which runoff generation schemes are described. In this study, we developed an emulation model by including various settings of other models to evaluate their impacts in a controlled manner. Specifically, the MRI–SiB emulation model was developed by incorporating MRI–SiB settings in the SiBUC. The investigation determined the main different settings in both LSMs that affected runoff generation and simulated discharge. We found that by adopting the same soil parameters, model structures, and time integration method for soil schemes, the runoff characteristics from the MRI–SiB can be emulated well by the SiBUC. The findings of this study provide insights into identifying the sources of runoff uncertainty in LSMs.

Next, the simulated discharge forced by the runoff from both the SiBUC and MRI–SiB emulation model was evaluated by comparing it with 30 years of observed river flow data. The two LSMs were forced by the observed rainfall and reanalysis of atmospheric data. For long–term evaluation, the discharge simulated by the SiBUC performed better than the flow estimated by the MRI-SiB to reproduce the monthly observed discharge. In particular, the SiBUC performed well at reproducing the discharge observed during wet years (when annual rainfall is higher than the climatological mean). In contrast, the discharge simulated by the MRI–SiB was better

than the flow estimated by the SiBUC during dry years (when annual rainfall is lower than the climatological mean). Therefore, using some SiBUC settings in the MRI–SiB, and vice versa, could enhance the performance of each model at reproducing the long–term observed river flow.

Table of contents

List of figures

List of tables

Chapter 1

Introduction

1.1 Research background

In recent years, many regions worldwide have been affected by unprecedented extreme floods and droughts. For example, in 2011, Thailand experienced severe flood damage due to continuous intense precipitation in the Chao Phraya River Basin, the main basin in this country. The flood disaster has affected more than 4 million households, with more than 800 deaths (Hydro and Agro Informatics Institute, 2012) and economic losses of approximately 46.5 billion USD (World Bank, 2012). The annual rainfall in 2011 was record–breaking; it was the highest in the country's 61–years record (Thai Meteorological Department, 2011). The extreme rainfall in that year was due to a combination of a strong southeast Asian monsoon between May and October and the previous four tropical storms that brought severe rainfall between June and October (Gale and Saunders, 2013). Komori *et al*. (2012) estimated that the accumulated rainfall during the 2011 rainy season (May–October) was 1439 mm, which was 1.43–fold greater than the climatological–mean rainy season rainfall during 1982–2002. In terms of duration, the 2011–flood was the longest ever in history, with a total span of 158 days (Gale and Saunders, 2013).

The latest report by the Intergovernmental Panel on Climate Change (IPCC, 2021) indicated that the risks of water–related disasters are increasing in magnitude and frequency as the water cycle is intensified due to climate change. Climate change brings more intense rainfall, associated flooding, and intense drought in many regions. Rainfall patterns are also changing owing to global warming. Precipitation is projected to increase in high latitudes, while it is likely to decrease in the subtropics region. Based on observational datasets, the report shows

that emissions of greenhouse gases from human activities are responsible for an increase of 1.1° warming since 1850–1900. It is expected that the global temperature will exceed 1.5° of warming over the next 20 years.

For climate change studies, general circulation models (GCMs) have been utilized as important tools to project future changes in climate and its associated impacts. GCMs are numerical models that simulate the physical processes in the atmosphere, ocean, ice, and land surface, represented by using a three–dimensional grid over the globe. The performance of the models is tested by comparing it with observed climate in the past. And sometimes, they are also compared with the results from other models. Once the models' accuracy has been confirmed, they are used to project the future climate according to some possible scenario. The IPCC issued its Special Report on Emissions Scenarios (SRES) in 2000 (Nakicenovic and Swart, 2000). It described four possible future scenarios, called A1, A2, B1, and B2, which are estimated based on a complex relationship between socioeconomic and range of emissions of greenhouse gases (GHGs) and their driving forces during the 21st century (IPCC, 2000). In 2013, the IPCC proposed new scenarios based on the level of GHGs in the atmosphere at the end of the 21st century, relative to the pre–industrial level. These scenarios are known as Representative Concentration Pathways (RCPs). It consists of four possible scenarios of radiative forcing, varies between 2.6, 4.5, 6.0, and 8.5 watts per square meter (W m^{-2}), which results in different ranges of mean global warming over 1.6, 2.4, 2.8, and 4.3 in 21st century, respectively. These RCPs were used in the IPCC Fifth (IPCC, 2014) and the Sixth Assessment Report (IPCC, 2021).

Although the GCMs have been used extensively to make a projection in the future climate, the information provided by the GCMs usually too coarse to capture regional and local climate processes, particularly in the areas where the climate is highly affected by topography. To deal with those issues, regional climate models (RCMs) are often used to dynamically downscale the GCMs for providing more detailed information at some particular regions. These higher resolution models have provided some advantages, such as they could reproduce locally heavy precipitation events that could not be obtained from the results of GCMs (Sasaki *et al*., 2011).

Among the output of the climate models, runoff data have been extensively used to predict the changes of future river discharge under global warming. For instance, a study by Nohara *et al*. (2006) was performed to investigate the projections of streamflow for 24 major rivers in the world based on the Special Report on Emissions Scenarios A1B scenario. The river discharge was

simulated using runoff output from 19 GCMs, participating under the Program for Climate Model Diagnosis and Intercomparison (PCMDI). A weighted ensemble mean (WEM) was used for the multimodel projections to reduce the models' bias and uncertainty. Their findings show that the results of WEM of the simulated flow could better reproduce the observed river flow, except those artificially controlled rivers (due to dam, irrigation effects, etc.). However, they revealed that it was difficult for an individual model to reproduce the observed historical streamflow, including the runoff bias from the GCMs. The results from river discharge projection at the end of the 21st century indicate that in high–latitude rivers, the discharge increases, and the peak flow is produced earlier due to earlier snowmelts caused by a warmer climate. On the other hand, streamflow tends to decrease for the rivers in Europe to the Mediterranean region and the southern United States.

Another study by Hirabayashi *et al*. (2013) was conducted to project global flood risk under climate change by employing daily runoff data generated by 11 GCMs under Coupled Model Intercomparison Project 5 (CMIP5). Historical simulations from 1850–2005 and future simulations with radiative forcing from 2.6 to 8.5 W m^{-2} during 2006–2100 were performed in their study. Before analyzing future climate simulations, they validated the accuracy of simulated flow forced by runoff from each GCM by comparing it with observed streamflow data from the Global Runoff Data Centre (GRDC) in 32 selected river basins. They found the annual simulated discharge was biased; the predicted discharge about $<$ 50% underestimated the observed streamflow. Even so, they assumed that the changes of frequency of extreme events, such as floods with a relatively long return period (of 100 year), could be illustrated without correcting the bias. In terms of future flood risks, they demonstrate a significant increase in flood frequency in Southeast Asia, Peninsular India, eastern Africa, and the northern half of the Andes. While, in some other regions, flood frequency is projected to decrease. They found that the global exposure to floods would increase depending on the degree of warming scenarios, implying a necessity for adaptation and mitigation strategies before significant warming.

The literature studies, including the two mentioned above, have reported the runoff output from the climate models is inevitably biased. Therefore, the discharge estimated by the runoff from the GCMs/RCMs inherits the bias of the climate models (Hirabayashi *et al*., 2013). Some possible causes might come from the performance of climate models on simulating precipitation and/or runoff. The runoff is calculated by the land surface model (LSM) embedded in the GCMs/RCMs. In the LSMs, runoff is estimated as a difference between precipitation and

evaporation. Since runoff plays an essential role in river discharge projection, it is necessary to evaluate the performance of LSMs with respect to river discharge.

Previous studies, as mentioned above, have also shown a large variability of runoff output among different LSMs embedded in the climate models, causing potential uncertainties in the future projection of river discharge. Different runoff estimations among various LSMs may be caused by different parameterization, representation of physical processes in the model, numerical schemes, etc. To improve the runoff accuracy from the LSM, it is necessary to improve the land surface scheme in the climate models ((Nohara *et al*., 2006). In addition, understanding the underlying physical processes of runoff generation in the LSMs is important to identify the sources of uncertainty in the LSMs (Falloon *et al*., 2011).

1.2 Research objectives

This study aims to evaluate runoff generation schemes in land surface models and propose strategies to improve their long-term observed streamflow reproductions. The objectives of this research are as follows.

- To analyze the differences in characteristics of runoff generated by land surface models forced by atmospheric output from a general circulation model and a regional climate model.
- To examine the applicability of the runoff output by the land surface model forced by the output of each climate model to river discharge simulation.
- To develop a framework for a detailed intercomparison of the land surface models.
- To investigate the runoff generation schemes in the land surface models.
- To conduct sensitivity analysis for considering the impacts of various settings in the land surface models on streamflow simulation.
- To improve the runoff accuracy in the land surface schemes to enhance the reproducibility of long-term observed river flow.

1.3 Composition of thesis

As mentioned earlier, this study aims to evaluate and improve the runoff generation schemes in land surface models for long-term streamflow simulations. This thesis consists of 6 chapters for discussing the objective of this study.

Chapter 2 describes the methodology of this study. As the land surface model is the main topic of this study, the historical development of the land surface models is briefly described. In addition, several intercomparison studies conducted in the past are reviewed. Also, an overall framework of this study is explained. Additionally, information about land surface models, river routing model, study area, observed rainfall and streamflow, and output of climate models used in this study is described.

Chapter 3 analyzes the applicability of runoff generated by land surface models to river discharge simulation. In total, three output datasets from the general circulation model and regional climate model, which vary in horizontal resolutions, were utilized in this study. Before streamflow simulation is performed, precipitation output from each dataset is evaluated with historical observed rainfall. Next, characteristics of runoff output from two land surface models, forced by atmospheric output from each climate model, were investigated. As the forcing data for both LSMs are the same, different runoff estimation indicates different settings in each LSM. Then, simulated discharge by runoff from each LSM is compared with the observed streamflow.

Chapter 4 investigates runoff generation schemes in the land surface models. The intercomparison analysis was performed by developing an emulation model, which enabled an investigation of the effects of various settings in the LSMs. Throughout this analysis, the settings in the LSMs, which have significant impacts on river discharge simulation, could have been identified.

Chapter 5 suggests some strategies for improving the accuracy of runoff from land surface models in reproducing long–term observed river flow. The estimated runoff from the two LSMs, forced by observed hydrometeorological data, was evaluated with respect to observed discharge. Throughout this analysis, the advantages and limitations of each LSM in reproducing the observed streamflow could be identified. Some strategies for improving the reproducibility of the observed streamflow were proposed by adopting some settings of one LSM to another LSM. This study also proposes a future direction for improving the land surface schemes.

Chapter 6 presents the concluding remark of this study.

Chapter 2

Methodology

2.1 Introduction

This chapter briefly introduces the historical development of a land surface model and its recent progress. Several studies about the intercomparison of the land surface models are also reviewed. Finally, a framework for this chapter is also described.

2.2 Historical development of land surface models

Land surface model (LSM) is a numerical model that solves energy and water transfer between land surface and atmosphere. It is one of the important components of climate models for providing a boundary condition in climate models and meso–scales atmospheric models. It controls the partitioning of available energy between sensible and latent heat, and of available water between evaporation and runoff (Pitman, 2003). Following is a brief description of the historical development of the LSMs. Based on the level of complexity of evapotranspiration processes, Sellers *et al*. (1997) classified the evolution of LSMs into three generations, as shown in Table 2.1.

The first LSM implemented in a climate model was proposed by Manabe (1969). A simple energy balance equation is applied in this model. Evaporation is limited by soil moisture below a threshold; if the soil moisture exceeds a certain limit, runoff is generated (saturation–excess runoff). The soil is represented as a single layer, and a constant soil depth and water–holding capacity are applied globally. That parameterization of hydrology is widely known as the ”Manabe bucket model”. Sellers *et al*. (1997) described the LSM proposed by Manabe (1969) is

Table 2.1: Classification of land surface models based on Sellers *et al*. (1997).

Generation	Characteristics	Example of LSMs
First	Use a simple energy balance equation, globally uniform soil depth and water–holding capacity, soil is represented as a single layer, runoff is treated as saturated–excess runoff, no representation of vegetation, heat conduction into soil is ignored.	”Bucket model” (Manabe, 1969)
Second	Explicit representation of vegetation and its role: including transpiration, canopy interception, etc. More complex hydrological process: soil hydrology scheme is based on Richards equation; soil–water movement is estimated based on Darcy’s Law; infiltration–excess runoff is also considered.	BATS (Dickinson, 1983) SiB (Sellers *et al*., 1986) SSiB (Xue *et al*., 1991) CLM (Dai *et al*., 2003)
Third	Explicit representation of carbon cycle: by integrating stomatal conductance and photosynthesis schemes into the LSMs.	MOSES (Cox *et al*., 1999)

included as the first–generation models. These models do not explicitly represent vegetation schemes and their roles. That oversimplification of evapotranspiration schemes is one of the significant limitations of these models (Sellers, 1992). In addition, the first–generation models may also be inadequate to capture diurnal to multi–annual scales of temperature variations, as heat conduction into the soil is neglected in these models (Pitman, 2003).

The work by Deardorff (1978) has shown a breakthrough in land surface modeling by introducing a method for explicitly simulating soil temperature and moisture in two layers, and vegetation in a single layer that shielded a fraction of ground from solar radiation (Pitman, 2003). Sellers (1997) describes those LSMs that includes a Deardorff (1978)–type model of vegetation being as second generation, including the Biosphere Atmosphere Transfer Scheme (BATS; Dickinson *et al*., 1983), the Simple Biosphere Model (SiB; Sellers *et al*., 1986), the Simplified Simple Biosphere Model (SSiB; Xue *et al*., 1991), and the Community Land Modeling (CLM; Dai *et al*., 2003). Major innovations of the second–generation LSMs include an explicit representation of vegetation and its roles, such as treatment of transpiration, canopy interception, and the impacts of canopy conductance on momentum transfer. The treatment of hydrology processes has also become more complex than the first–generation schemes. For example,

explicit representation of various soil types; soil scheme is implemented based on Richards equation, replacing the simple bucket model of Manabe (1969); vertical water transfer within the soil layers is described following Darcy's Law; and infiltration–excess runoff is also considered for estimating the runoff. The improvement in evaporation, soil temperature, and soil moisture representations in the second–generation models have provided a means to explore the impacts of land cover change (Pitman, 2003).

The third–generation models are identified by the method used to model the carbon cycle. The canopy conductance introduced in the second–generation models was recognized as a means to improve evapotranspiration schemes, address the issue of carbon uptake by plants and its structural response, and capture the impact of increasing carbon dioxide. Stomatal conductance and photosynthesis schemes into the LSMs represent a fundamental advance in LSMs for estimating the feedbacks of increasing carbon dioxide in climate simulations. The increasing carbon dioxide influences the canopy conductance, and the vegetation can respond structurally by growing different leaves or taller trees (Pitman, 2003). Despite this, other processes, such as soil hydrology, soil temperature, etc., are treated similarly to the second–generation schemes. Met Office Surface Exchange Scheme (MOSES; Cox *et al*., 1999) is one of the LSMs that belongs to this group.

Pitman (2003) describes that although the above–ground processes in the LSMs (e.g. the evapotranspiration schemes) has been well developed, the modeling of the below–ground processes (e.g. soil hydrology) are still too simplified. As the two components are linked via root–uptake, improving the hydrological representation in the LSMs is necessary, because the errors in the hydrological processes inevitably cause errors in the surface energy balance simulation.

2.3 Intercomparison studies of land surface models

Land surface processes in climate models have evolved from a very simple, implicit approach representing the surface energy balance and hydrology (Manabe, 1969) to complex models that explicitly represent many of the key processes in the land surface (Pitman, 2003). Numerous land surface schemes vary in detail and complexity and have been developed by various institutions. Intercomparison of the land surface models are useful to assess the sensitivities of the wide range of and improve the land surface schemes (Henderson–Sellers *et al*., 1995).

Extensive studies have been done on the intercomparison of land surface models. They have

shown a large spread among different LSMs in terms of their partitioning of surface energy between latent and sensible heat flux and precipitation between runoff and evapotranspiration when driven with the same meteorological forcing (Koster and Milly, 1997). Some efforts have been done to bring the land surface community together to understand why various LSMs perform differently, including Global Land–Atmosphere System Study (GLASS, http://hydro.iis.u-tokyo.ac.jp/GLASS/), The Project for Intercomparison of Landsurface Parameterisation Schemes (PILPS; Henderson–Sellers *et al*., 1995), and the Global Soil Wetness Project (GSWP; Dirmeyer *et al*., 1999).

Numerous studies on the intercomparison of LSMs have been conducted by different methods and purposes. For example, a study by Koster and Milly (1997) aimed to analyze the sources of variability in LSM behavior, targeting 16 LSMs participating in the PILPS. The results of this project have shown that different LSMs driven by the same forcing can produced significantly different surface energy and water budgets, even when some key aspects of the LSMs (vegetation cover, albedo, turbulent drag coefficient, and snowcover) are carefully controlled (Pitman *et al*., 1993). To understand why these differences happened, they employed a monthly water balance model (MWBM) as a tool for understanding the differences in evaporation rates by each LSM and how the interplay between evaporation and runoff formulations affects simulated soil water dynamics. The MWBM performs no energy balance calculation; the only prognostic variable is the amount of soil moisture in the root zone. The model is forced with monthly total precipitation; some of its amounts reduce as interception loss, the remainder infiltrates the soil. The root zone soil moisture increases with the infiltration, but it decreases through evaporation, which represents the sum of transpiration and bare soil evaporation. Some of the infiltrated water is calculated as root–zone drainage. By fitting the parameters in MWBM for each LSM, they successfully reproduced the annual and seasonal water balances of the 16 LSMs. They showed that the differences in evaporation estimation among LSMs are due to differences in the interception loss rates and the functional relationships between root-zone soil moisture, transpiration efficiency, surface runoff, and root–zone drainage generation. One advantage of their method is that it can be applied without detailed knowledge of individual LSM formulations. However, it is also the limitation of this method; the parameters fitting of the WMBM can not be used for the physical interpretation of each LSM. The MWBM only captures that the transpiration and runoff rates increase with increasing soil moisture in a given LSM. Therefore, they emphasized that understanding the interaction between evaporation and runoff processes in an

LSM, such as how runoff processes affect soil moisture, is critical for understanding the LSM's behavior.

Another study by Oki *et al*. (1999) focuses on the assessment of the accuracy of runoff generated by 11 LSMs participating under the GSWP project. Offline simulations were performed by the LSMs using observed hydrometeorological data. The runoff estimated by the LSMs was translated into river discharge by a river routing model TRIP (Total Runoff Integrating Pathways (TRIP; Oki and Sud, 1998). Then, the simulated discharge was evaluated by comparing it with observed streamflow at 250 stations in 18 river basins worldwide, including the Chao Phraya, the Amazon, the Mackenzie, and the Mississippi. They found that the estimated runoff by the LSMs tends to underestimate the annual observation, which is mainly due to the precipitation forcing. For instance, inadequate quality of the rainfall data, weaker intensity, and continuous precipitation due to disaggregation of monthly precipitation into six–hourly data; small density of rain gauges in some catchment; etc. They also pointed out inadequate parameters or structures of the LSMs, such as processes of groundwater movement, agricultural usage of river water, etc., may also cause errors. However, that topic is beyond the scope of their study.

A study by Mueller *et al*. (2016) had been conducted to examine the behaviour of LSMs for generating surface runoff in case of intense rainfall events. That issue is important because an accurate estimation of surface runoff depends on reliable schemes of infiltration and redistribution of water throughout the soil profile. They performed two infiltration experiments using 3 LSMs: the Soil Water Air Plant (SWAP; van Dam, 1997), Carbon and Hydrology–Tiled ECMWF Scheme for Surface Exchange over Land (CHTESSEL; Balsamo, 2009), and Joint UK Land Environment Simulator (JULES; Best *et al*., 2011). In LSMs, when the rainwater reaches the ground, it is split into water available to infiltrate –maximum infiltration rate, and the surface runoff. The maximum infiltration rate is used as the top boundary condition for a one–dimensional (vertical) water redistribution solution in the soil column below the surface. The models used in their study differ mainly in the maximum infiltration rate definition: in SWAP, it is defined as flux or head controlled; in CHTESSEL, it is calculated as an effective depth of surface runoff for the first 50 cm of the soil; and in JULES, saturated hydraulic conductivity is multiplication and a factor that depends on tile types (land–use types). All the LSMs discretize the spatial derivative in the Richards equation for updating the soil moisture in the next step by using central finite difference, which is a non–monotone method and is prone to produce non–physical spurious oscillations in the solution. In each LSM, six mesh dependence studies were per-

formed by changing the vertical resolution of the soil column, with a total depth of 2m. The grid size varies from uniform 1cm to 5cm, 10cm, 20cm, 50 cm, default JULES setting (10cm, 25cm, 65cm, and 100cm), and default CHTESSEL setting (1cm, 2cm, 4cm, 8cm, 10cm, 25cm, 50cm and 100cm). All simulations were run over one day, with a timestep of 1s to avoid numerical instabilities. In the first experiment, intensive rainfall was represented as a step function of 1000 mm day^{-1} over 0.1 days, and in the second, constant intensive rainfall of 1000 mm day^{-1} was considered. These types of discontinuities problems are challenging for the numerical solvers. When the soil is characterized with hydraulic conductivity that is higher than the rainfall, they found that the solution on the coarse uniform mesh using SWAP ($>$ 10cm mesh) and JULES ($>$ 5cm mesh) is prone to non–physical oscillations. The interpolation of hydraulic conductivity K between the soil layers may cause those oscillations: in SWAP and JULES, K is averaged by the arithmetic mean method, while in CHTESSEL, it is computed using the maximum soil moisture of the two cells. An and Noh (2014) has shown that simple averaging methods (e.g. arithmetic, geometric) may produce unacceptably large errors on coarse grids owing to the high non–linearity of the hydraulic conductivity. In contrast, the upwinding approach used for computing K in the CHTESSEL, can avoid oscillations on the coarse grid while providing a similar solution to the other models in finer grids. They also pointed out that infiltration representation in JULES did not allow for the gradual increase of surface runoff, unlike the other two models. That is because the maximum infiltration rates in JULES are solely based on saturated hydraulic conductivity. The infiltration rate should represent the gradually developing runoff in rainfall on initially unsaturated soil. They suggest that treatment of maximum infiltration rates in JULES can be revised by considering the soil moisture content.

In this section, several intercomparison studies of LSMs with various methods and purposes have been reviewed. As it can be seen, performing the intercomparison of LSMs study is helpful to analyze the model behavior, and to identify a direction for improvement, such as shown in the study by Mueller *et al*. (2016).

2.4 Framework of this study

2.4.1 Introduction

As mentioned earlier, this study aims to evaluate and improve the runoff generation schemes in land surface models for long–term streamflow simulations. The overall framework of this

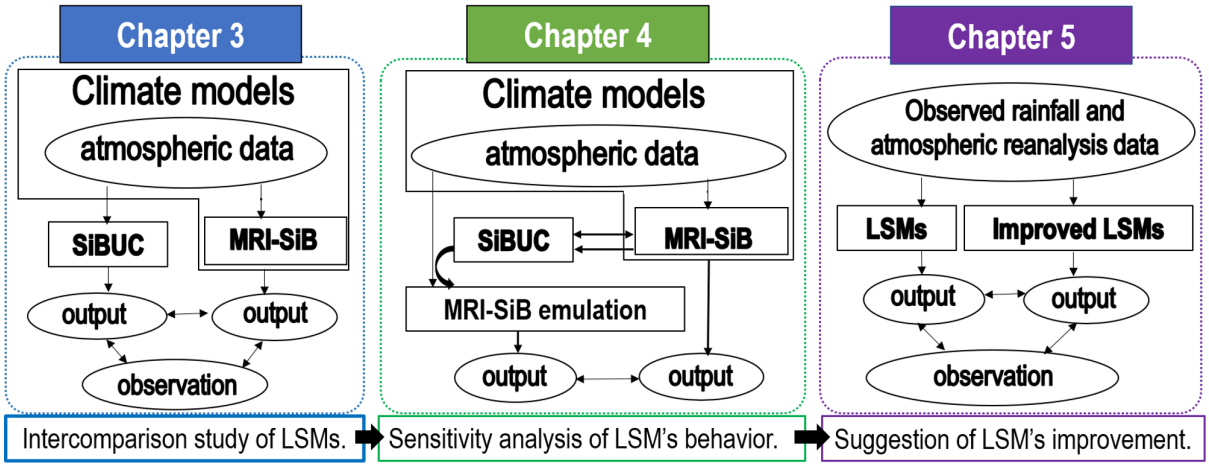

Figure 2.1: Framework of this study.

study is shown in Figure 2.1. The main contents of this study are described in Chapter 3 until Chapter 5. In chapter 3, the main topic is an intercomparison study to analyze the applicability of runoff generated by land surface models to river discharge simulation. This chapter aims to analyze how much the spread of output between two land surface models. The atmospheric forcing used for both LSMs is obtained from the output of climate models. Next, in chapter 4, some possible reasons why such differences happen are investigated by carrying out sensitivity analysis to investigate the LSM behavior on runoff estimation. Previous study has pointed out that it is extremely challenging to analyze the sources of variability in LSM behavior due to the complexity of the interactions among components (Kally and Milly, 1997). This study addresses such problem by developing an emulation model of one LSM by using another LSM so that a process–by–process comparison can be conducted to quantify each component's contribution to the disparity. Similar to chapter 3, atmospheric data from the output of climate models are used as forcing data. In chapter 5, the performance of both LSMs is evaluated by comparing their output with observation data. Observed rainfall and reanalysis atmospheric data are used as forcing for the LSMs. The advantages and limitations of each LSM for reproducing the observation are investigated in this chapter. Based on this analysis, some strategies for improving their performance are proposed.

Description of land surface models, flow routing model, study area, observation, and output of climate model datasets used in this study are presented below.

Table 2.2: Comparison of SiBUC and MRI–SiB.

Differences	SiBUC	MRI–SiB
Base model	SiB version 2 (Seller *et al.*, 1996)	SiB version 1 (Seller *et al.*, 1986)
Water body	considered	not considered
Urban canopy	considered	not considered
Vegetation layer	1 layer (canopy)	2 layers (canopy and ground cover)

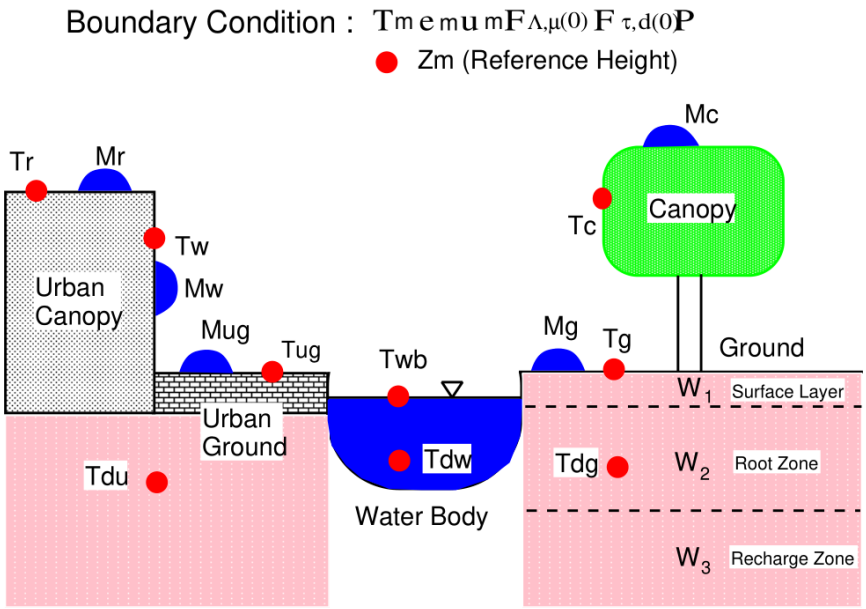

Figure 2.2: Schematic figure of SiBUC. *Courtesy of SiBUC manual*.

2.4.2 Land surface models

Two LSMs were used in this study: Simple Biosphere Model including Urban Canopy (SiBUC; Tanaka *et al.*, 2005) and Meteorological Research Institute–Simple Biosphere (MRI–SiB, Hirai *et al*., 2007).

SiBUC is a land surface model which implements a mosaic scheme that can consider a mixture of land use, paddy field, and irrigation system in the model. In SiBUC, land use is separated into three categories: green area, urban area, and water body, as shown in Figure 2.2. The green area model was developed based on Simple Biosphere (SiB) scheme version 2 (SiB2; Seller *et al.*, 1996).

MRI–SiB is a land surface model developed by Meteorological Research Institute, Japan

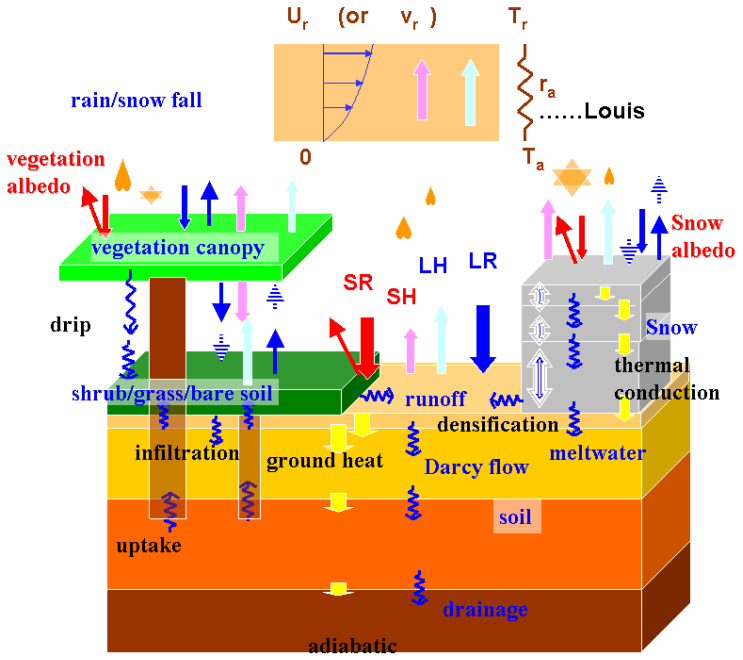

Figure 2.3: Schematic figure of MRI–SiB. *Courtesy of Team GW of Meteorological Research Institute www.mri-jma.go.jp/Project/1-21/1-21-2/Land_Surface_Processe_en.html).*

Meteorological Agency based on the original version of a SiB (Seller *et al.*, 1986; Sato *et al.*, 1989). This model is embedded in the climate models developed by Meteorological Research Institute. Schematic figure of MRI–SiB is shown in Figure 2.3. Several versions of the MRI–SiB has been developed by the MRI; this study utilized the ”SiB0109” version.

Some of the differences between these two LSMs are shown in Table 2.2. As both LSMs have been developed based on similar schemes of SiB, the basic structures are the same; for example, soil water movement is described by three soil layers utilizing a simplified Richards equation in both models. However, as two of them have been developed independently by the different institutions, detail structures, calculation methods, soil parameters, etc., are different. For example, vegetation schemes are treated differently in both LSMs. MRI–SiB has two vegetation layers for canopy and ground cover. While, in the green area model in SiBUC, the number of vegetation layers is reduced to only one, following SSiB (Xue *et al.*, 1991) and SiB2 (Sellers *et al.*, 1996), in order to adopt iterative photosynthesis–conductance model and for incorporating satellite data to describe surface parameters. The differences between the two LSMs will be described in detail in Chapter 4 of this thesis.

2.4.3 Flow routing model

A flow routing model is required to simulate river discharge by using runoff output from the land surface models. This study utilized a distributed flow routing model 1K–FRM, developed based on one–dimensional kinematic wave theory. The source codes and the manual operation are opened to the public on the webpage of Hydrology and Water Resources Research Laboratory Kyoto University.

A coupled of a land surface model SiBUC and a flow routing model 1K–FRM (Yorozu and Tachikawa, 2015) is used in this research. By using this coupled model, the effect of interaction between flow routing and land surface processes could be investigated.

2.4.4 Study area

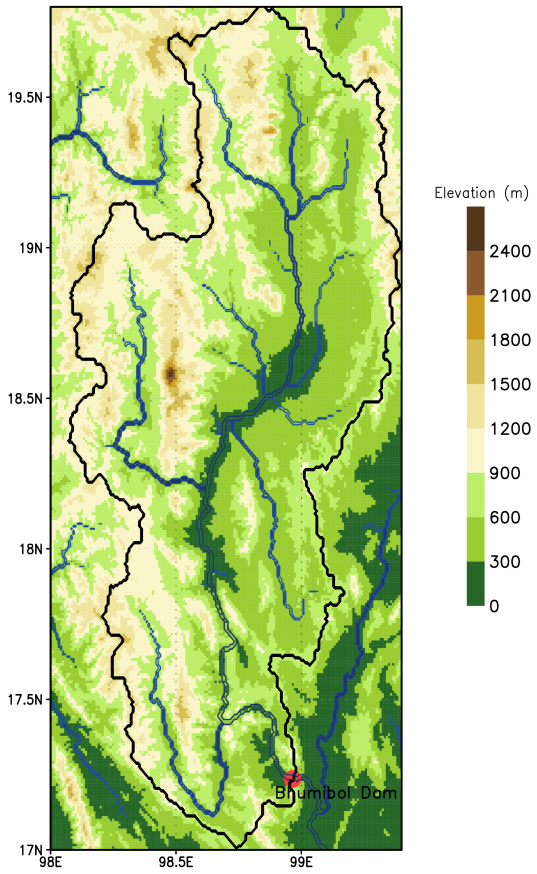

Figure 2.4: Elevation (m) in the upper part of the Ping River Basin. Black line represents the basin boundary. Red circle shows the Bhumibol Dam location.

Table 2.3: Climate model output datasets used in this study.

Climate model	Present climate simulation
MRI–AGCM 3.2S with 20km mesh size	1979–2003
NHRCM with 5km and 2km mesh size	1980–1999

The target area of this study is the upper part of the Ping River Basin, in the northern part of Thailand, as shown in Figure 2.4. The total catchment area of the dam is about 26,400 km^2. The main dam in Ping River, named Bhumibol Dam, was completed in 1964. Bhumibol Dam catchment is located in 98—99.5°E, 17—19.9°S. It was built mainly for the purpose of water resources, hydroelectric power production, and flood control.

Ping River is one of the major tributaries of the Chao Phraya River system. Chao Phraya River basin, which covers about 30% of land area in Thailand, is considered the most important basin in Thailand.

2.4.5 Observation data

This study used observation of rainfall, atmospheric reanalysis, and streamflow data. For rainfall data, the dataset from Climate Hazards Group InfraRed Precipitation with Station data (CHIRPS; Funk *et al.*, 2015) was utilized. CHIRPS is a quasi–global satellite data product with in–situ station rainfall data. We selected this gridded rainfall data because it has a very high spatial resolution of 0.05°. This dataset has a daily time step, and it is available from 1981 to the near–present.

In addition to rainfall, other atmospheric data, such as air temperature, air pressure, humidity, short and longwave radiation in the downward direction, and wind speed, are required for LSMs' forcing. This study obtained those atmospheric reanalysis data from JRA–55 (Kobayashi and Iwasaki, 2016). This dataset has 60–km spatial resolution and 3–hour temporal resolution.

For streamflow data, observed daily inflow at the outlet of Bhumibol Dam was utilized. The observation data was obtained from the Electricity Generating Authority of Thailand (EGAT).

2.4.6 Climate model output datasets

In this study, output dataset from an atmospheric general circulation model MRI–AGCM 3.2S (Mizuta *et al*., 2012) and a regional climate model Non–Hydrostatic Regional Climate Model

(NHRCM; Sasaki *et al*., 2008) were utilized. Summary of climate model output datasets utilized in this study is shown in Table 2.3. Both climate models were developed by Meteorological Research Institute. MRI–AGCM 3.2S has a very high horizontal resolution of 20–km, enabling the simulation of large–scale phenomena associated with small–scale orography, such as tropical cyclones and other localized phenomena (Mizuta *et al*., 2012). The model is developed based on the Japan Meteorological Agency (JMA)'s operational weather prediction model, implementing quasi–conservatives semi–Langrangian dynamics, a radiation scheme, and a land surface scheme. Yoshimura scheme is used for parameterization of cumulus convection in the model. The present and future climate simulation was performed using observed sea surface temperature (SST) and projected SST by atmosphere–ocean coupled models as lower boundary conditions. They have shown that this high–resolution model shows an excellent performance in simulating heavy monthly–mean precipitation around the tropical Western Pacific, the global distribution of tropical cyclones, the seasonal cycle of East Asian summer monsoon, and so on. This model has been developed under the Innovative Program of Climate Change Projection framework for the 21st Century (KAKUSHIN), supported by the Ministry of Education, Culture, Sports, Science, and Technology (MEXT). The output dataset of the present climate simulation by the MRI–AGCM 3.2S (SPA experiment) was utilized for this study. It consists of 25–years of simulation results, ranging from 1979 until 2003.

Another climate model output dataset used in this study was obtained from NHRCM. NHRCM was built based on an operation Non–Hydrostatic Model (NHM), developed by the Meteorological Research Institute and the Numerical Prediction Division of the Japan Meteorological Agency. A land surface scheme MRI–JMA Simple Biosphere model is embedded in the NHRCM for describing the biosphere process, surface temperature, and snow depth. Parametrization of cumulus convection in this model is based on Kain and Fritsch scheme. A preliminary experiment was conducted to evaluate the performance of the model (Sasaki *et al*., 2008). The NHRCM, with a grid interval of 10 km, was nested in the Regional Analysis dataset, and a 4 km mesh size NHRCM was nested in it. They found that the NHRCM could well reproduce the monthly precipitation, seasonal change and observed rainfall's regional features obtained from the AMeDAS dataset. Another study by Sasaki *et al*. (2011) also analyzed the performance of NHRCM with 5km spatial resolution, applied in Japan. The results showed that the annual mean surface temperature and precipitation agreed with the observed data. In addition, it also could reproduce heavy precipitation events which could not be obtained from the results

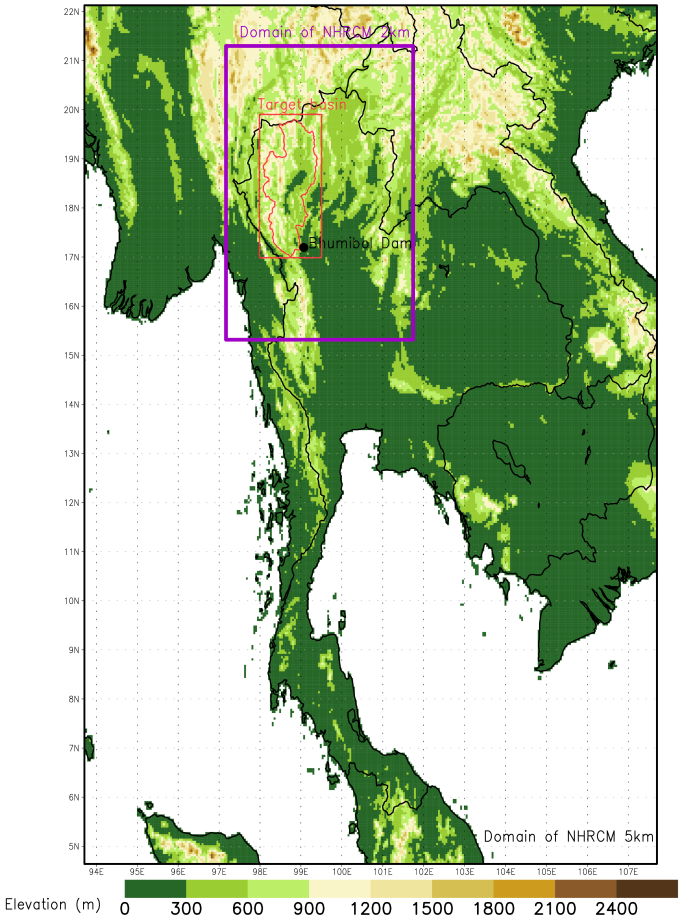

Figure 2.5: Elevation (m) in NHRCM 5–km domain applied in Thailand region. Purple box represents NHRCM 2–km domain, covering Yom and Nan River Basin. Red box indicates the target basin in upper part of the Ping River.

of GCM.

In this study, output from the NHRCM applied in the Thailand region was utilized. This dataset was generated under the Integrated Research Program for Advancing Climate Models (TOUGOU) framework supported by MEXT. Two datasets are available, simulated by the different spatial resolutions of NHRCM: 5 km and 2km grid size. The NHRCM with 5km was nested in MRI–AGCM 3.2S and the NHRCM with 2km was nested in it. The 5km model was simulated for the whole Thailand region, while the 2km model was applied to Yom and Nan River basin (15.2°–21.4°S and 97.3°-101.8°E), as shown in Figure 2.5. Each output dataset consists of 20 years of results of present climate simulation (1980–1999) and future climate simulation (2080–2099) under the RCP8.5 scenario. However, only the results of the present climate simulation are used in this study.

Chapter 3

Analysis of the applicability of runoff generated by land surface models for streamflow simulation

Abstract

This research investigated the applicability of runoff generated by two land surface models (LSMs) for streamflow simulation in the upper part of Ping River Basin, Thailand. Atmospheric output dataset from a general circulation model MRI–AGCM 3.2S with 20–km grid size and a regional climate model NHRCM with 5–km (NHRCM05) and 2–km grid size (NHRCM02) were used as forcing for both LSMs. First, rainfall output from each dataset was evaluated with the observed rainfall. Simulated rainfall by GCM rainfall has shown excellent performance in reproducing the mean observed precipitation. Meanwhile, rainfall from the RCMs tends to underestimate the climatological mean of the observed rainfall. Simulated rainfall by GCM also showed a stronger intensity of daily precipitation than that by the RCMs. The NHRCM02 was able to produce significantly higher intensity than the NHRCM05. From the comparison of the water budget, SiBUC tended to estimate higher evapotranspiration and lower runoff than MRI–SiB. Each LSM generated different runoff characteristics; SiBUC estimated higher surface runoff and lower subsurface runoff than MRI–SiB (Tinumbang *et al*., 2019). Subsurface runoff was the dominant runoff component in MRI–SiB. Different runoff characteristics have shown some impacts on the simulated streamflow. The peak discharge by SiBUC, formed primarily due to surface runoff generation, is produced soon after the peak rainfall event. On the other hand, MRI–SiB's peak flow shows significantly more delay than the peak rainfall. As MRI–SiB is dominated by subsurface runoff, the rainwater is first infiltrated into the soil before it travels

to reach a river, resulting in long lag times. The estimated daily discharge forced runoff from both LSMs was evaluated by using a flow duration curve. Simulated discharge by SiBUC using GCM forcing tends to overestimate the observed peak and low flow, while it shows well reproducibility of the mid–flow. On the other hand, the discharge by MRI–SiB mostly underestimated the observed flow, but it was able to reduce the bias of peak flow by SiBUC. The simulated monthly streamflow was also evaluated to analyze the LSMs' ability to reproduce the seasonal cycles of observed discharge. Overall, all simulated results by both LSMs could reproduce the seasonal variability of the observed discharge, mainly due to the excellent performance of the climate model in simulating the seasonal variability of the observed rainfall. However, different runoff characteristics between the two LSMs have shown some impacts on the simulated peak discharge. Monthly peak discharge by SiBUC has shown the same timing as peak simulated rainfall. On the other hand, peak discharge by MRI–SiB is more delayed than peak rainfall. Simulated discharge by SiBUC using GCM forcing has shown a low bias for simulating annual flow and that in wet and dry seasons, indicating the excellent ability of runoff by SiBUC in reproducing the observed streamflow. In contrast, discharge by MRI–SiB forced by GCM has improved performance in reproducing the peak observed flow, but it mostly underestimated the observed discharge. Meanwhile, most of the simulated discharges forced by the RCMs show much lower volume than the observed inflow, mainly due to underestimating the precipitation output by the RCMs. However, the peak discharge by SiBUC using NHRCM02 shows the best performance in reproducing the peak observed flow (Tinumbang *et al*., 2019a). Stronger rainfall intensity by the NHRCM02 might have an impact on improving the simulated peak discharge. In conclusion, the present work has shown the different runoff characteristics of each LSM and how it affects the simulated streamflow.

3.1 Introduction

Many regions worldwide have been affected by unprecedented extreme floods and drought in recent years. Intergovernmental Panel on Climate Change (2021) reported that it is expected that the risks of water-related disasters are increasing in magnitude and frequency due to global warming. Projections of such phenomena are necessary to design planning and perform appropriate responses to future events.

Climate models, also known as general circulation models or GCMs, have been developed to simulate the present climate and project the changes of future climate. They simulate Earth ' s climate system interactions, including atmosphere, ocean, ice, and land surface. However, the resolution of GCMs output are often too coarse to be used for impact assessment studies for local scale because it do not accurately describe local phenomenon. For regional level assessment, much finer resolution output is generally used, usually by downscaling the output of GCMs, such as utilizing statistical or dynamic methods (using a nested model, known as a regional climate model, RCM).

The output of the climate models have been widely used to predict the changes of river discharge under global warming (Hirabayashi *et al*., 2013, Hunukumbra and Tachikawa, 2013, Manee *et al*., 2017, etc.). However, many researchers (Hirabayashi *et al*., 2013) reported some bias in the simulated discharge by runoff output from the climate models. The possible causes might come from the performance of climate models on simulating precipitation and/or runoff. The latter, runoff, is calculated by the land surface model (LSM) embedded in the climate models. Since runoff plays an essential role in river discharge simulation, it is necessary to evaluate the performance of LSMs from a river discharge viewpoint. Some studies have been done to analyze the performance of LSMs for estimating energy balance components, including sensible and latent heat, and the evaluation for runoff is still limited in the literature (Getirana *et al*., 2017).

This study aims to investigate characteristics of runoff generated by two LSMs and analyze their applicability for streamflow simulation.

Table 3.1: Summary of availability and experimental period for each dataset.

Dataset	Baseline period	Spin–up period	Analysis period
Observed rainfall Observed streamflow			1990–1999
MRI–AGCM 3.2S	1979–2003	1979–1989	1990–1999
NHRCM05 NHRCM02	1980–1999	1980–1989	1990–1999

3.2 Methodology

3.2.1 Simulation designs

This study utilized the output of general circulation model MRI–AGCM 3.2S with 20–km mesh size, and regional climate model NHRCM with 5–km and 2–km mesh size, which was applied in the Thailand region. This analysis only used the output of the baseline period from each dataset. The data from MRI–AGCM 3.2S and NHRCM consist of 25–years and 20–years, respectively, as shown in Table 3.1.

One year data of MRI–AGCM 3.2S consists of 12 months, starting from January to December. On the other hand, the one-year dataset from NHRCM consists of 13 months, starting from the beginning of April to the end of April in the following year. Hence, the first-month data of NHRCM was discarded as model spin up, and the last 12–months data, starting from May to April in the following year, were utilized for simulation.

In this study, simulation by MRI–AGCM 3.2S atmospheric forcing data was conducted for 25–years, while NHRCM was for 20–years. For each dataset, the simulation results during 1990–1999 were utilized for impact analysis, and the rest were discarded as spin-up simulations.

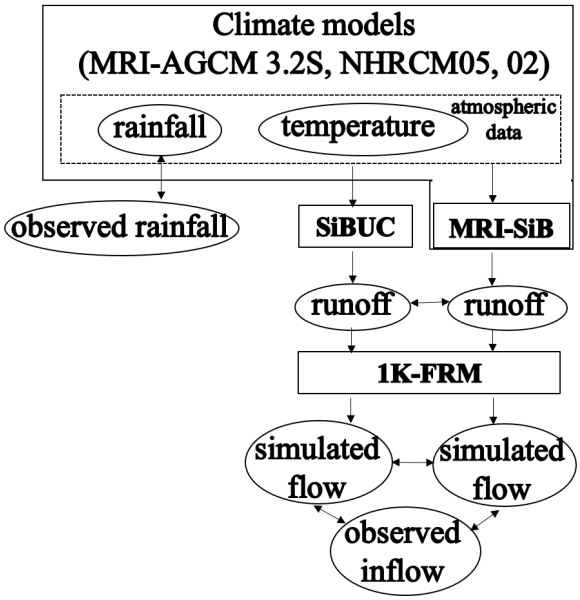

Figure 3.1: Framework and impacts analysis of this study.

3.2.2 Impact analysis

Figure 3.1 shows the framework and impacts analysis of this study.

At first, rainfall output from each climate model was evaluated by comparing it with the observed CHIRPS rainfall data. The evaluation was performed by analyzing the spatial pattern of the rainfall, climatological–mean of basin average monthly rainfall, frequency, and intensity of precipitation from each dataset.

After that, runoff simulation was performed by SiBUC utilizing the atmospheric data from the output of each climate model. Characteristics of runoff generated by SiBUC were compared with that by MRI–SiB. In this analysis, the estimated runoff by MRI–SiB was obtained from the output dataset of each climate model. Since both LSMs utilized the same atmospheric data, different runoff estimations indicated different settings (land surface parameters, model structures, etc.) between the two LSMs.

Then, the generated runoff by both LSMs was given to a flow routing model for simulating the streamflow. The simulated discharge was extracted as daily discharge at the outlet of Bhumibol Dam, and it was evaluated by comparing it with the observed inflow into this dam. The characteristics of simulated discharge forced by the runoff by both LSMs were examined in terms of volume of the discharge as well as the timing of peak discharge.

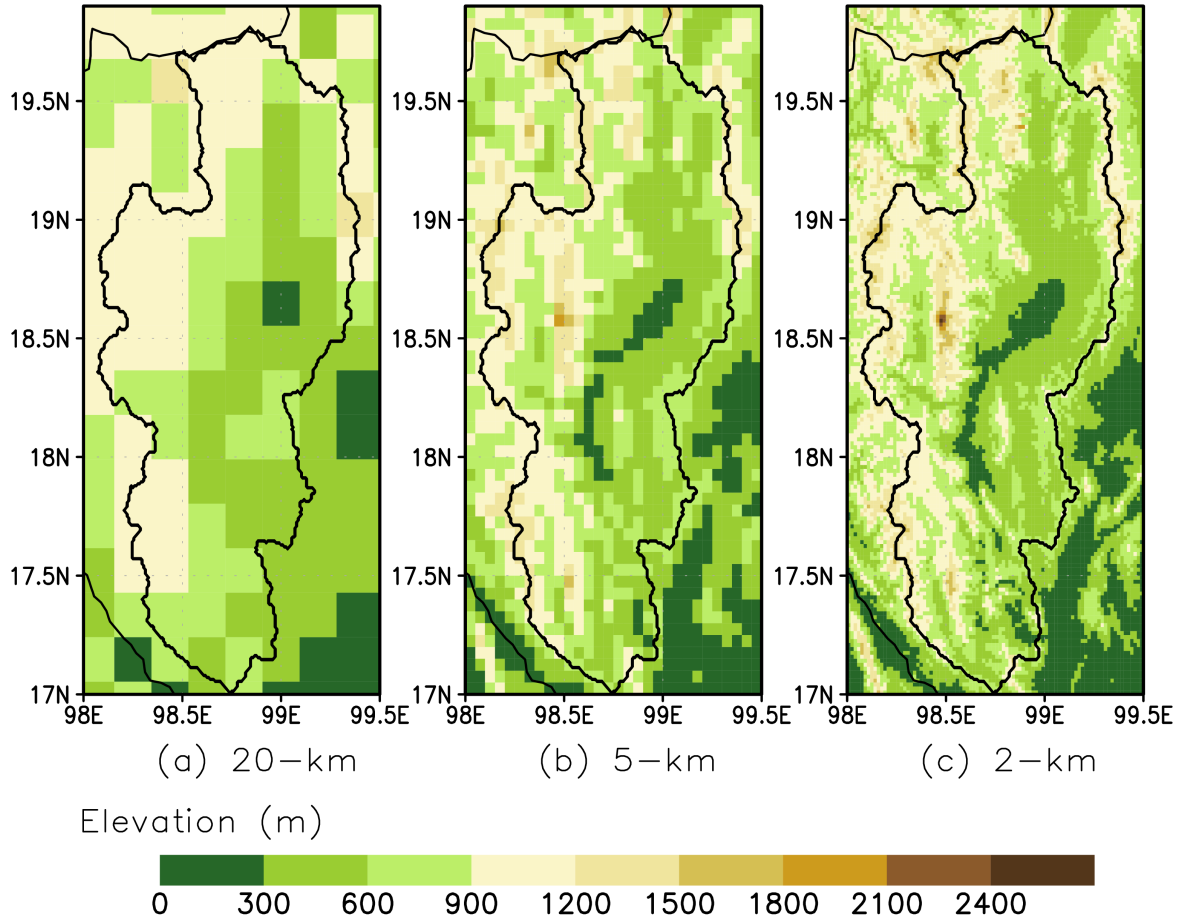

Figure 3.2: Comparison of topography among different spatial resolution of SiBUC.

3.2.3 Modeling approach for runoff simulation by SiBUC

The spatial resolution of SiBUC was set according to the mesh size of the climate models. Hence, SiBUC with three different spatial resolutions was utilized in this study: 20–km, 5–km, and 2–km mesh size.

SiBUC with 5–km spatial resolution for the upper part of Ping River Basin developed by Yorozu *et al*., (2018) was used for this study. It was confirmed that the simulated discharge by the developed model could well reproduce 2011–big flood event in this basin, as shown in Figure 3.3, with Nash–Sutcliffe Efficiency (NSE) is 0.79, Root Mean Square Error (RMSE) is 219 m^3 s^{-1}, and the correlation coefficient is 0.90 (Yorozu *et al*., 2018).

SiBUC with 20–km spatial resolution was developed by interpolating the resolution of SiBUC with 5–km into 20–km using the nearest neighbor method. On the other hand, SiBUC with 2–km mesh size was developed by upscaling the original input data of SiBUC from 1–km to 2–km

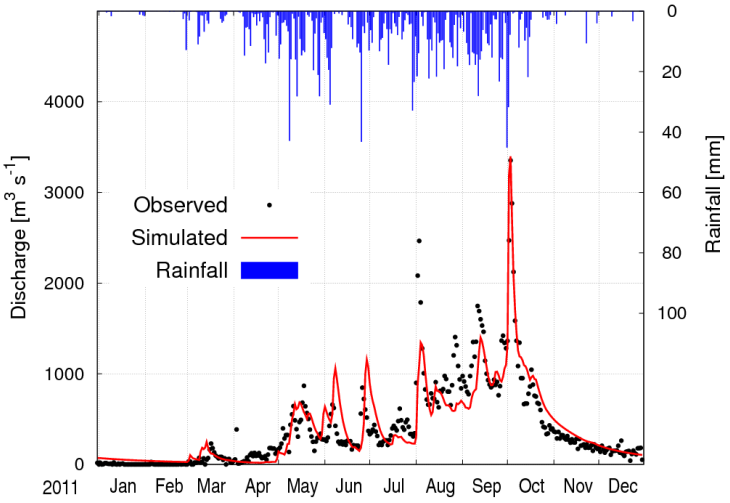

Figure 3.3: Comparison of daily discharge from observation (black dot) and simulation (red line) in 2011. Reproduced from Yorozu *et al*. (2018).

resolution by the same method.

Comparison of topography among different spatial resolutions of SiBUC is shown in Figure 3.2. The 20–km, 5–km, and 2–km model utilize 9×17 (163), 30×58 (1740), and 90×174(15660) grid cells, respectively.

3.3 Evaluation of rainfall output from the climate models

3.3.1 Spatial patterns of climatological mean rainfall

For rainfall evaluation, at first, spatial distribution of the simulated rainfall from the climate models was compared with the observed rainfall. In this analysis, the spatial resolution of MRI–AGCM 3.2S and NHRCM02 were interpolated using the nearest neighbor method to be the same as that of the observed CHIRPS rainfall (0.05°). NHRCM05 rainfall was not interpolated as it already had the same resolution as that of the observed rainfall dataset.

The differences between the simulated and observed rainfall were calculated in terms of percent of bias (PBIAS), shown in Eq. (5.3).

$$PBIAS = \frac{\sum_{i=1}^{N} (M_{\mathrm{i}} - O_{\mathrm{i}})}{\sum_{i=1}^{N} O_{\mathrm{i}}} \times 100 \tag{3.1}$$

with M and O represents the rainfall amount from the model and observation, respectively. The bias measures the tendency of the simulated rainfall to be higher (positive value) or lower (negative value) than the observation, with the optimal value is equal to zero. We estimated the bias of 10–years mean annual rainfall and the average rainfall in wet (May to October) and dry (November to April) seasons.

Figure 3.4 shows the spatial pattern of average annual, wet, and dry seasons observed rainfall, as well as the bias of the simulated rain by MRI–AGCM 3.2S, NHRCM05, and NHRCM02. The observed annual rainfall shows a diverse distribution, with more rain in the northern and southwest and less rainfall in the middle of the basin. As seen, abundant rainfall occurs in the wet season and less rainfall in the dry season.

Simulated rainfall by MRI–AGCM 3.2S shows a good performance in reproducing the mean annual and wet season rainfall, but it mostly overestimates the precipitation in the dry season. This wet bias in GCM in the dry season is slightly reduced by dynamically downscaling, as shown by NHRCM05 rainfall, especially in the basin. However, overall results by RCMs rainfall do not show significant improvement, as it mostly underestimated the observed rainfall in both wet and dry seasons in most regions.

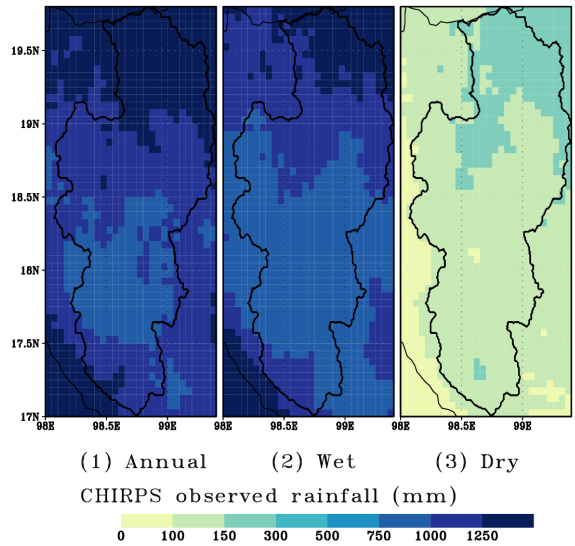

(a) Spatial patterns of CHIRPS observed rainfall.

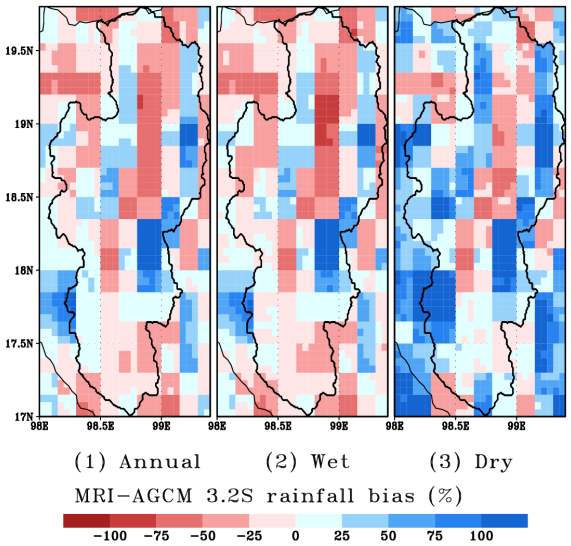

(b) Spatial patterns of bias for MRI–AGCM 3.2S rainfall.

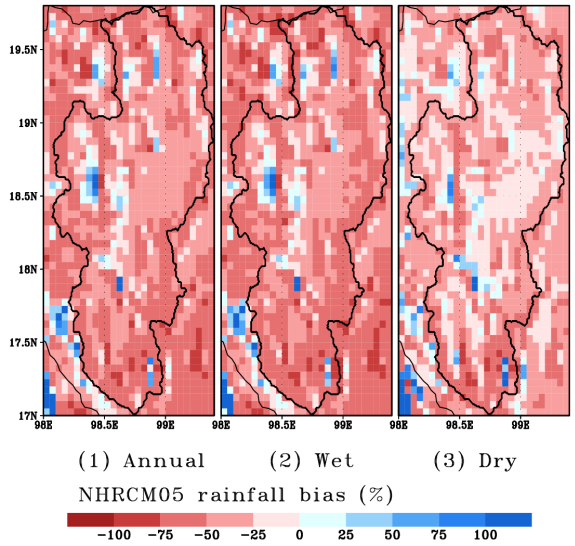

(c) Spatial patterns of bias for NHRCM05 rainfall.

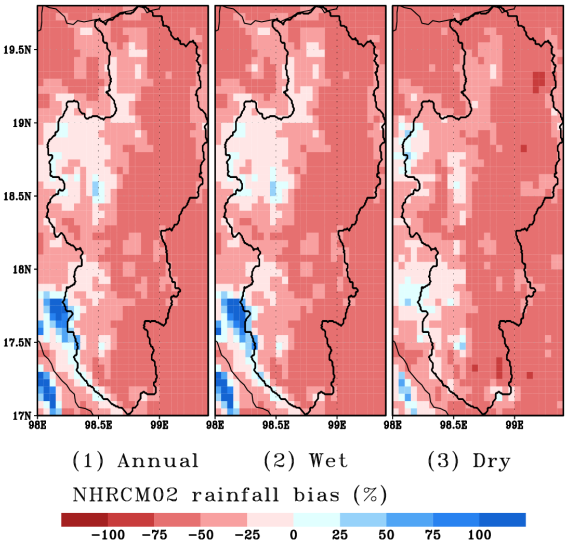

(d) Spatial patterns of bias for NHRCM02 rainfall.

Figure 3.4: Spatial patterns of climatological mean (1) annual, (2) wet (May to October), and (3) dry seasons (November to April) rainfall from (a) observation, and bias of simulated rainfall from (b) MRI–AGCM 3.2S, (c) NHRCM05, and (d) NHRCM02.

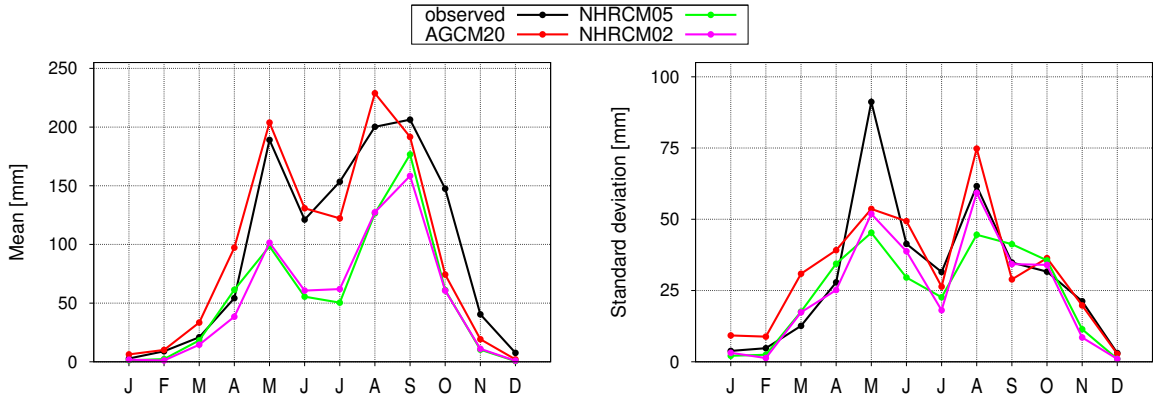

Figure 3.5: Seasonal cycles of (a) mean and (b) standard deviation of observed rainfall (black line) and rainfall output from MRI–AGCM 3.2S, NHRCM05, and NHRCM02, shown in the red, green, and pink lines, respectively.

Table 3.2: Mean and standard deviation of observed annual, wet, and dry seasons rainfall (unit: mm), and the evaluation of rainfall from each dataset in terms of PBIAS.

Dataset	Mean			Standard deviation		
	Annual	Wet	Dry	Annual	Wet	Dry
Observed [mm]	1152	1018	135	82	59	23
MRI–AGCM 3.2S	-3	-6	25	-0.2	13	61
NHRCM05	-43	-44	-30	-30	-8	10
NHRCM02	-45	-44	-50	-31	-10	-23

3.3.2 Seasonal cycles of basin average rainfall

Figure 3.5 shows seasonal variations in the mean and standard deviation of rainfall for each dataset, and Table 3.2 shows the evaluation of rain from different climate models in terms of percent bias (PBIAS). This analysis aims to evaluate the ability of the climate models in reproducing the observed pattern of rainfall and its interannual variability. In this analysis, all the rainfall was computed as basin average for 10–years period.

The area means annual rainfall estimated from the CHIRPS dataset is 1152 mm. This value is close to mean annual (during 1981–2004) rainfall estimated from gauges stations, which is 1101 mm (Kotsuki *et al*., 2013). In this basin, more than 80% of the annual rainfall occurs in the wet season, and the rest in the dry season.

In general, the rainfall from all datasets could capture the seasonal cycle of precipitation in this basin. The observation peak rainfall in the early and late rainy seasons occurs in May and

September, respectively. Rainfall from GCM shows the same peak time in the early wet season, but it produces an earlier peak in the late rainy season in August. On the other hand, the rainfall from both RCMs shows the same peak time in the early and late rainy seasons as that of the observed rainfall. However, the peak value from RCMs tends to be underestimated, while the peak value from GCM rainfall shows a better fit with the observation.

Overall, the rainfall from GCM has better performance than the RCMs in reproducing the mean and interannual variability of the observed annual rainfall. The wet season shows a lower bias, indicating good abilities to reproduce the observed rainfall, but in the dry season, it produces about 25% excessive precipitation. On the other hand, rainfall from both RCMs tends to underestimate the mean and standard deviation of observed annual rainfall. Estimated rainfall from NHRCM05 shows a lower bias than the rainfall from NHRCM02 in the dry season. In general, the simulated rainfall from the climate models is better at capturing the interannual variability of observed precipitation in the wet season.

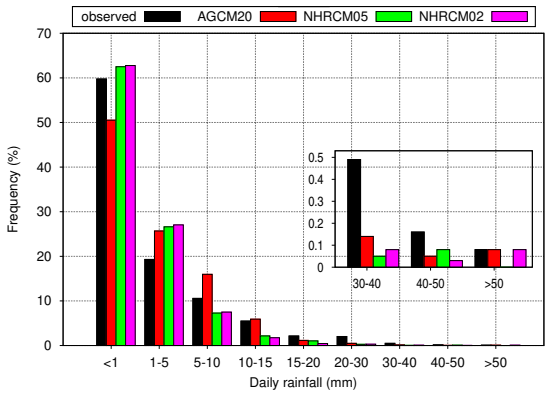

(a) Frequency of daily rainfall. Subplot indicates frequency of daily rainfall more than 30 mm day^{-1}.

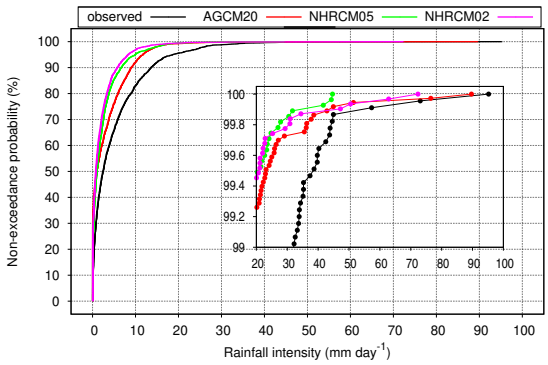

(b) Non–exeedance probability of daily rainfall. Subplot indicates proportion of rainfall more than 99th percentile in all rainfall events.

Figure 3.6: Frequency and intensity of daily rainfall from observation and simulation from MRI–AGCM 3.2S, NHRCM05, and NHRCM02, represent by black, red, green, and pink colors, respectively.

3.3.3 Frequency and intensity of daily rainfall

Figure 3.6(b) shows the frequency of daily rainfall from observation and simulation from each climate model. RCMs rainfall tends to be closer to the observed rainfall in simulating the light rain (1 mm day^{-1}), while the rainfall from GCM has less light rain. The simulated rainfall by MRI–AGCM 3.2S and NHRCM02 show more frequent heavy rain (50 mm day^{-1}) than that of NHRCM05 and are close to the observed rainfall.

Figure 3.6(b) shows a non–exceedance probability of rainfall (mm day^{-1}) between observed and simulated rainfall from each climate model. For extreme rainfall (more than the 99th percentile), the MRI–AGCM 3.2S shows a higher intensity than the rainfall from RCMs and is closer to observed. The rainfall from 2–km mesh size NHRCM shows a stronger intensity than the 5–km NHRCM.

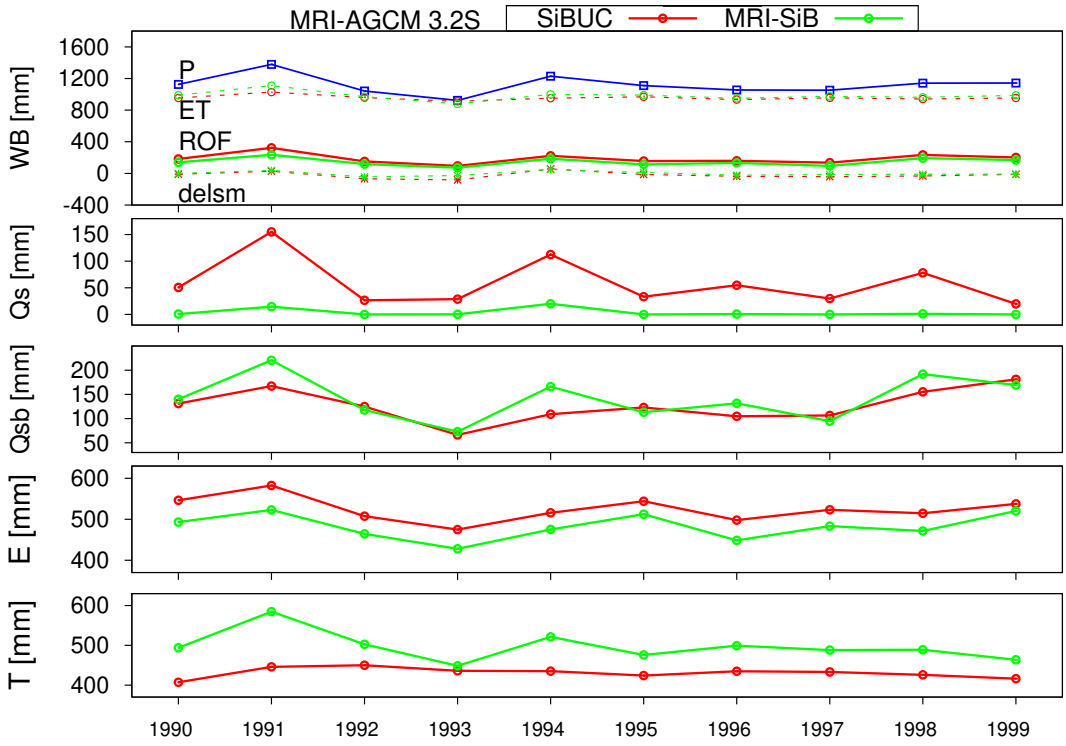

Figure 3.7: Comparison of annual water budget (WB) by SiBUC (red line) and MRI–SiB (green line) forced by MRI–AGCM 3.2S atmospheric data. P, ET, ROF, delsm, Qs, Qsb, E, and T represent precipitation, evapotranspiration, runoff, change of soil moisture, surface runoff, sub-surface runoff, evaporation, and transpiration, respectively.

3.4 Analysis of water budget and runoff characteristics

Figure 3.7, Figure 3.8, and Figure 3.9 show annual water budget by SiBUC and MRI–SiB forced by MRI–AGCM 3.2S, NHRCM05, and NHRCM02, respectively. Water budget by MRI–SiB embedded in the NHRCM is unbalanced because it was simulated by time–slice integration method. In addition, one out of 13–months in one–year result by NHRCM was discarded since it was assumed as NHRCM spin–up.

Overall, estimated evapotranspiration by MRI–SiB tends to be higher, and the generated runoff tends to be lower than that by SiBUC. When the rainfall amount is relatively low, as shown by NHRCM05 rainfall in 1992 and 1997 (less than 600 mm), the estimated evapotranspiration by MRI–SiB exceeds the annual rainfall. Due to low rainfall amounts, evapotranspiration could occur by extracting more water from the soil.

Fluctuations of annual runoff from both LSMs seem to be affected by rainfall amount and rainfall intensity. For example, annual rainfall by NHRCM05 in 1990 and 1991 is 815 mm and

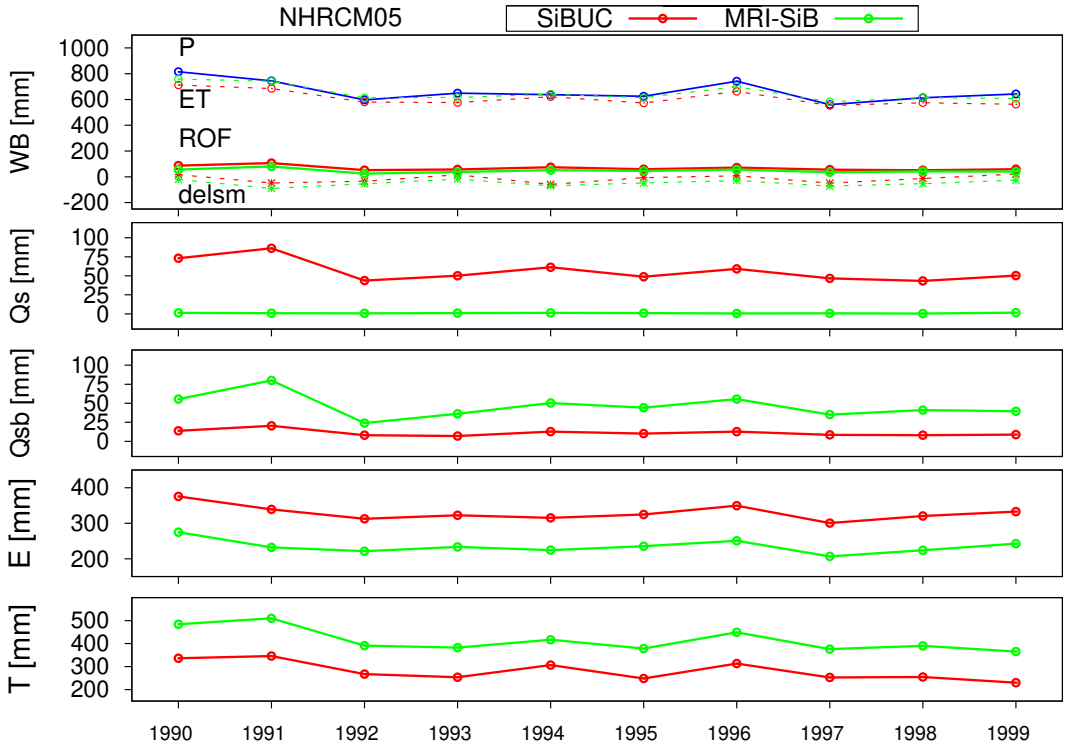

Figure 3.8: Similar to previous figure, but the forcing is NHRCM05 atmospheric data.

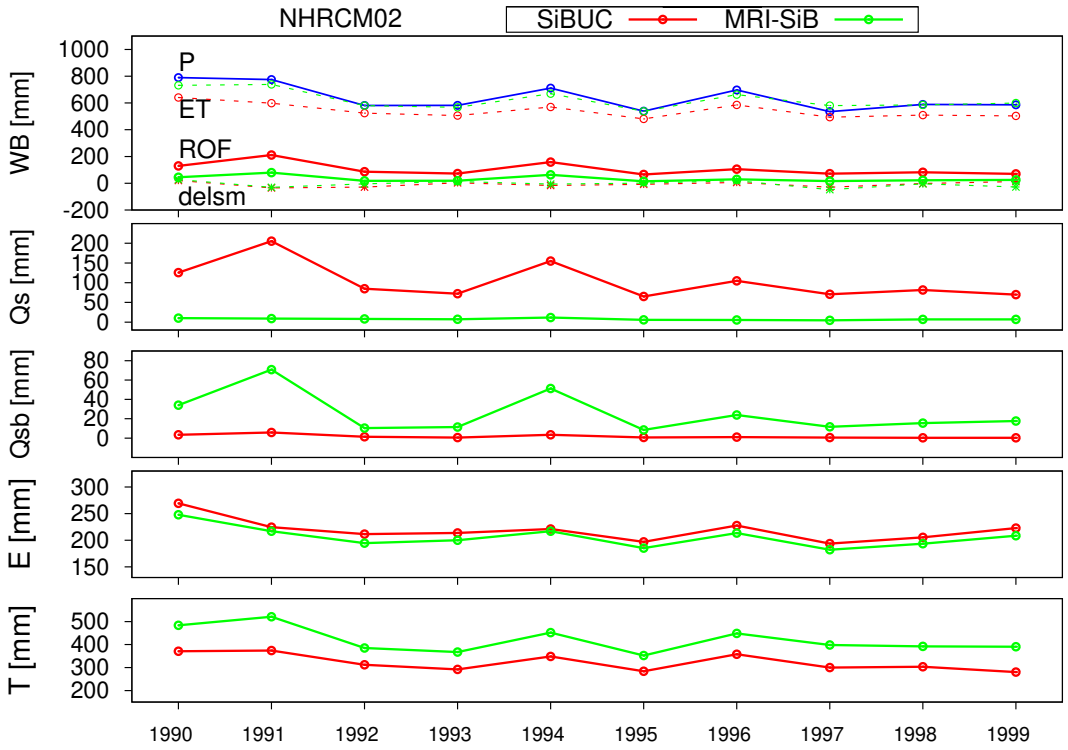

Figure 3.9: Similar to previous figure, but the forcing is NHRCM02 atmospheric data.

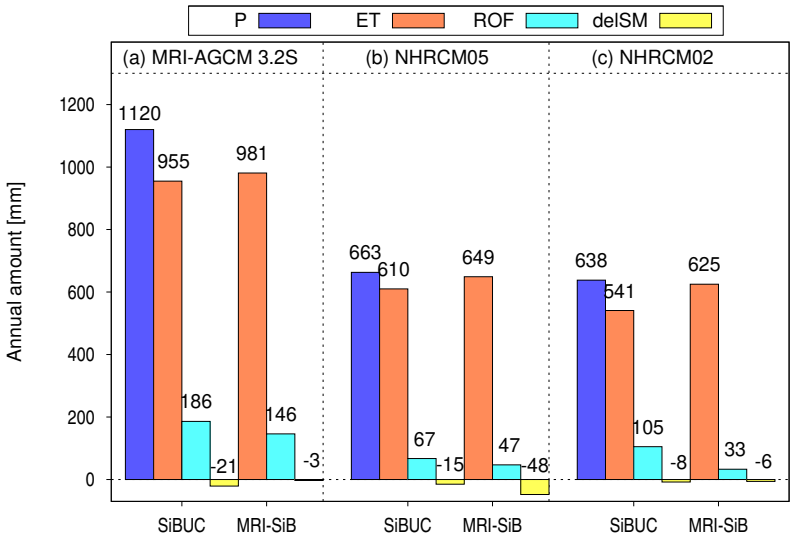

(a) Mean annual water budget. Blue, orange, light blue, and yellow bars represent rainfall, evapotranspiration, runoff, and change of soil moisture, respectively.

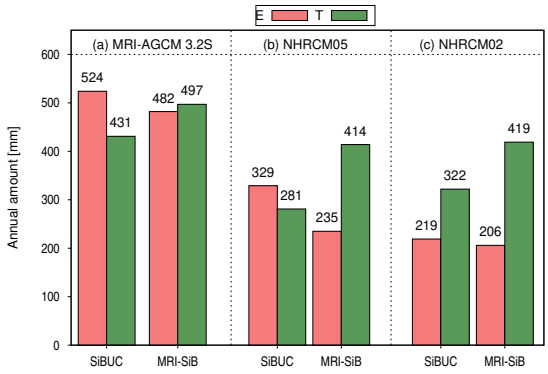

(b) Mean annual evapotranspiration components. Red and green bars represent evaporation and transpiration, respectively.

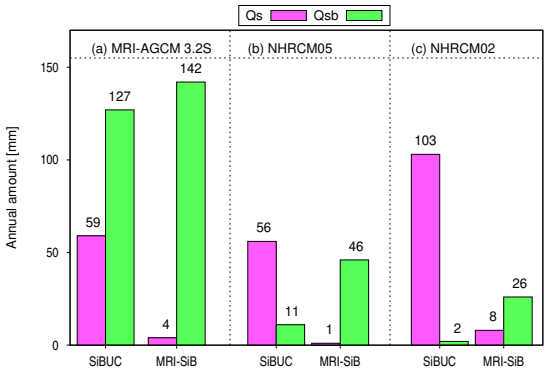

(c) Mean annual runoff components. Pink and green bars represent surface and subsurface runoff, respectively

Figure 3.10: Mean annual water budget components simulated by SiBUC and MRI–SiB, forced by atmospheric output from (a) MRI–AGCM 3.2S, (b) NHRCM05, and (c) NHRCM02.

744 mm, respectively. In 1991, estimated runoff by both LSMs was higher (SiBUC: 106 mm, MRI–SiB: 81 mm) than that in 1990 (SiBUC: 87 mm, MRI–SiB: 57 mm). That was affected by extreme rainfall events, which caused the high estimated runoff.

Figure 3.10(a) shows a mean annual water budget by SiBUC and MRI–SiB forced by atmospheric output from each dataset. In this basin, 10–years–mean of runoff depth estimated

from inflow into the Bhumibol Dam is 183 mm. As the mean annual rainfall is 1152 mm, the evapotranspiration in this basin is estimated to occupy more than 80% of the total precipitation.

Between the two LSMs, the generated runoff by SiBUC forced by output from MRI–AGCM 3.2S is closer to the observed runoff depth. On the other hand, simulated runoff by both LSMs forced by RCMs forcing is lower than the observed runoff. That is due to the underestimated rainfall by the RCMs.

Figure 3.10(b) shows a comparison of mean annual evapotranspiration components between SiBUC and MRI–SiB forced by each output dataset. Overall, estimated evaporation by SiBUC tends to be higher than MRI–SiB, while the estimated transpiration is the opposite.

Comparison of mean annual runoff components between SiBUC and MRI–SiB forced by atmospheric data from each dataset is shown in Figure 3.10(c). As seen, the estimated runoff by MRI–SiB is dominated by subsurface runoff in all simulations regardless of the atmospheric forcing. On the other hand, SiBUC tends to estimate higher surface runoff and lower subsurface runoff than MRI–SiB. However, the ratio of surface and subsurface runoff estimated by SiBUC differ depending on the atmospheric data.

By using MRI–AGCM 3.2S forcing, surface runoff and subsurface runoff by SiBUC occupy about 30% and 70% of the total runoff, respectively. While, when the atmospheric data from RCMs output were used, SiBUC estimated significantly higher surface runoff than the subsurface runoff. In particular, by using the NHRCM02 forcing, SiBUC generated mostly only surface runoff. The amount of surface runoff by SiBUC was also particularly high in this simulation, even though the rainfall amount by the NHRCM02 was relatively low. That difference in runoff characteristics by SiBUC among different forcing is caused by the difference in rainfall intensity. For this analysis, one year result, such as in 1992, was investigated in detail.

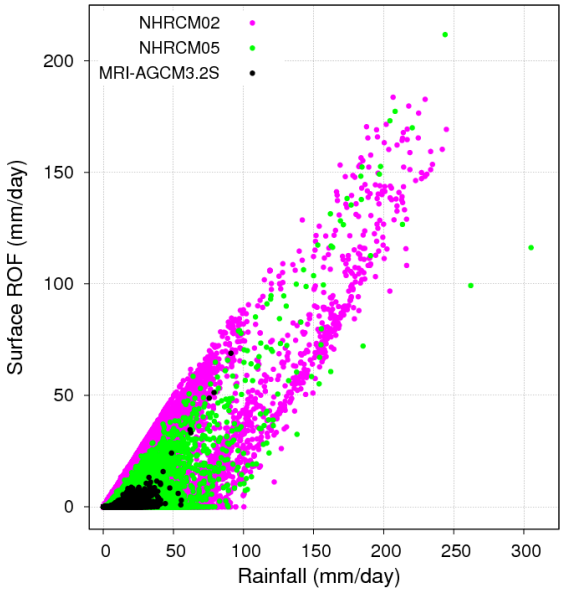

Figure 3.11: Scatter plot of daily rainfall and surface runoff generated by SiBUC in 1992. Only grid cells within Bhumibol Dam catchment are plotted. Black, green, and pink dots represent forcing data from MRI–AGCM 3.2S, NHRCM05, and NHRCM02, respectively. Unit is mm.

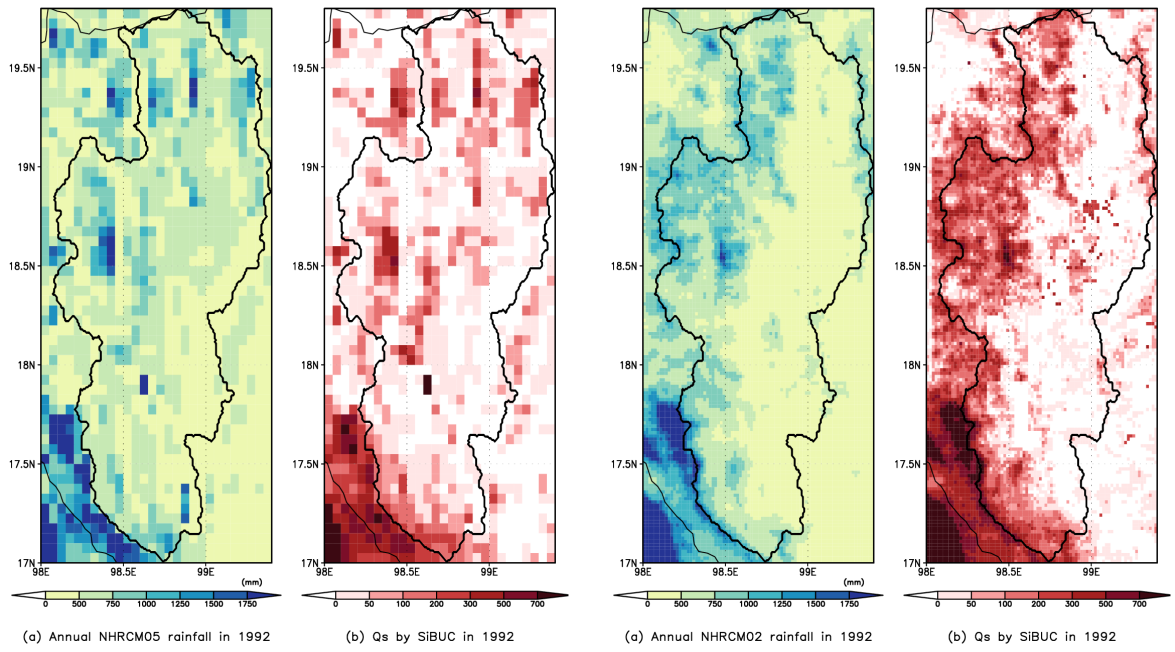

(a) Simulation by NHRCM05 forcing.

(b) Simulation by NHRCM02 forcing.

Figure 3.12: Spatial pattern of annual rainfall (P) and surface runoff (Qs) generated by SiBUC in 1992. Unit is mm.

Relationship between rainfall and surface runoff generated by SiBUC using each forcing in 1992 was investigated. In this year, annual rainfall by MRI–AGCM 3.2S, NHRCM05, and NHRCM02 is 1042 mm, 597 mm, and 581 mm, respectively. The generated surface runoff by SiBUC by each forcing is 26 mm, 30 mm, and 85 mm, respectively. Although the total rainfall by the GCM is the highest, the generated surface runoff by SiBUC is relatively lower than by using the RCMs forcing. In addition, even though total rainfall by the RCMs is similar, SiBUC generated very high surface runoff by using NHRCM02 compared to by NHRCM05.

Figure 3.11 shows a scatter plot of daily rainfall and surface runoff generated by SiBUC for grid cells within the basin in 1992 by using each forcing. As seen from this figure, the higher the spatial resolution of the climate models, the more grid cells with high rainfall intensity, such as rainfall more than 100 mm day^{-1}. The high rainfall intensity corresponds to the high surface runoff generated by SiBUC. As the RCMs had more cells with high–intensity rainfall than the GCM, surface runoff estimated by SiBUC forced by the RCMs atmospheric data tends to be more dominant than that by the GCM forcing.

In addition, the spatial distribution of rainfall also affects the runoff generation. Figure 3.12 shows a spatial pattern of annual rainfall and surface runoff generated by SiBUC in 1992 forced by NHRCM05 and NHRCM02. Even though the basin average rainfall by the RCMs is similar, the rainfall distribution is different in both RCMs. In particular, the NHRCM02 tends to have more intense rainfall in mountainous region of the western part of this basin compared to the NHRCM05. On the other hand, in the low–elevation region (eastern area of the basin), the estimated rainfall by NHRCM05 tends to be higher than the NHRCM02.

From this figure, the spatial pattern of surface runoff by SiBUC mostly corresponds to the spatial distribution of rainfall: the higher the rainfall, the higher the surface runoff. As there are more grid cells in the NHRCM02 with high rainfall than the NHRCM05, the number of cells corresponding to high surface runoff by SiBUC is also higher, resulting in higher surface runoff generation by SiBUC forced by NHRCM02 compared to that of NHRCM05.

In summary, even though the RCMs has similar rainfall amount, the generated surface runoff by SiBUC between NHRCM05 and NHRCM02 is greatly different. It is due to the difference in rainfall intensity and spatial distribution of rainfall. The generated surface runoff by SiBUC forced by NHRCM02 is higher than NHRCM05 because the NHRCM02 rainfall tends to have higher intensity and more grid cells with high rainfall amount compared to NHRCM05.

Overall, in this section, the differences in water budget estimation as well as runoff char-

acteristics between the two LSMs were found, even though they were forced with the same atmospheric forcing data. This difference in the ability of the LSMs in simulating the water budget components might be due to the differences in land surface parameters, representation of physical processes in land surface, etc.

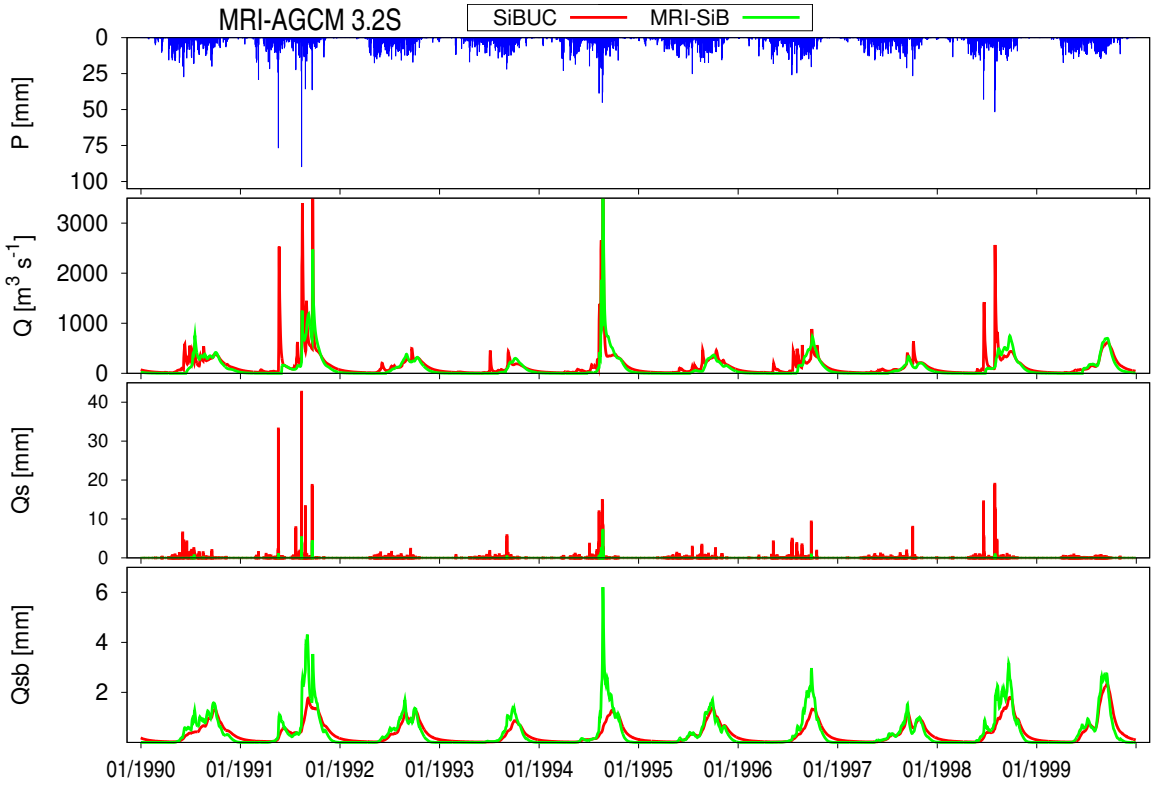

Figure 3.13: Time series of daily precipitation (P) from MRI–AGCM 3.2S, simulated daily discharge (Q), surface runoff (Qs), and subsurface runoff (Qsb) by SiBUC (red line) and MRI–SiB (green line).

3.5 Evaluation of simulated river discharge

3.5.1 Characteristics of simulated daily discharge

Figure 3.13, Figure 3.14, and Figure 3.15 shows simulated daily discharge forced by runoff by SiBUC and MRI–SiB utilizing atmospheric data from MRI–AGCM 3.2S, NHRCM05, and NHRCM02 output datasets, respectively. In general, simulated discharge by SiBUC is higher than that by MRI–SiB due to higher runoff estimation.

Figure 3.16(a) shows the simulated daily discharge in 1991 by using MRI–AGCM 3.2S forcing. As can be seen, both LSMs show different abilities in simulating the streamflow due to the differences in the estimated runoff characteristics. The increase and decrease of the simulated discharge by SiBUC runoff show a similar response to the rainfall events. As the discharge by SiBUC was formed mainly through surface runoff, the discharge increases soon after the rainfall events.

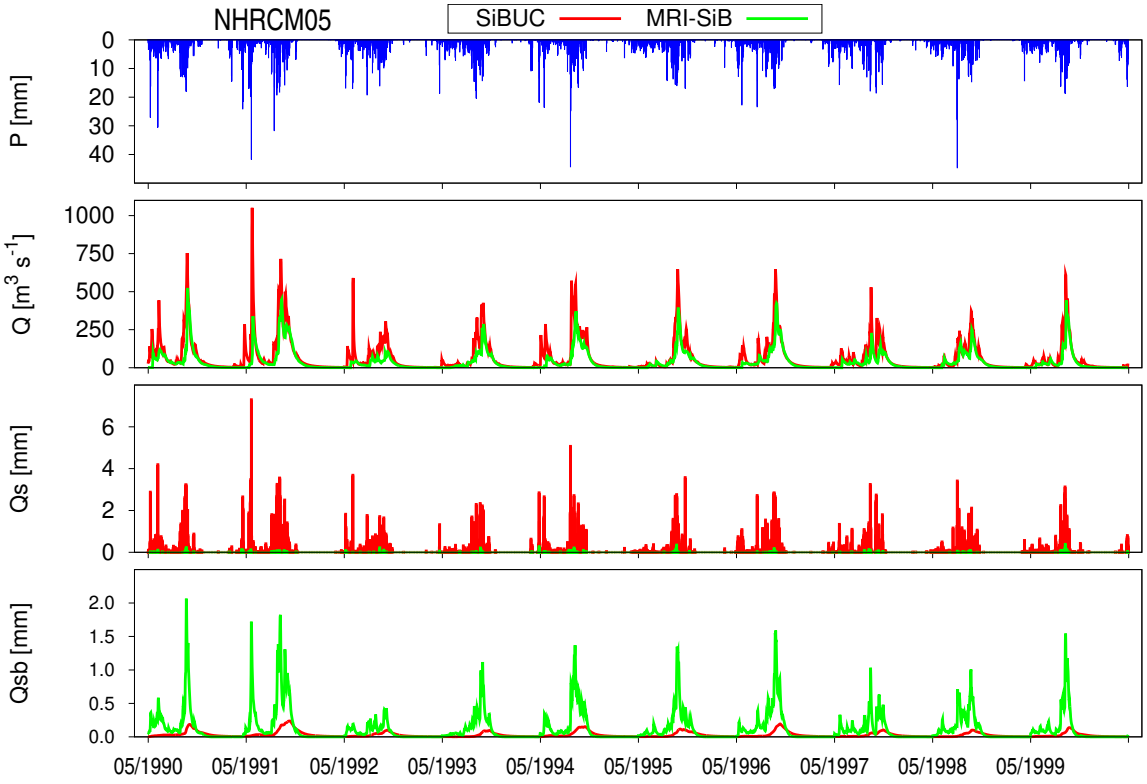

Figure 3.14: Similar to Figure 3.13 but the forcing is NHRCM05 atmospheric data.

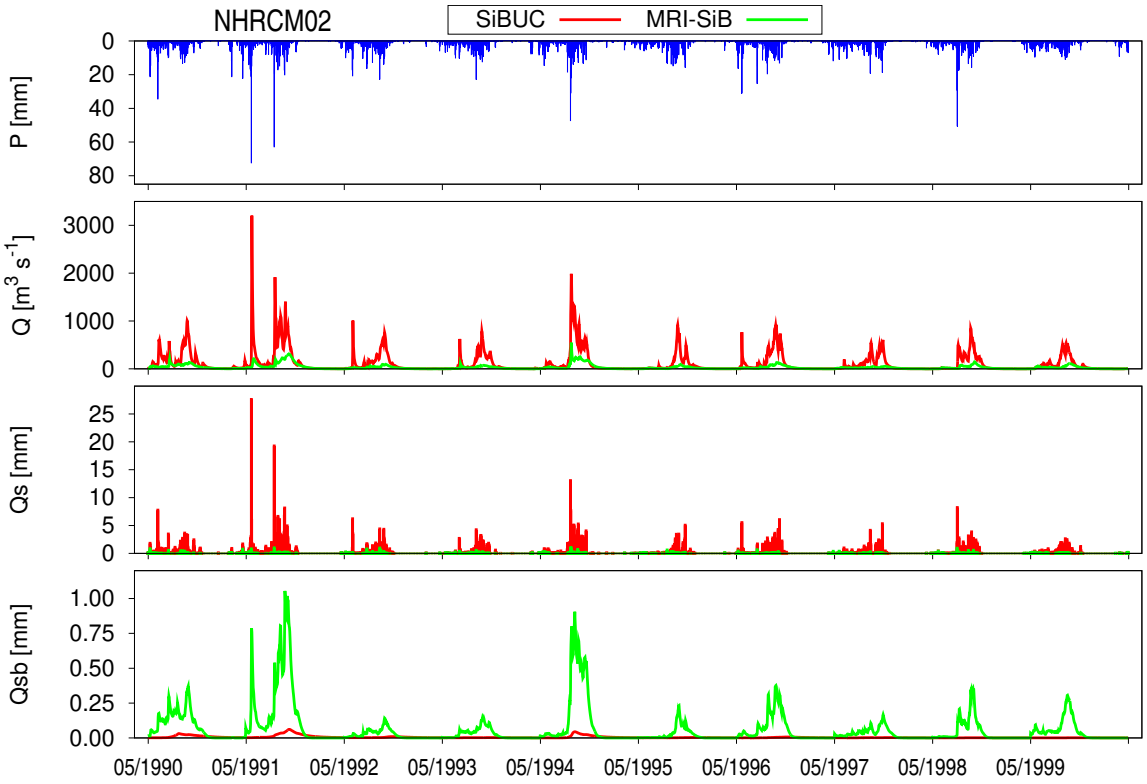

Figure 3.15: Similar to Figure 3.13 but the forcing is NHRCM02 atmospheric data.

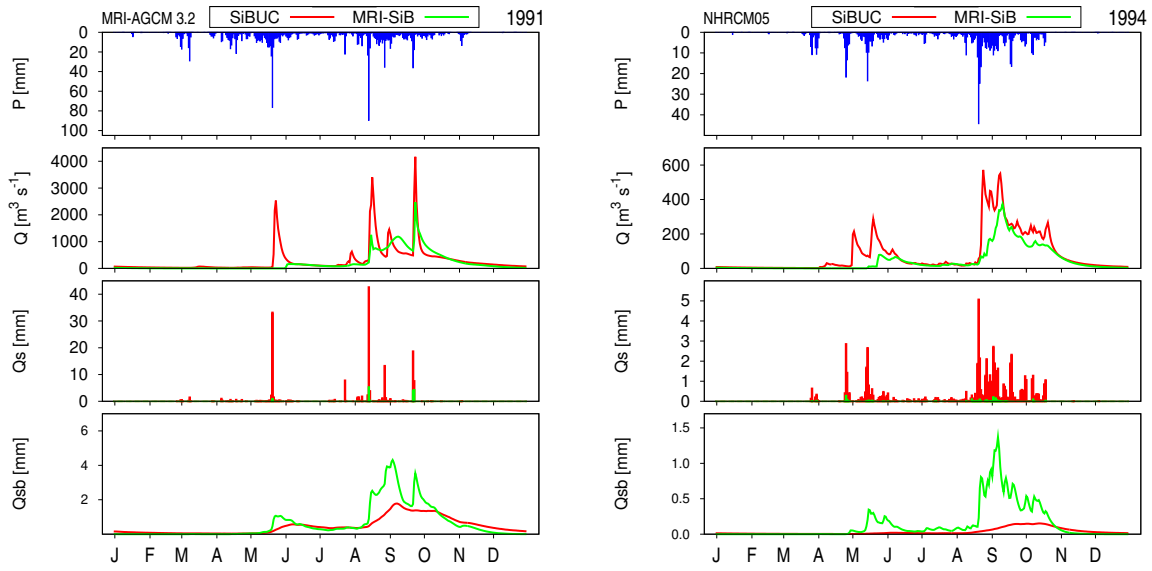

(a) Simulated daily discharge by MRI–AGCM 3.2S in 1991.

(b) Simulated daily discharge by NHRCM05 in 1994.

Figure 3.16: Time series of daily precipitation (P), simulated daily discharge (Q), surface runoff (Qs), and subsurface runoff (Qsb) between SiBUC (red line) and MRI–SiB (green line).

Meanwhile, the estimated discharge by MRI–SiB does not show such high discharge in response to the earlier intense rainfall events, as shown at the end of May. As subsurface runoff is the dominant runoff component in MRI–SiB, the effect of catchment wetness can be seen here. It is thought that the first rainwater is used to increase the soil moisture, and as the wetness of the soil gets higher, the discharge starts to rise.

Different runoff components between the two LSMs also results in the different lag time of the simulated discharge, such as shown in Figure 3.16(b). In this year, the peak of a rainfall event is shown in the mid of August. As seen, the peak discharge by SiBUC is produced soon after the peak rainfall event, while the peak flow by MRI–SiB show significantly more delayed at the beginning of September. As surface runoff is dominant in SiBUC, the rainwater enters the river quicker, resulting in shorter lag times. Oppositely, as MRI–SiB is dominated by subsurface runoff, the rainwater is first infiltrated into the soil before it travels to reach a river, resulting in longer lag times.

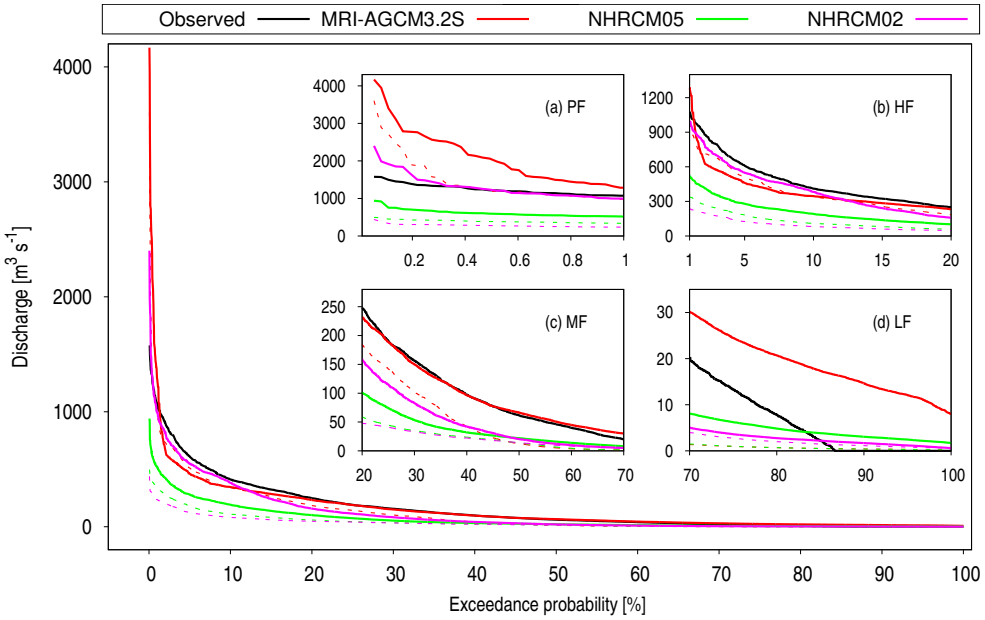

Figure 3.17: Flow duration curve (FDC) of observed (black line) and simulated discharge forced by runoff by SiBUC (solid line) and MRI–SiB (dash line). Red, green, and pink colors represent atmospheric forcing data from MRI–AGCM 3.2S, NHRCM05, and NHRCM02. The FDC is partitioned into four zones: (a) peak flow (0–1% of exceedance probability), (b) high flow (1–20%), (c) mid flow (20–70%), (d) low flow (70–100%).

3.5.2 Evaluation of simulated daily streamflow

Figure 3.17 shows a comparison of the flow duration curve (FDC) of the observed and simulated daily streamflow for 10–years period. Following Chilkoti *et al*. (2019), in this analysis, the FDC is partitioned into four different zones: (a) peak flow (PF, 0–1% of exceedance probability), (b) high flow (HF, 1–20%), mid flow (MF, 20–70%), low flow (LF, 70–100%). Simulated daily discharge by the runoff from each LSM is evaluated by calculating the PBIAS of each zone, as shown in Figure 3.18.

By utilizing MRI–AGCM 3.2S forcing, the simulated discharge by SiBUC tends to overestimate the observed peak and low flow, while it could well reproduce the observed mid flow. The simulated flow by MRI–SiB tends to underestimate all flow, except the peak flow, which shows a lower PBIAS, indicating a better model performance.

Compared to the simulated flow forced by GCM forcing, the estimated peak flow by SiBUC utilizing NHRCM02 is closer to the observation. However, all simulated discharges by both LSMs forced by RCMs forcing tend to underpredict the observed flow in most zones. That is mainly due to the underestimation of the simulated rainfall from the RCMs.

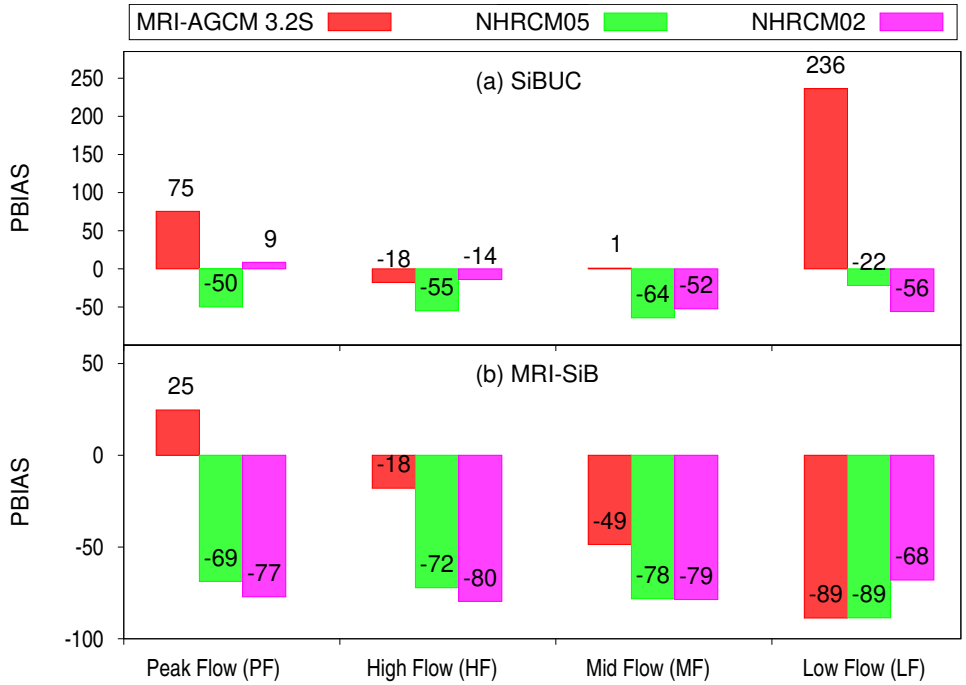

Figure 3.18: Percent bias of flow duration curve (FDC) for simulated discharge by (a) SiBUC and (b) MRI–SiB (dash line). Red, green, and pink bars represent atmospheric forcing data from MRI–AGCM 3.2S, NHRCM05, and NHRCM02.

All simulated discharge by MRI–SiB shows more negative biases than SiBUC, as MRI–SiB tends to produce lower runoff estimation.

Table 3.3: Mean of annual, wet, and dry seasons observed streamflow(unit: m^3 s^{-1}), and the evaluation of rainfall from each dataset in terms of PBIAS.

Dataset	LSMs	Annual	Wet	Dry
Observed [m^3 s^{-1}]		1805	1471	334
MRI–AGCM 3.2S	SiBUC	-1	-3	5
	MRI–SiB	-25	-19	-49
NHRCM05	SiBUC	-57	-53	-72
	MRI–SiB	-74	-72	-83
NHRCM02	SiBUC	-24	-15	-67
	MRI–SiB	-79	-79	-79

3.5.3 Evaluation of average monthly simulated streamflow

Figure 3.19 shows a comparison of 10–years–mean monthly observed and simulated discharge forced by runoff by SiBUC and MRI–SiB utilizing the forcing from each dataset. There are some differences between the simulated discharge by both LSMs in terms of discharge volume and peak discharge timing.

The monthly discharge by SiBUC shows the same timing of peak flow as that of peak rainfall. For example, peak rainfall by MRI–AGCM 3.2S is shown in August, and by RCMs is in September. All the peak discharge by SiBUC is shown in August, and the RCMs forcing is shown in September. On the other hand, most of the peak discharge by MRI–SiB is shown more delayed than the peak rainfall. As mentioned earlier, the subsurface runoff is the dominant runoff component in MRI–SiB, and subsurface runoff arrives at the stream later than the surface runoff, which causes a delay in peak discharge.

The simulated discharge by both LSMs is evaluated by calculating PBIAS of mean annual discharge, discharge in wet (May to September), and dry season (October to April), as shown in Table 3.3. In terms of mean annual discharge, simulated streamflow by SiBUC forced by MRI–AGCM 3.2S is closer than that by MRI–SiB to the observed river flow. However, the peak discharge in September by MRI–SiB is closer to the observed inflow than SiBUC. All the simulated discharges from both LSMs utilizing RCMs atmospheric forcing tend to underestimate the observed discharge. It is mainly due to the underestimated rainfall by the RCMs. On the other hand, the simulated discharge by SiBUC forced by NHRCM02 is close to the observed

discharge, even though the rainfall from the NHRCM02 underestimated the observed rainfall. That high volume of discharge corresponds to the high surface runoff generated by SiBUC, which is caused by high rainfall intensity and more grid cells with high rainfall amounts in the NHRCM02.

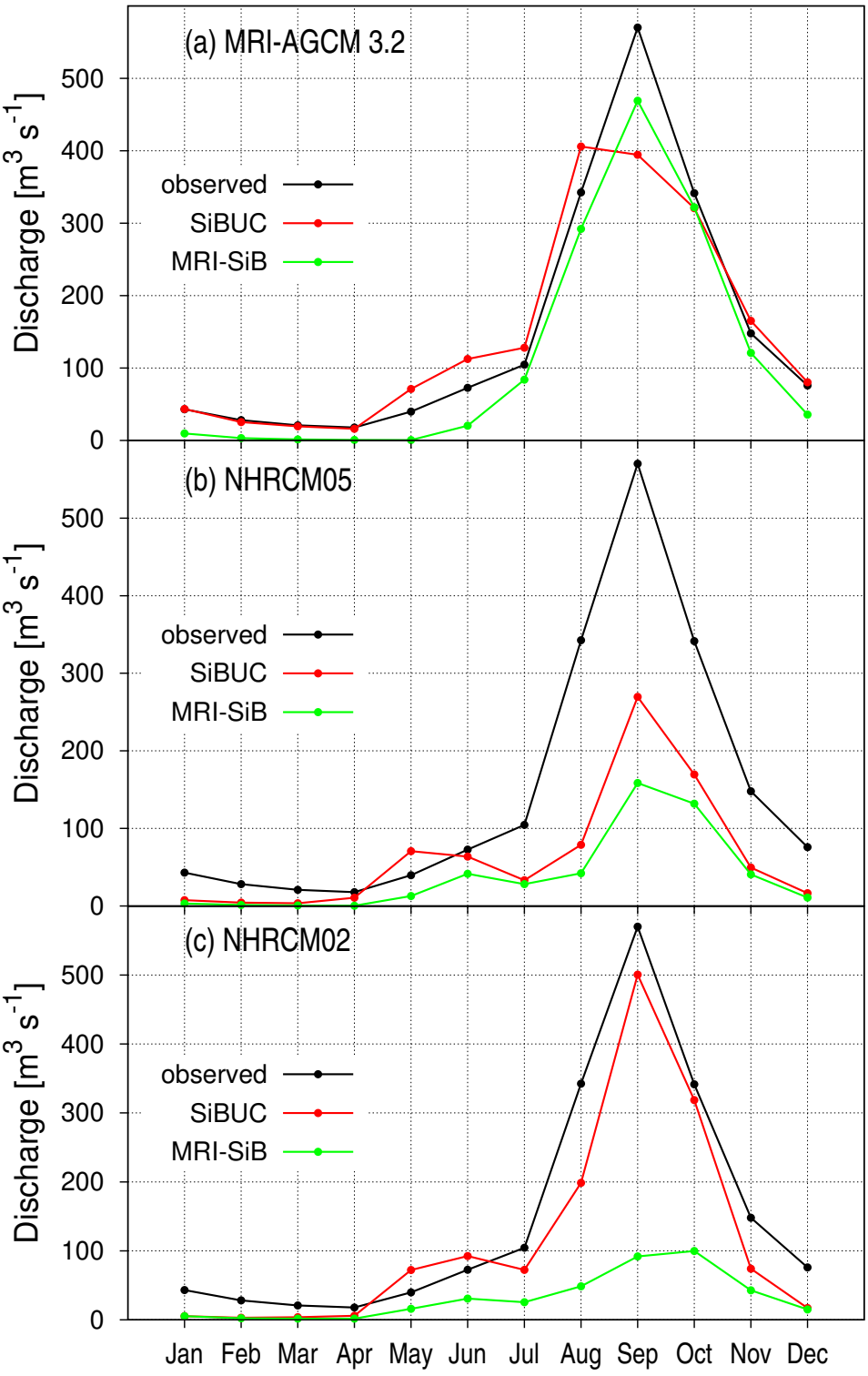

Figure 3.19: Evaluation of simulated discharge and runoff components generated by SiBUC (red line) and MRI–SiB (green line) forced by (a) MRI–AGCM 3.2S, (b) NHRCM05, and (c) NHRCM02. Black line represents observed inflow into Bhumibol Dam.

3.6 Conclusions

This research investigated the applicability of runoff generated by two land surface models (LSMs) for streamflow simulation. Atmospheric output dataset from MRI–AGCM 3.2S with 20–km grid size and NHRCM with 5–km and 2–km grid size were used as forcing for both LSMs. First, we evaluated the rainfall output from each dataset with the observed rainfall. Simulated rainfall from the RCMs underestimated the climatological mean and standard deviation of the observed rainfall. On the other hand, the GCM rainfall was better at reproducing the mean and interannual variability of the observed precipitation. Simulated rainfall by GCM also showed a stronger intensity of daily precipitation than that by the RCMs. The NHRCM02 was able to produce significantly higher intensity than the NHRCM05.

Regarding water budget, SiBUC tended to estimate higher evapotranspiration and lower runoff than MRI–SiB. Different LSMs also generated different runoff characteristics; SiBUC estimated higher surface runoff and lower subsurface runoff than MRI–SiB. Subsurface runoff was the dominant runoff component in MRI–SiB.

Different runoff characteristics have shown some impacts on the simulated streamflow. The peak discharge by SiBUC, formed primarily due to surface runoff generation, is produced soon after the peak rainfall event. On the other hand, MRI–SiB's peak flow shows significantly more delay than the peak rainfall. As MRI–SiB is dominated by subsurface runoff, the rainwater is first infiltrated into the soil before it travels to reach a river, resulting in long lag times.

Then, we evaluated the simulated flow forced runoff from both LSMs by using a flow duration curve. Simulated discharge by SiBUC using GCM forcing tends to overestimate the observed peak and low flow, while it shows well reproducibility of the mid flow. On the other hand, the discharge by MRI–SiB mostly underestimated the observed flow, but it was able to reduce the bias of peak flow by SiBUC.

The simulated monthly streamflow was also evaluated to analyze the LSMs' ability to reproduce the seasonal cycles of observed discharge. Overall, all simulated results by both LSMs could reproduce the seasonal variability of the observed discharge, mainly due to the excellent performance of the climate model in simulating the seasonal variability of the observed rainfall. However, different runoff characteristics between the two LSMs have shown some impacts on the simulated peak discharge. Monthly peak discharge by SiBUC has shown the same timing as peak simulated rainfall. On the other hand, peak discharge by MRI–SiB is mostly more

delayed than the peak rainfall.

Simulated discharge by SiBUC using GCM forcing has shown a low bias for simulating annual flow and that in wet and dry seasons, indicating the excellent ability of runoff by SiBUC in reproducing the observed streamflow. In contrast, discharge by MRI–SiB forced by GCM has improved performance in reproducing the peak observed flow, but it mostly underestimated the observed discharge. Meanwhile, most of the simulated discharges forced by the RCMs show much lower volume than the observed inflow. That is due to the underestimation of the precipitation output by the RCMs.

The present work has shown the different runoff characteristics by each LSM and how it affects the simulated streamflow. Further investigation on the runoff generation mechanisms in each LSM is necessary to understand what has caused such differences.

Chapter 4

Investigation of runoff generation schemes in land surface models

Abstract

The previous chapter has shown different runoff characteristics between SiBUC and MRI–SiB. It is thought that different settings in both LSMs have caused that difference. This study investigated which settings were treated differently in the two land surface models (LSMs). The different settings between both LSMs were adopted in SiBUC to evaluate their impacts on runoff generation. Our investigation identified some different settings in both LSMs that mainly affected the runoff generation and the simulated discharge, such as soil parameters, model structures, and time integration methods on soil schemes (Tinumbang *et al.*, 2020, 2021). It is thought that the findings in this study could provide some insights to identify the sources of uncertainty in LSMs and propose better settings for reproducing the observed river flow.

4.1 Introduction

The Intergovernmental Panel on Climate Change (IPCC, 2021) predicts that water-related disasters increase in magnitude and frequency due to global warming. Previous impact assessment studies (Nohara *et al*., 2006, Hirabayashi *et al*., 2013) sought to project changes in future river discharge using runoff (ROF) output from general circulation models (GCMs) and regional climate models (RCMs). However, they pointed out that the simulated discharge by runoff from GCMs/RCMs is biased. In order to get a better prediction of future river flow, it is necessary to enhance the model performance, including parameters calibration, improving the physical processes in LSMs, and so on.

The importance of understanding the underlying physical processes of runoff generation by GCMs for river flow prediction has been emphasized in the earlier study. For example, Falloon *et al*., (2011) evaluated the simulated discharge forced by runoff output from two GCMs: Hadley Centre GCM (HadCM3; Gordon *et al*., 2000) and Hadley Centre Global Environmental Model version 1 (HadGEM1; Martin *et al*., 2006), against the observed river flow on 24 world ' s major river basins. Both GCMs employed different LSMs. The original version of Met Office Surface Exchange Scheme (MOSES1; Cox *et al*., 1999) is embedded in HadCM3, while Met Office Surface Exchange Scheme version 2 (MOSES2; Essery *et al*., 2001) is employed in HadGEM1. The two LSMs have been developed with similar soil hydrology schemes, but they apply different time integration methods, an explicit method in MOSES1 and an implicit method in MOSES2, to update the soil moisture. They found that in some of the river basins, the bias of simulated river discharge was reflected in the precipitation bias, while in other regions, were not. They suggested that other reasons for errors, such as runoff generation due to errors in soil moisture storage, are likely to cause the bias of the simulated discharge in those basins. Based on their results, it is thought that the choice of time integration method may be important as it affects the calculation of soil moisture. From the literature review, we found that the implicit method is widely applied for the soil schemes in many LSMs, including The Minimum Advanced Treatments of Surface Interaction and RunOff (MATSIRO) (Takata *et al*., 2003) and The Community Noah Land Surface Model with Multi–Parameterization Options (NOAH–MP) (Niu *et al*., 2011).

Although many studies have shown some bias of runoff by LSMs, a detailed investigation on the reasons for bias due to runoff generation processes is still limited in the literature (Falloon

et al., 2011). A study by Takata and Hanasaki (2021) discussed this issue by investigating the behavior of MATSIRO on runoff generation mechanisms. They evaluated the simulated discharge forced by the runoff from MATSIRO against observed inflow at the Bhumibol Dam catchment in Thailand. The runoff by MATSIRO was simulated using the observed meteorological data. They found that the estimated river flow by the original MATSIRO significantly underestimated the observed discharge. Throughout sensitivity analysis by changing saturation threshold to determine the depth of water table, they found that as the level of unsaturated soil moisture decreased, the water table depth became shallow, resulting in the increase of both saturation–excess and base runoff. Consequently, the simulated discharge increased, and the closest estimation to the observed inflow was achieved by changing the saturation threshold from 0% to 50% of porosity. Their findings suggest the importance of the relationship between soil moisture and groundwater depth.

In this study, we also tried to investigate the possible reasons of runoff bias in the two LSMs: SiBUC and MRI–SiB. In our previous study (Tinumbang *et al*., 2019), we found that both LSMs showed different runoff characteristics, even though they were forced by the same forcing from the output of the Non–Hydrostatic Regional Climate Model. MRI–SiB showed a significantly low surface runoff and high subsurface runoff, while SiBUC was the opposite. To have a better understanding of the runoff generation mechanisms in the LSMs and to figure out the reason why such differences happened, we investigated the runoff generation schemes in the two LSMs. To figure out a better model among both LSMs is beyond the scope of this chapter. However, it is thought that the findings of this study could provide some insights into potential causes of runoff bias in both LSMs.

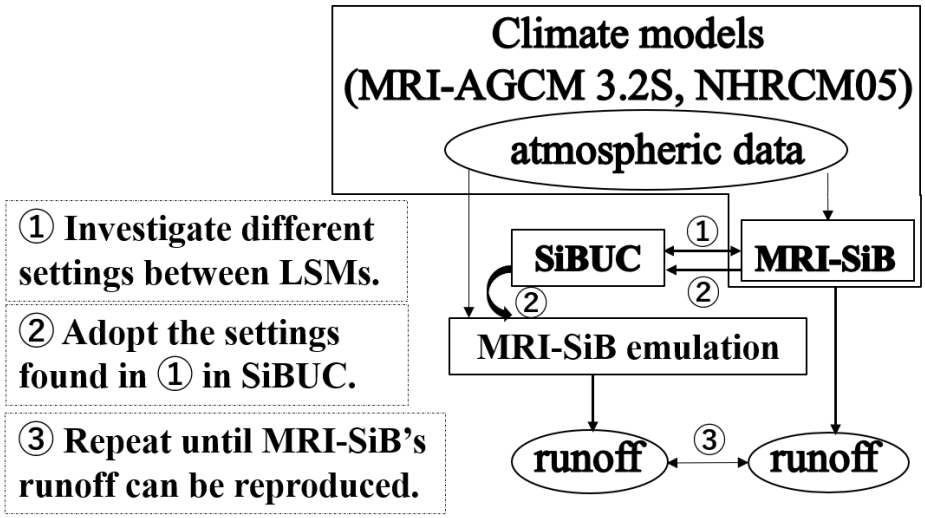

Figure 4.1: Framework of this study.

4.2 Development processes of MRI–SiB emulation model

The previous chapter has shown different runoff characteristics between SiBUC and MRI–SiB and their impacts on the simulated river flow. The different performances of the LSMs might be owing to the differences in land surface parameters, representation of physical processes in the model, parameter settings, etc.

In this study, the possible reasons for the different runoff estimations between the two LSMs are investigated in detail. Figure 4.1 shows a framework of this study.

To understand the underlying processes in the runoff generation mechanisms in the two LSMs, first, we investigated the different settings in both LSMs, mainly by analyzing the source codes of the two LSMs. Next, the different setting that was found is adopted in SiBUC. SiBUC that the setting has been revised to be the same as that of MRI–SiB is called MRI–SiB emulation model. These processes are repeated until the emulation model can reproduce similar runoff characteristics as MRI–SiB.

The atmospheric output data from MRI–AGCM 3.2S and NHRCM with 5–km mesh size (NHRCM05) were used as forcing for the emulation model, and the runoff generated by MRI–SiB embedded in these climate models were set as a reference. Total GCM rainfall was close to the observation, while the RCM rainfall underestimated. Therefore, the simulation by the RCM forcing can be assumed to be set as dry condition.

Table 4.1: Summary of simulation period.

Dataset	Historical simulation period	Spin–up period	Analysis period
MRI–AGCM 3.2S	1979–2003	1979–1983	1984–2003
NHRCM05	1980–1999	1980–1989	1990–1999

The impacts of changing settings on runoff estimation are investigated in detail throughout the development of the emulation model.

Summary of numerical simulation for each atmospheric forcing is shown in Table 4.1. Experimental cases by using MRI–AGCM 3.2S output data were conducted for 25–years period (1979–2003). The first 5–years results were discarded as spin–up, and the last 20–years were used for sensitivity analysis. On the other hand, simulation by NHRCM05 output was performed for 20–years, with the first ten–years were discarded as spin–up, and the rest were utilized for analysis study. The spatial resolution of the emulation model is set to be the same as the atmospheric forcing, and the temporal resolution is set as 1 hour for all forcing.

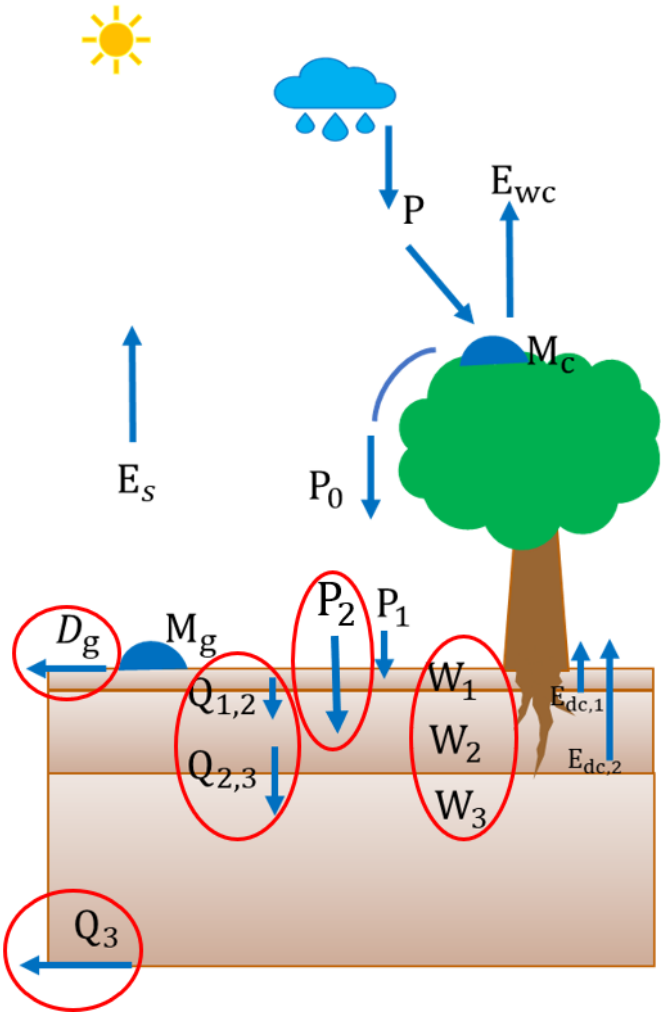

Figure 4.2: Schematic diagram of land surface model. Red circles represent the variables that are estimated differently in both LSMs. *Illustration is reproduced from a schematic figure of green area in SiBUC, based on SiBUC manual.*

4.3 Different settings between SiBUC and MRI–SiB

Both SiBUC and MRI–SiB have been developed based on Simple Biosphere (SiB) (Sellers, *et al.*, 1986). Therefore, the basic structures in both models are similar. For example, soil water movement between adjacent soil layers is described by three soil layers using a simplified Richards equation. However, as two of them have been developed independently, detailed structures, calculation methods, soil parameters, etc., are different. Figure 4.2 shows variables that are treated differently in SiBUC and MRI–SiB, and Table 4.2 summarizes the different settings between both LSMs based on our findings. The list of all variables in this chapter is shown in Table 4.3.

Table 4.2: Different settings between SiBUC and MRI–SiB.

Settings	SiBUC	MRI–SiB
Land surface parameters	set for each soil class	set for each vegetation class
Structure for direct infiltration (P_2)	no	yes
Soil–water flow equation	$Q_{i,i+1} = K\left[\frac{\partial\psi}{\partial z} + 1\right]$	$Q_{i,i+1} = K\left[\frac{\partial\psi}{\partial z}\right]$
Subsurface runoff equation	$Q_3 = \sin\oslash_s K_\mathrm{s} W_3^{2\mathrm{B}+3}$	$Q_3 = \sin\oslash_s K_\mathrm{s} W_3^{2\mathrm{B}+3} + \frac{\psi_2 - \psi_3}{z_3}$
Numerical methods for soil schemes	explicit midpoint method	semi–implicit method

Table 4.3: List of variables for the soil schemes

Symbol	Meaning	Dimension
P	total precipitation	L T^{-1}
P_c	intercepted precipitation	L T^{-1}
P_0	effective precipitation into ground surface	L T^{-1}
P_1	infiltrated rainwater into surface soil layer	L T^{-1}
P_2	infiltrated rainwater into root zone	L T^{-1}
E_s	direct evaporation of water from surface soil layer	M L^{-2} T^{-1}
$E_{\mathrm{dc},1}, E_{\mathrm{dc},2}$	abstraction of soil moisture by transpiration	M L^{-2} T^{-1}
$Q_{1,2}, Q_{2,3}$	soil–water flow between soil layer	L T^{-1}
Q_3	subsurface runoff	L T^{-1}
K_i	hydraulic conductivity of ith layer	L T^{-1}
ψ_i	matric potential of ith layer	L
W_i	soil water content of ith layer	L^3 L^{-3}
D_i	depth of ith soil layer	L
ψ_s	matric potential at saturation	L
θ_s	soil water content at saturation	L^3 L^{-3}
K_s	soil hydraulic conductivity at saturation	L T^{-1}
$\oslash_\mathrm{s}$	mean topographic slope	
B	soil wetness parameter	
ρ_w	density of water	M L^{-3}
Δt	time step	T

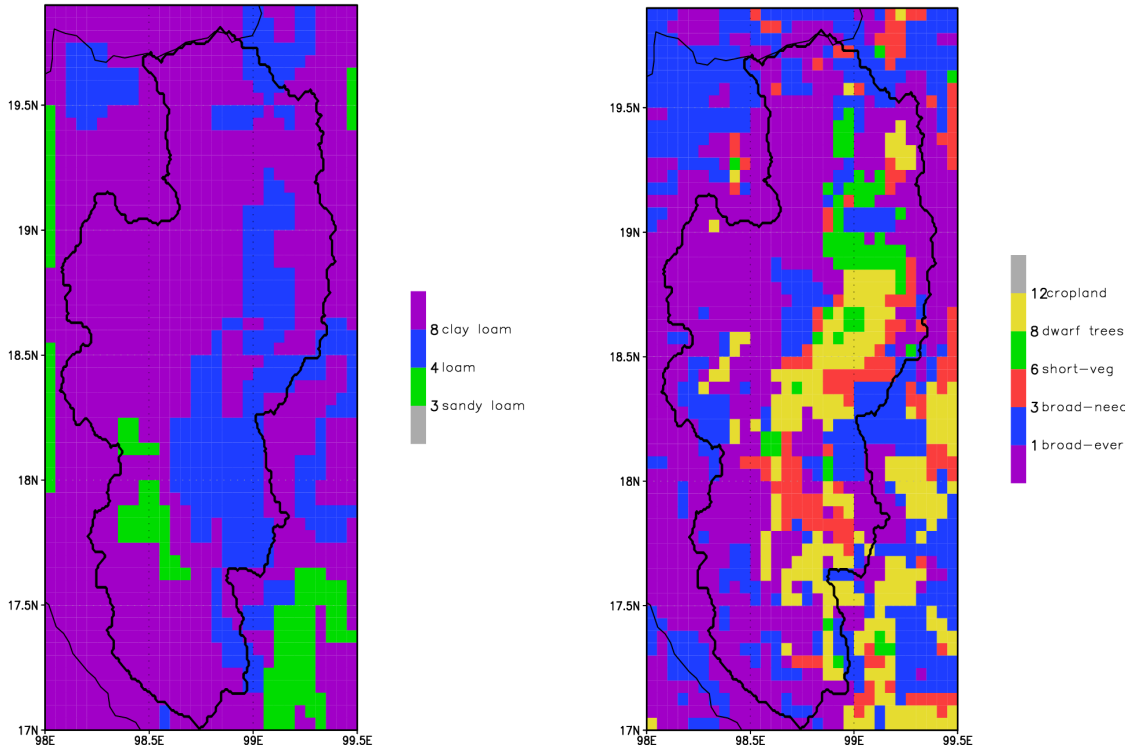

(a) Soil class in SiBUC.

(b) Vegetation class in MRI–SiB.

Figure 4.3: (a) Spatial pattern of soil class in SiBUC obtained from Ecoclimap database. Green, blue, and purple color represents sandy loam, loam, and clay loam, respectively. (b) Spatial pattern of vegetation class in MRI–SiB. Purple, blue, red, green, and yellow color represents broadleaf–evergreen forest, broadleaf and needleleaf forest, short–vegetation, dwarf trees and shrubs, and cropland, respectively. This is for upper part of Ping River Basin.

4.3.1 Land surface parameters

In general, the land surface processes models require a lot of parameters, including parameters related to soil, vegetation, slope, and elevation. Among these parameters, soil parameters are one of the important settings for estimating the runoff in LSMs as they are directly used to calculate the movement of rainwater in the soil. The parameters related to soil include soil characteristics parameters (such as saturated hydraulic conductivity K_{s}, matric potential of saturation ψ_{s}, saturation ratio, B power), and soil depth of three soil layers.

Soil parameters used in SiBUC for simulation in this basin were derived from the Ecoclimap dataset (Masson *et al*., 2003). In SiBUC, soil characteristics parameters are set for each soil

class, following the definition from Cosby *et al*., (1994). On the other hand, in MRI–SiB, all soil parameters, including soil characteristics parameters, are assigned for each vegetation class. Figure 4.3 shows spatial distributions of soil class in SiBUC and vegetation class in MRI–SiB for the upper part of Ping River Basin.

In both LSMs, the parameters are set differently, such as shown in Figure 4.4(a) and Figure 4.4(b), which shows spatial patterns of K_{s} and ψ_{s} in SiBUC and MRI–SiB. Details information is shown in Table 5.6, which describes soil characteristics parameters for each soil class in SiBUC (based on the definition from Cosby *at al*., 1994) and for each vegetation class in MRI–SiB. As seen, MRI–SiB set higher soil characteristic parameters than in SiBUC.

Figure 4.4(c) and Figure 4.4(d) shows spatial distributions of soil layer of the root zone (second layer) and recharge zone (third layer), respectively. In both LSMs, the soil thickness of surface soil layer is set to be the same, equal to 0.02 m. Meanwhile, the depth of the deeper layers is set differently. For this catchment, the depth of root and recharge zone in MRI–SiB is set between 0.5–1.5 m and 1.5–3.5 m, respectively, depending on vegetation type. SiBUC tends to set much thicker depth than MRI–SiB. The maximum depth in SiBUC is set up to 12 m.

Parameters related to vegetation, such as greenness fraction, leaf area index (LAI), and the fraction of photosynthetically active radiation (FPAR), are also important for water budget estimation, especially for transpiration. Both LSMs also set the vegetation parameters differently. For developing the emulation model, not all vegetation parameters of MRI–SiB can be adopted in SiBUC, as the two LSMs have different vegetation schemes. In MRI–SiB, the vegetation is represented by two layers: canopy and ground cover. In SiBUC, both canopy and ground cover are called canopy, and treated together in one vegetation layer.

Figure 4.5 shows spatial patterns of greenness fraction in the two LSMs. This parameter is set to only one vegetation layer (canopy) in SiBUC, and two vegetation layers, canopy and ground cover, in MRI–SiB. For this analysis, only the parameters for canopy in MRI–SiB are used, and the parameters for ground cover are not considered for developing the emulation model.

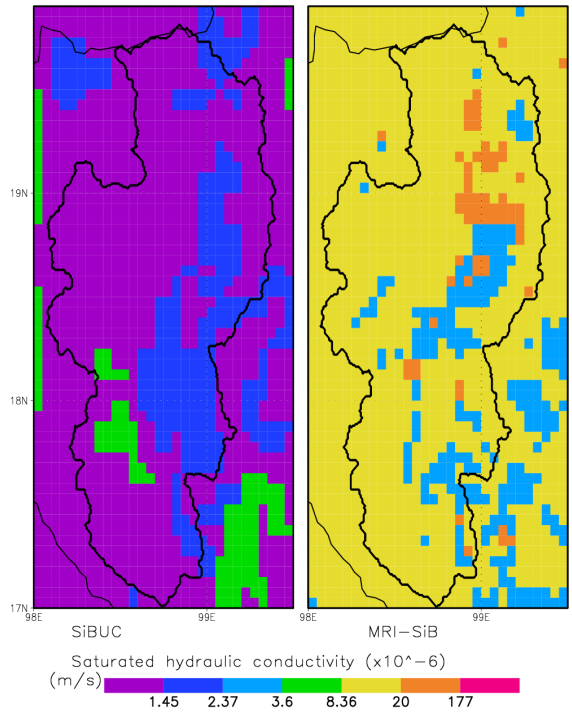

(a) Saturated hydraulic conductivity.

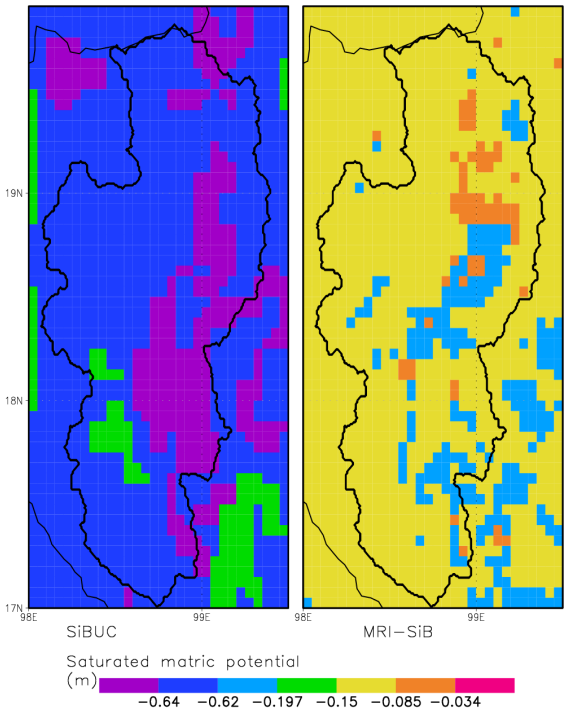

(b) Matric potential of saturation

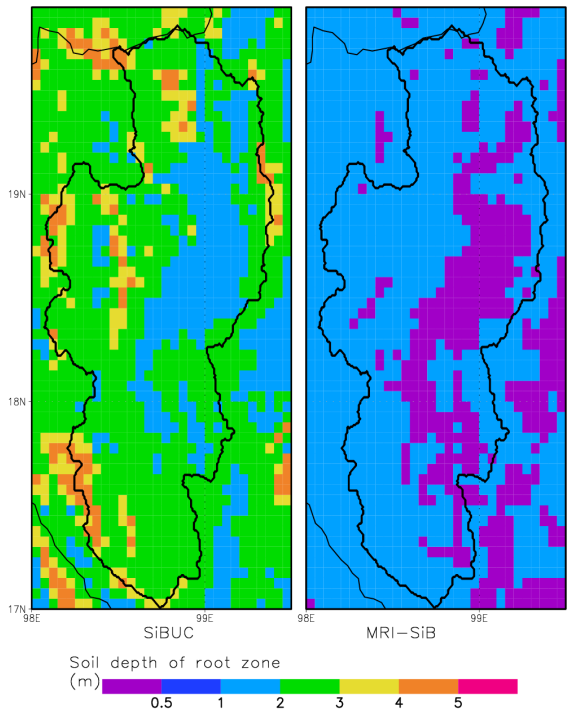

(c) Soil depth of root zone.

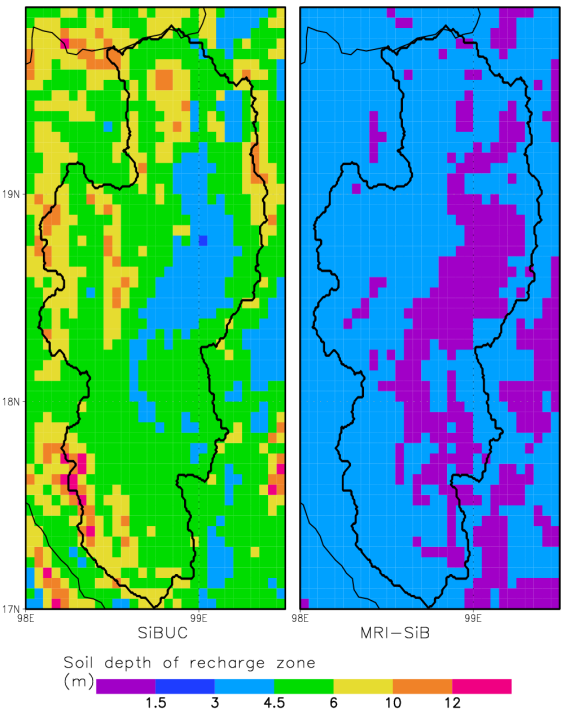

(d) Soil depth of recharge layer.

Figure 4.4: Spatial patterns of soil parameters in SiBUC (left) and MRI–SiB (right).

Table 4.4: Comparison of soil characteristic parameters in SiBUC and MRI–SiB.

(a) Soil characteristic parameters in SiBUC (based on Cosby *at al*., 1984).

Soil class	K_s (m s^{-1})	ψ_s (m)	θ_s	B
Sandy loam	8.35×10^{-6}	-0.16	0.419	4.34
Loam	2.36×10^{-6}	-0.65	0.476	5.25
Clay loam	1.44×10^{-6}	-0.63	0.478	8.41

(b) Soil characteristic parameters value in MRI–SiB.

Vegetation class	K_s (m s^{-1})	ψ_s (m)	θ_s	B
Broadleaf–evergreen forest	2.00×10^{-5}	-0.086	0.42	7.12
Broadleaf and needleleaf forest	2.00×10^{-5}	-0.086	0.42	7.12
Short–vegetation	2.00×10^{-5}	-0.086	0.42	7.12
Dwarf trees and shrubs	1.76×10^{-4}	-0.035	0.435	4.05
Cropland	3.50×10^{-6}	-0.198	0.458	7.80

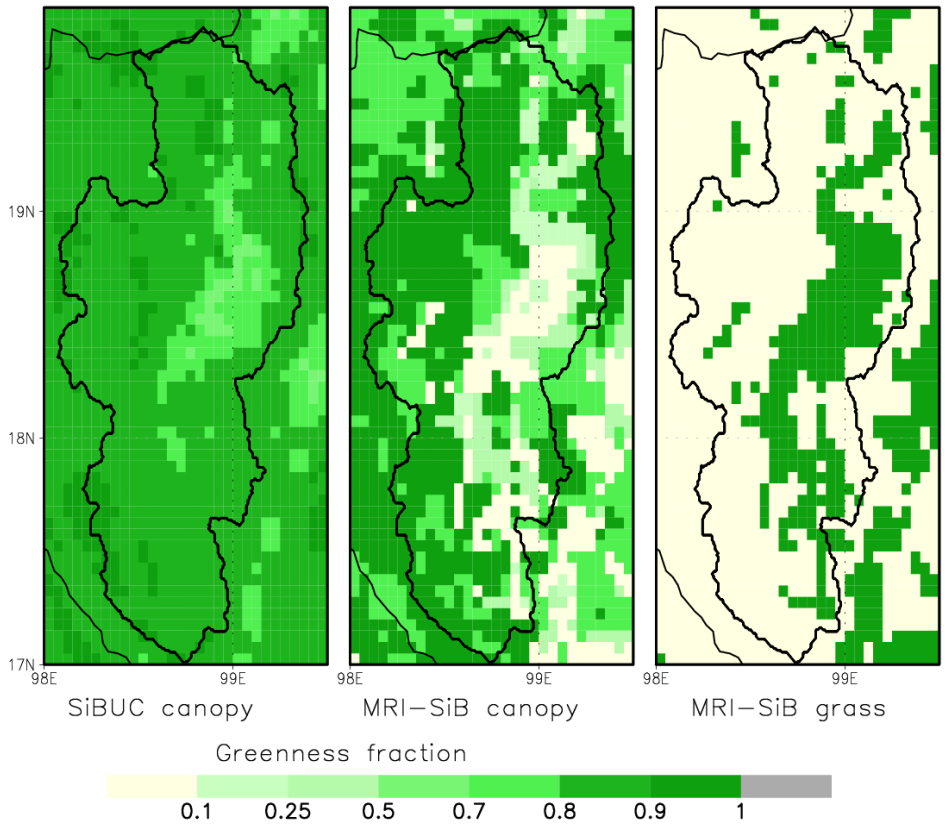

Figure 4.5: Spatial patterns of greenness fraction for canopy layer in SiBUC (left), canopy layer in MRI–SiB (middle), and ground cover layer in MRI–SiB (right).

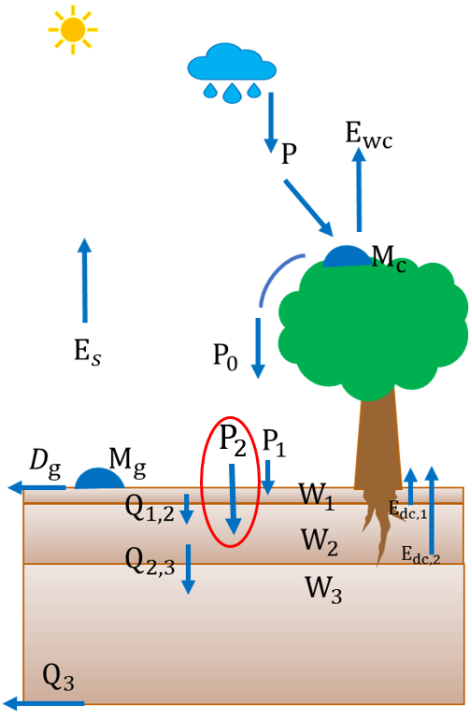

Figure 4.6: Similar to Figure 4.2. Red circles shows a structure for direct infiltration from ground surface into second soil layer, called P_2.

4.3.2 Structure for direct infiltration from ground surface into deeper soil layer

By investigating MRI–SiB source codes, we found a structure for direct infiltration from the ground surface into the root zone. In this study, that structure is called as "P_2", indicated in Figure 4.10. In SiBUC, when rainwater reaches the ground, some rainwater can infiltrate into the surface soil layer. While, in MRI–SiB, rainfall is able to infiltrate into the surface soil layer and directly infiltrate into the root zone. That structure was originally incorporated in the global circulation model (GCM) developed by MRI because large time–steps setting (more than one–hour) in the GCM had caused less infiltrated rainwater in the soil. In the NHRCM, this scheme is still employed.

The incorporation of P_2 structure affects the surface runoff calculation. In both LSMs, two types of surface runoff is considered; infiltration–excess runoff (Hortonian runoff) and saturation–excess runoff (Dunne runoff). Hortonian runoff is calculated when the rainfall intensity exceeds the infiltration capacity. In SiBUC, saturation–excess runoff is estimated when soil moisture of surface soil layer has reached saturation. As P_2 structure exists in the MRI–SiB, Dunne runoff is calculated when the soil moisture of both surface soil layer and root zone has saturated.

4.3.3 Governing equation for water movement between adjacent soil layers

Another difference in both LSMs is the governing equations for estimating soil–water flow. In SiBUC, the transfer of water between each soil layer is calculated based on Darcy's Law by considering hydraulic diffusion and gravitational drainage of water in the soil, shown in Eq. (4.1). The term "1" in Eq. (4.1) accounts for gravitational drainage. In MRI–SiB, the gravitational drainage is neglected, and soil–water flow is estimated only based on the hydraulic diffusion, as shown in Eq. (4.2).

$$Q_{i,i+1} = K\left[\frac{\partial\psi}{\partial z} + 1\right] = \overline{K}\left[\frac{2\left(\psi_i - \psi_{i+1}\right)}{D_i + D_{i+1}} + 1\right] \quad \text{(i=1,2)} \tag{4.1}$$

$$Q_{i,i+1} = K\left[\frac{\partial\psi}{\partial z}\right] = \overline{K}\left[\frac{2\left(\psi_i - \psi_{i+1}\right)}{D_i + D_{i+1}}\right] \quad \text{(i=1,2)} \tag{4.2}$$

with,

$$\overline{K} = \frac{D_i K_i + D_{i+1} K_{i+1}}{D_i + D_{i+1}} \tag{4.3}$$

In both LSMs, hydraulic conductivity and matric potential are given as a function of soil moisture based on the formulae of Clapp and Hornberger (1978), as shown in Eq. (4.4) and Eq. (4.5), respectively.

$$K_i = K_{\mathrm{s}} W_i^{2\mathrm{B}+3} \tag{4.4}$$

$$\psi_i = \psi_{\mathrm{s}} W_i^{-\mathrm{B}} \tag{4.5}$$

4.3.4 Governing equation for subsurface runoff estimation

In SiBUC, subsurface runoff calculation is only determined by gravitational drainage, shown in Eq. (4.6). While, in MRI–SiB, both gravitational drainage and potential gradients between root zone and recharge layer are considered for calculating subsurface runoff, as shown in Eq. (4.7).

$$Q_3 = \sin\oslash_s K_{\mathrm{s}} W_3^{2\mathrm{B}+3} \tag{4.6}$$

$$Q_3 = \sin\oslash_s K_{\mathrm{s}} W_3^{2\mathrm{B}+3} + \frac{\psi_2 - \psi_3}{D_3} \tag{4.7}$$

Table 4.5: Considered variables for updating soil moisture at the next time step in SiBUC and MRI–SiB.

Variables	SiBUC	MRI–SiB
Soil moisture	✓	×
Matric potential	✓	✓
Hydraulic conductivity	✓	×

4.3.5 Time integration methods for soil schemes

To update the soil moisture for each time step, both LSMs apply different time integration methods. The variables that are considered for updating soil moisture at the next time step are also different in both models, as shown in Table 4.5.

In SiBUC, the explicit–midpoint method is applied to soil moisture, matric potential, and hydraulic conductivity. This method is, also known as the modified Euler method, solving the differential equation by evaluating the slope of the solution at the midpoint between current and next time step. Algorithm to update soil moisture at next time step in SiBUC is shown in Figure 4.7. First, by using initial soil moisture, estimated from the previous time step, matric potential in Eq. (4.5), hydraulic conductivity in Eq. (4.4), and soil–water flow between adjacent soil layer in Eq. (4.1), are calculated. Then, the Richards equation, shown in Eq. (4.8)–Eq. (4.10), is solved to update the soil moisture.

$$\frac{\partial W_1}{\partial t} = \frac{1}{\theta_{\rm s} D_1}\left[P_1 - Q_{1,2} - \frac{E_{\rm s} + E_{\rm dc,1}}{\rho_{\rm w}}\right] \tag{4.8}$$

$$\frac{\partial W_2}{\partial t} = \frac{1}{\theta_{\rm s} D_2}\left[Q_{1,2} - Q_{2,3} - \frac{E_{\rm dc,2}}{\rho_{\rm w}}\right] \tag{4.9}$$

$$\frac{\partial W_3}{\partial t} = \frac{1}{\theta_{\rm s} D_3}\left[Q_{2,3} - Q_3\right] \tag{4.10}$$

Next, take an average of initial and updated soil moisture. Then, the matric potential, hydraulic conductivity, and soil–water flow is again calculated by using the mean soil moisture value to solve the Richards equation.

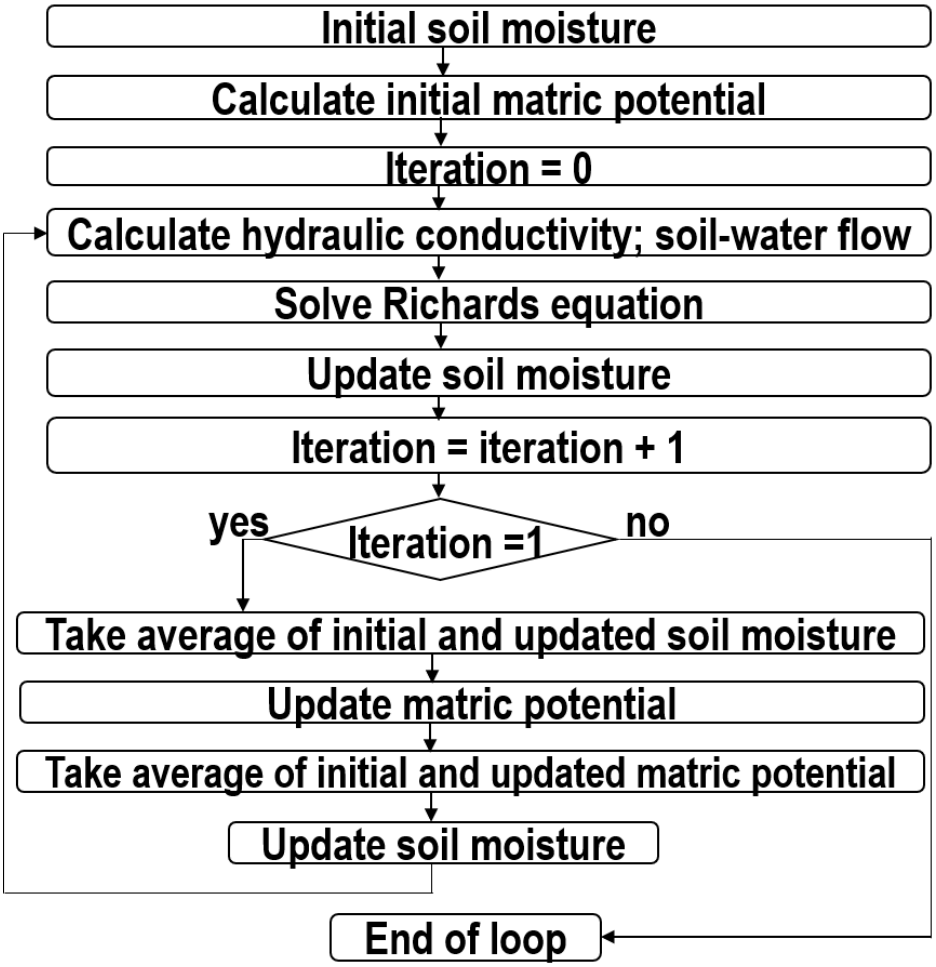

Figure 4.7: Algorithm of explicit–midpoint method applied in SiBUC to update soil moisture at next time step.

In MRI–SiB, semi–implicit method is applied to matric potential by linearizing about soil moisture using a Taylor expansion, expressed by:

$$\psi_i^{t+\Delta t} = \psi_i^t + \frac{\partial \psi_i^t}{\partial W_i^t}\frac{\partial W_i^t}{\partial t}\Delta t \tag{4.11}$$

Then, Eq. (4.11) is inserted into Eq. (4.2) for estimating the soil–water flow in the next time step, becomes Eq. (4.12).

$$Q_{i,i+1} = K\left[\frac{\partial \psi}{\partial z}\right] = \overline{K}\left[\frac{2\left(\psi_i + \frac{\partial \psi_i}{\partial W_i}\frac{\partial W_i}{\partial t}\Delta t - \psi_{i+1} - \frac{\partial \psi_{i+1}}{\partial W_{i+1}}\frac{\partial W_{i+1}}{\partial t}\Delta t\right)}{D_i + D_{i+1}}\right] \quad \text{(i=1,2)} \tag{4.12}$$

Assume that:

$$\overline{K}\left[\frac{2\left(\psi_i-\psi_{i+1}\right)}{D_i+D_{i+1}}\right]=Q_{i,i+1(\exp)} \quad \text{(i=1,2)} \tag{4.13}$$

Then, Eq. (4.12) can be rewritten as Eq. (4.14).

$$Q_{i,i+1}=Q_{i,i+1(\exp)}+\overline{K}\left[\frac{2\left(\frac{\partial\psi_{\mathrm{i}}}{\partial W_{\mathrm{i}}}\frac{\partial W_{\mathrm{i}}}{\partial t}\Delta t-\frac{\partial\psi_{\mathrm{i+1}}}{\partial W_{\mathrm{i+1}}}\frac{\partial W_{\mathrm{i+1}}}{\partial t}\Delta t\right)}{D_i+D_{i+1}}\right] \quad \text{(i=1,2)} \tag{4.14}$$

Eq. (4.14) can be inserted into Richards equations for each soil layer, shown in Eq. (4.8)–Eq. (4.10), to become Eq. (4.16)–Eq. (4.18) for updating the soil moisture of the next time step. Eq. (4.9) is revised as follow to consider P_2 structure.

$$\frac{\partial W_2}{\partial t}=\frac{1}{\theta_{\mathrm{s}}D_2}\left[P_2+Q_{1,2}-Q_{2,3}-\frac{E_{\mathrm{dc},2}}{\rho_{\mathrm{w}}}\right] \tag{4.15}$$

$$\frac{\partial W_1}{\partial t}=\frac{1}{\theta_{\mathrm{s}}D_1}\left[P_1-Q_{1,2(\exp)}-K_{1,2}\left[\frac{2\left(\frac{\partial\psi_1}{\partial W_1}\frac{\partial W_1}{\partial t}\Delta t-\frac{\partial\psi_2}{\partial W_2}\frac{\partial W_2}{\partial t}\Delta t\right)}{D_1+D_2}\right]-\frac{E_{\mathrm{s}}+E_{\mathrm{dc},1}}{\rho_{\mathrm{w}}}\right] \tag{4.16}$$

$$\begin{aligned}\frac{\partial W_2}{\partial t}=\frac{1}{\theta_{\mathrm{s}}D_2}\Bigg[&P_2+Q_{1,2(\exp)}+K_{1,2}\left[\frac{2\left(\frac{\partial\psi_1}{\partial W_1}\frac{\partial W_1}{\partial t}\Delta t-\frac{\partial\psi_2}{\partial W_2}\frac{\partial W_2}{\partial t}\Delta t\right)}{D_1+D_2}\right]\\&-Q_{2,3(\exp)}-K_{2,3}\left[\frac{2\left(\frac{\partial\psi_2}{\partial W_2}\frac{\partial W_2}{\partial t}\Delta t-\frac{\partial\psi_3}{\partial W_3}\frac{\partial W_3}{\partial t}\Delta t\right)}{D_2+D_3}\right]-\frac{E_{\mathrm{dc},2}}{\rho_{\mathrm{w}}}\Bigg]\end{aligned} \tag{4.17}$$

$$\frac{\partial W_3}{\partial t}=\frac{1}{\theta_{\mathrm{s}}D_3}\left[Q_{2,3(\exp)}+K_{2,3}\left[\frac{2\left(\frac{\partial\psi_2}{\partial W_2}\frac{\partial W_2}{\partial t}\Delta t-\frac{\partial\psi_3}{\partial W_3}\frac{\partial W_3}{\partial t}\Delta t\right)}{D_2+D_3}\right]-Q_3\right] \tag{4.18}$$

Eq. (4.16)-Eq. (4.18) can be rewritten as following matrices.

$$\begin{bmatrix} \frac{\theta_s D_1}{\Delta t} + \frac{2K_{1,2}}{D_1+D_2}\frac{\partial \psi_1}{\partial W_1} & \frac{2K_{1,2}}{D_1+D_2}\frac{\partial \psi_2}{\partial W_2} & 0 \\ -\frac{2K_{1,2}}{D_1+D_2}\frac{\partial \psi_1}{\partial W_1} & \frac{\theta_s D_2}{\Delta t} + \frac{2K_{1,2}}{D_1+D_2}\frac{\partial \psi_2}{\partial W_2} + \frac{2K_{2,3}}{D_2+D_3}\frac{\partial \psi_2}{\partial W_2} & -\frac{2K_{2,3}}{D_2+D_3}\frac{\partial \psi_3}{\partial W_3} \\ 0 & -\frac{2K_{2,3}}{D_2+D_3}\frac{\partial \psi_2}{\partial W_2} & \frac{\theta_s D_3}{\Delta t} + \frac{2K_{2,3}}{D_2+D_3}\frac{\partial \psi_3}{\partial W_3} \end{bmatrix} \begin{bmatrix} \frac{\partial W_1}{\partial t}\Delta t \\ \frac{\partial W_2}{\partial t}\Delta t \\ \frac{\partial W_3}{\partial t}\Delta t \end{bmatrix}$$

$$= \begin{bmatrix} P_1 - Q_{1,2(\exp)} - \frac{E_s + E_{dc,1}}{\rho_w} \\ P_2 + Q_{1,2(\exp)} - \frac{E_{dc,2}}{\rho_w} \\ Q_{2,3(\exp)} - Q_3 \end{bmatrix} \tag{4.19}$$

Note that:

$$\frac{\partial \psi_i}{\partial W_i} = \frac{\partial \left(\psi_s W_i^{-B}\right)}{\partial W_i} = -B\psi_s W_i^{-B-1} = \frac{-B\psi_i}{W_i} \tag{4.20}$$

The above matric can be solved by using the Gauss–Jordan Elimination method to derive the solution of Richards Equation.

Table 4.6: Experimental designs by emulation model. Experiment A and B were performed by using SiBUC and MRI–SiB parameters, respectively. Control experiment is the simulation by original parameters and structures of SiBUC.

Changes	Experiments													
	Control	A						B						
		1	2	3	4	5	6	0	1	2	3	4	5	6
1. Land surface parameters SiBUC $\rightarrow$ MRI–SiB	–	–	–	–	–	–	–	✓	✓	✓	✓	✓	✓	✓
2. Incorporating P_2 scheme	–	✓	–	–	✓	–	✓	–	✓	–	–	✓	–	✓
3. Soil–water flow equation $Q_{i,i+1} = K\left[\frac{\partial\psi}{\partial z}+1\right] \rightarrow Q_{i,i+1} = K\left[\frac{\partial\psi}{\partial z}\right]$	–	–	✓	–	✓	–	✓	–	–	✓	–	✓	–	✓
4. Subsurface runoff equation $Q_3 = \sin\oslash_s K_\mathrm{s} W_3^{2\mathrm{B}+3} \rightarrow Q_3 = \sin\oslash_s K_\mathrm{s} W_3^{2\mathrm{B}+3} + \frac{\psi_2-\psi_3}{D_3}$	–	–	–	✓	✓	–	✓	–	–	–	✓	✓	–	✓
5. Time integration methods Explicit $\rightarrow$ semi–implicit	–	–	–	–	–	✓	✓	–	–	–	–	–	✓	✓

4.4 Experimental designs by MRI–SiB emulation model

Table 4.6 shows a summary of experimental cases performed by changing land surface parameters, model structures, and time integration methods in SiBUC. This study aims not to develop an MRI–SiB emulation model but to investigate in detail the impacts of different settings in both LSMs. A control experiment is a simulation performed by the original parameters and structures of SiBUC. Experiment A and B were performed by using SiBUC and MRI–SiB parameters, respectively. Experiment 0 (E0) was conducted to investigate the impacts of changing land surface parameters. E1–E4 were performed to analyze the impacts of different model structures in the two LSMs; by incorporating P_2 structure, neglecting gravitational drainage in soil–water flow, and considering hydraulic diffusion for subsurface runoff calculation, respectively. E5 was performed to examine the impacts of different time integration methods in the soil schemes by changing from explicit midpoint method to semi–implicit method). E6 was carried out by setting the same model structures and time integration methods as MRI–SiB. The impact changing setting was evaluated in terms of water budget and runoff components.

4.5 Changes of water budget

4.5.1 Overall impacts

The results of 20–years–mean annual water budget using MRI–AGCM 3.2S forcing by MRI–SiB, SiBUC, and each experimental case is shown in Figure 4.8. 20–years–mean annual rainfall by MRI-AGCM 3.2S is 1144 mm. It is used for all the experimental cases.

As mentioned in the previous section, the evapotranspiration by MRI–SiB counts for about 88% of rainfall, and the rest is runoff. Subsurface runoff is the dominant runoff component, as surface runoff only counts for about 2% of the total runoff. The results of the original SiBUC parameters and structures are set as a control experiment in this analysis. The estimated runoff by SiBUC was about 33% higher than that of MRI–SiB. Surface runoff and subsurface runoff counts for 30% and 70% of the total runoff, respectively.

Figure 4.9 shows the results of 10–years–mean annual water budget using NHRCM05 forcing by MRI–SiB, SiBUC, and each experimental case. The basin average annual rainfall by NHRCM05 is less than 700 mm. As mentioned earlier, MRI–SiB results showed an imbalance of water budget because it was simulated by time–slice integration method. Total runoff by MRI–SiB is about 7% of total rainfall, and similar to the results by MRI–AGCM 3.2S, it was mostly generated as subsurface runoff. Meanwhile, in the control experiment (by using original SiBUC parameters and structures), the surface runoff counts for about 87% of total runoff, and the rest is subsurface runoff. The ratio of surface runoff by SiBUC using NHRCM05 is higher than that by using MRI–AGCM 3.2S forcing.

Impacts of adopting MRI–SiB settings in SiBUC are described as follows.

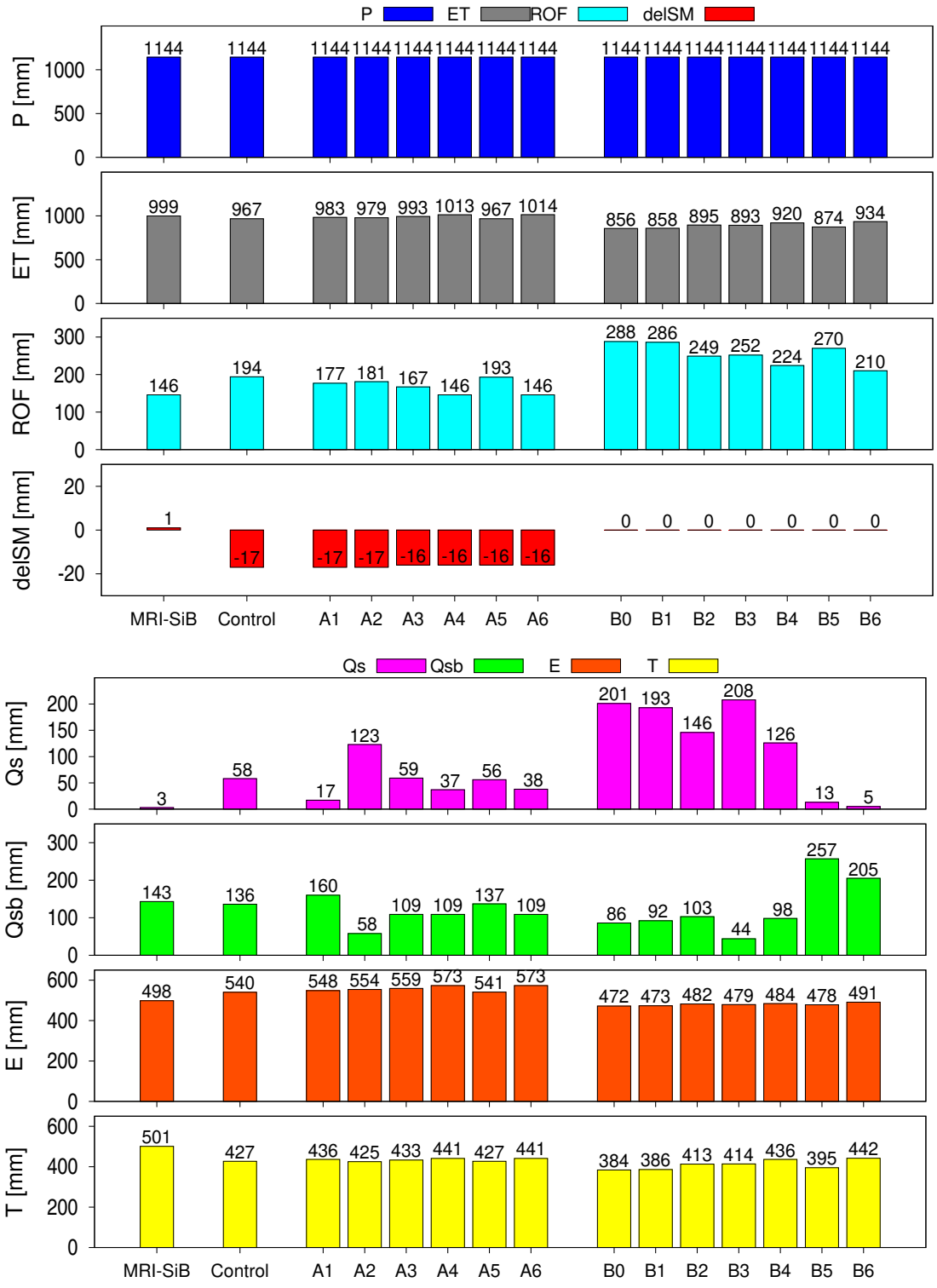

Figure 4.8: 20–years–mean annual water budget component by MRI–SiB, control, and each case. Top: blue, gray, light blue, and red bars represent rainfall (P), evapotranspiration (ET), runoff (ROF), and change of soil moisture (delSM). Bottom: pink, green, yellow, and orange bars represent surface runoff (Qs), subsurface runoff (Qsb), transpiration (T), and evaporation (E). Forcing data is MRI–AGCM 3.2S atmospheric data.

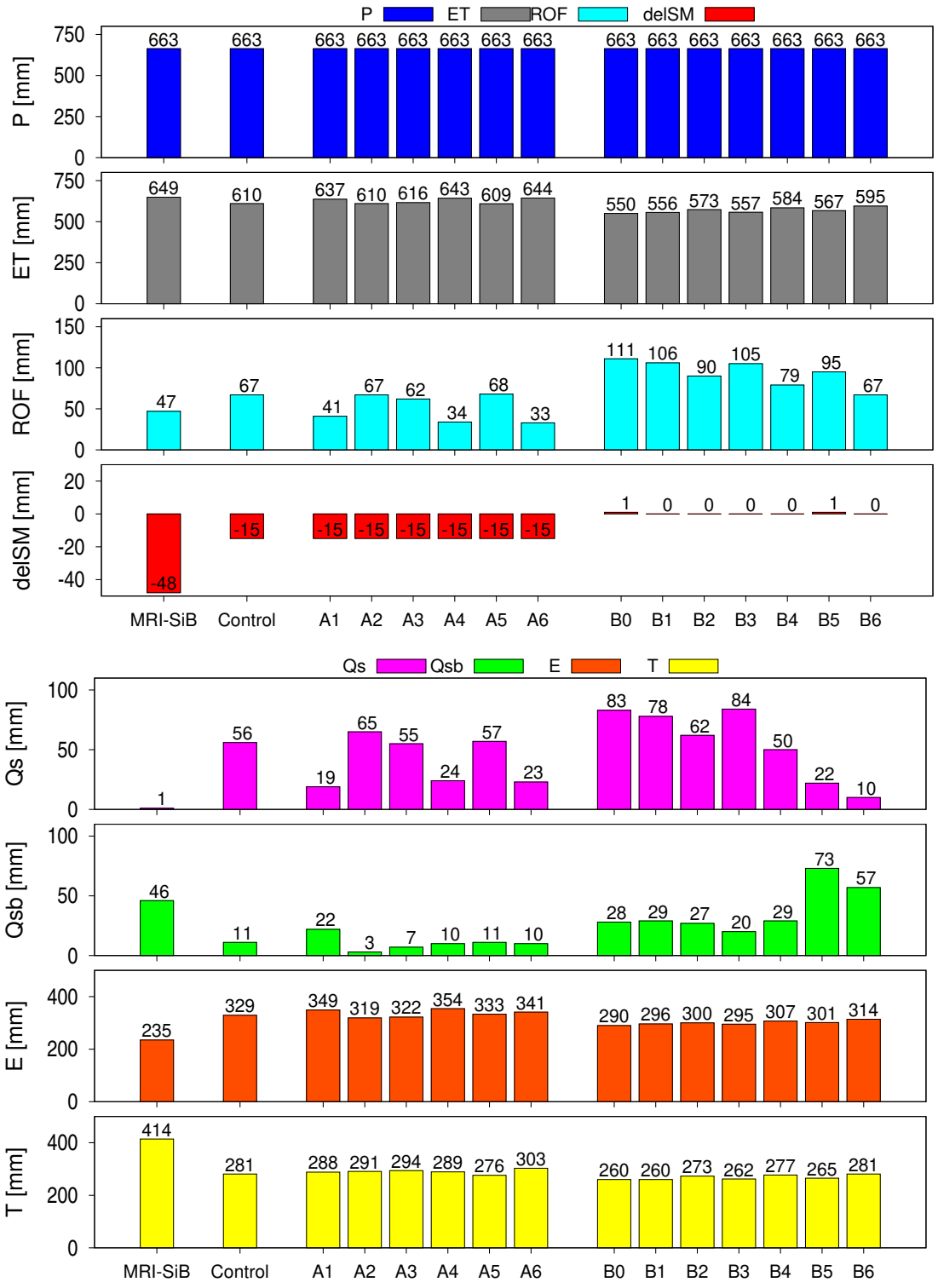

Figure 4.9: Similar to the previous figure but for 10–years–mean with the forcing is NHRCM05 atmospheric data.

Table 4.7: Mean annual runoff components (unit: mm). Experiment 0 is changing MRI–SiB parameters.

Forcing	MRI–AGCM 3.2S			NHRCM05		
Experiment	MRI–SiB	Control	B0	MRI–SiB	Control	B0
Qs	3	58	201	1	56	83
Qsb	143	136	86	46	11	28

4.5.2 Impacts of changing land surface parameters

Table 4.7 shows a comparison of mean annual water budget components between MRI–SiB, control, and B0 experiment (changing MRI–SiB land surface parameters). The estimated evapotranspiration is higher in B0, and runoff is lower than the control experiment in both forcings. Surface runoff is higher than the control experiment in all forcing. The increase of surface runoff might be due to thinner soil depth in MRI–SiB parameters than that in SiBUC. Thinner soil depth could increase the surface runoff since the soil has a lower capacity to store the rainwater.

Meanwhile, subsurface runoff using GCM forcing is lower, and it is higher than the control experiment by using RCM forcing. It is thought there are two possible reasons. The decrease of subsurface runoff might happen because of the higher estimation of surface runoff. As some rainwater has already been generated as surface runoff, subsurface runoff becomes decreases due to lower infiltrated rainwater.

On the other hand, subsurface runoff could increase because the parameters in MRI–SiB related to infiltration, such as saturated hydraulic conductivity and saturated matric potential, are set to be much higher (about 10–fold) than that in SiBUC. Both settings could increase the vertical infiltration rates and increase the subsurface runoff.

By only changing MRI–SiB soil parameters in SiBUC, surface runoff is much higher, and subsurface runoff is lower than that in MRI–SiB. These results show that changing the soil parameters alone could not emulate the MRI–SiB results.

4.5.3 Impacts of incorporating direct infiltration structure into deeper soil layer

The results by incorporating P_2 structure (A1 and B1 cases) shows the surface runoff decreases and subsurface increases compared to the results without P_2 structure, as seen in Table 4.8. As seen in Figure 4.10, surface runoff reduces because by adopting P_2 structure, the infiltrated rainwater in the soil increases, and surface runoff (Dunne runoff) is generated when both surface soil and root zone has reached saturation. As the infiltrated water increases, the subsurface runoff also becomes higher.

In both GCM and RCM forcings, the impacts of surface runoff reduction due to P_2 structure is higher by using SiBUC parameters than by MRI–SiB parameters. It can be due to the differences in soil depth. Higher soil depth can store more rainwater than in the thinner soil.

Table 4.8: Mean annual runoff components (unit: mm). Experiment 1 is incorporating P_2 scheme.

Forcing	MRI–AGCM 3.2S					NHRCM05				
Experiment	MRI–SiB	Control	A1	B0	B1	MRI–SiB	Control	A1	B0	B1
Qs	3	58	17	201	193	1	56	19	83	78
Qsb	143	136	160	86	92	46	11	22	28	29

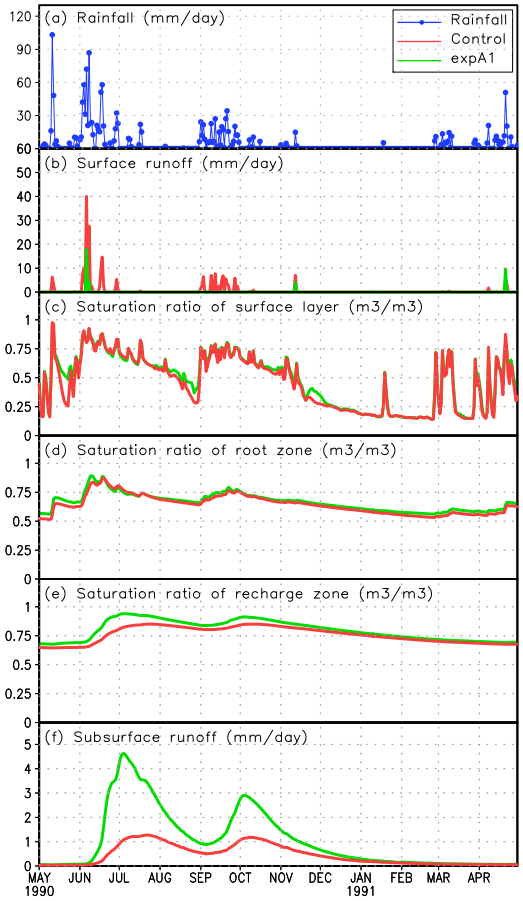

(a) Simulation by SiBUC soil parameters. Red and green lines represent the simulation without (control) and with P_2 structure (A1), respectively.

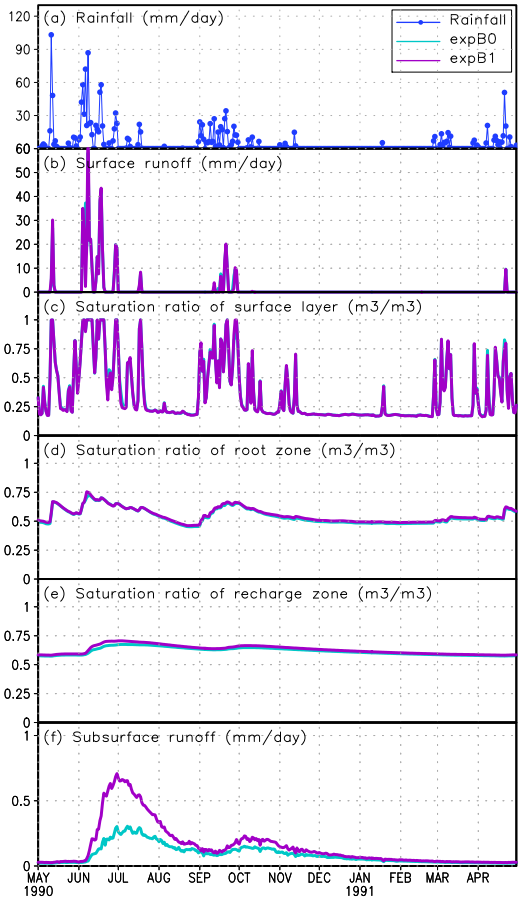

(b) Simulation by MRI–SiB soil parameters. Light blue and purple lines represent the simulation without (B0) and with P_2 structure (B1), respectively.

Figure 4.10: Time series of daily rainfall (a), surface runoff (b), saturation ratio of top to bottom layers (c-e), and subsurface runoff (f) in 1990. This is for investigating the impacts of considering P_2 structure. Forcing is NHRCM05 atmospheric data.

Table 4.9: Mean annual runoff components (unit: mm). Experiment 2 is neglecting gravitational drainage in Darcy's Law.

Forcing	MRI–AGCM 3.2S					NHRCM05				
Experiment	MRI–SiB	Control	A2	B0	B2	MRI–SiB	Control	A2	B0	B2
Qs	3	58	123	201	146	1	56	65	83	62
Qsb	143	136	58	86	103	46	11	3	28	27

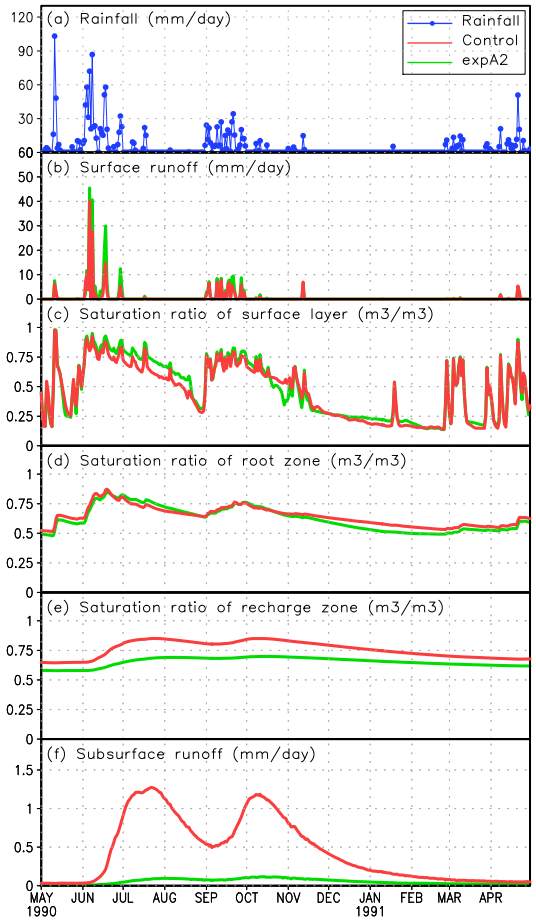

(a) Similar to Figure 4.10(a) but for the simulation which consider (control) and neglecting gravitational drainage (A2) with SiBUC parameters.

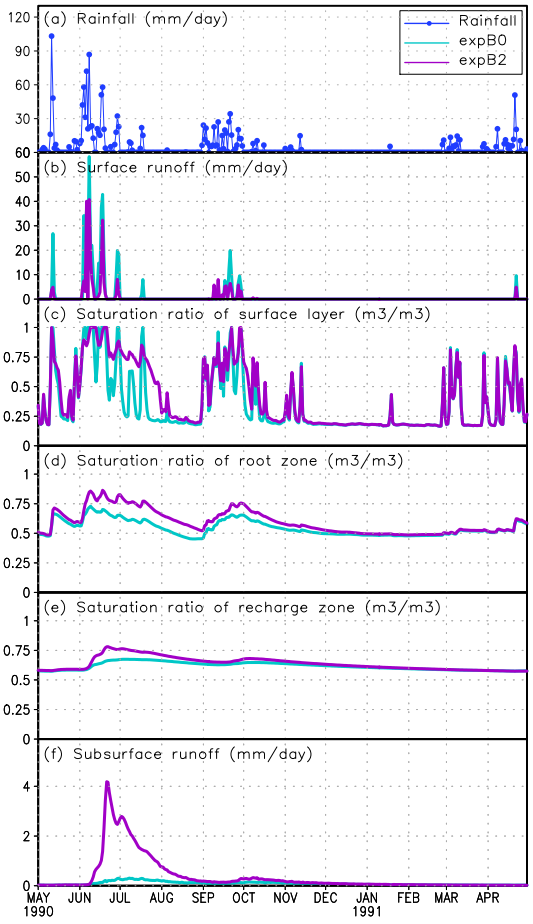

(b) Similar to Figure 4.10(b) but for the simulation which consider (B0) and neglecting gravitational drainage (B2) with MRI–SiB parameters.

Figure 4.11: Similar to Figure 4.10, but for investigating the impacts of neglecting gravitational drainage for estimating soil–water flow.

4.5.4 Impacts of neglecting gravitational drainage for estimating soil–water flow between adjacent soil layers

Neglecting gravitational drainage in Darcy's Law shows different impacts using SiBUC parameters (A2) and MRI–SiB parameters (B2), as seen in Figure 4.9. Using SiBUC parameters in both GCM and RCM forcings show an increase in surface runoff and decrease of subsurface runoff compared to the control experiment. In contrast, by using MRI–SiB parameters, compared to the B0 case, which considers the gravitational flow, the impacts of ignoring gravitational drainage on reduction of surface runoff is significant in both forcings.

Figure 4.11 shows the comparison of soil moisture of each layer for considering and without considering gravitational flow by using SiBUC parameters (control and A2) and by MRI–SiB parameters (B0 and B2). The forcing data was NHRCM05 atmospheric output. The grid cell that showed significant soil moisture changed due to the impact of neglecting gravitational flow was selected in this plot. The simulation results in 1990 are selected because the annual rainfall in this year is the highest (more than 800 mm) among 10–years annual NHRCM05 rainfall.

In Figure 4.11(a), annual surface runoff increases by 1.5–fold, from 222 mm to 322 mm, while the annual subsurface runoff decreases from 162 mm to 20 mm. In contrast, in Figure 4.11(b), annual surface runoff decreases from 537 mm to 265 mm, while the annual subsurface runoff increases from 32 mm to 133 mm.

As seen in both figures, the changes of surface soil moisture due to the impacts of neglecting gravitational flow are seen mainly during the rainfall events. When the gravitational drainage was neglected, it resulted in the lower vertical exchanges between soil layers. Therefore, the soil moisture tends to be higher than that by considering the gravitational flow. In Figure 4.11(a), this results in the higher estimation of the surface runoff. As some rainwater has already been generated as surface runoff, the subsurface runoff is lower because of less infiltrated rainwater.

On the other hand, in Figure 4.11(b), the surface soil moisture has more fluctuation, and it also tends to reach saturation faster when the gravitational flow is considered. When the gravitational drainage is neglected, the surface runoff is lower, perhaps because the surface soil moisture does not reach saturation as fast as that by considering the gravitation flow.

4.5.5 Impacts of considering hydraulic diffusion for estimating subsurface runoff estimation

The impacts of considering hydraulic diffusion on subsurface runoff estimation would depend on soil moisture of root zone and recharge zone. Figure 4.12 shows the change of soil moisture and subsurface runoff when the hydraulic diffusion is considered when calculating the subsurface runoff. Subsurface runoff increases if the soil moisture of the root zone is higher than the recharge zone. Otherwise, it decreases.

The analysis of basin average, shown in Table 4.10, has been demonstrated that considering hydraulic diffusion for estimating the subsurface runoff results in the lower subsurface runoff compared to the original setting.

Table 4.10: Mean annual runoff components (unit: mm). Experiment 3 is considering hydraulic diffusion for subsurface estimation.

Forcing	MRI–AGCM 3.2S					NHRCM05				
Experiment	MRI–SiB	Control	A3	B0	B3	MRI–SiB	Control	A3	B0	B3
Qs	3	58	59	201	208	1	56	55	83	84
Qsb	143	136	109	86	44	46	11	7	28	20

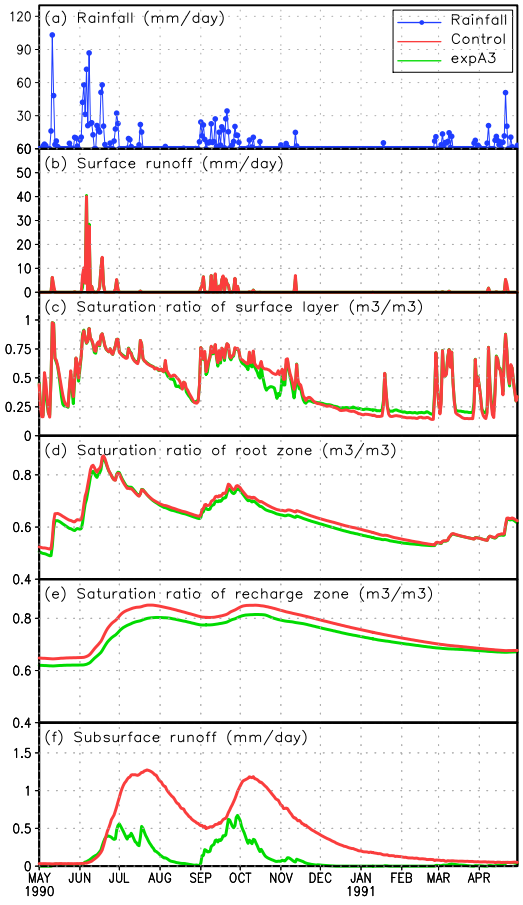

(a) Similar to Figure 4.10(a). A3 is simulation by considering hydraulic diffusion on subsurface calculation with SiBUC parameters.

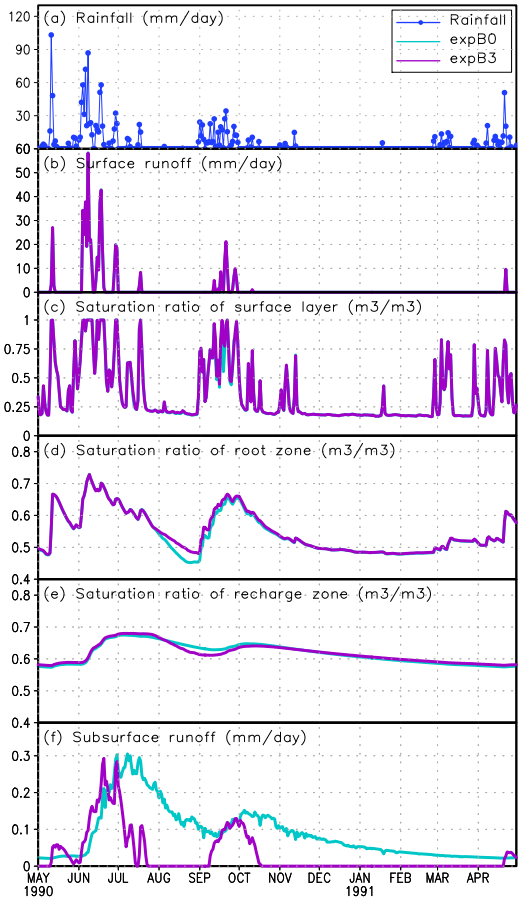

(b) Similar to Figure 4.10(b). B3 is for simulation by considering hydraulic diffusion on subsurface calculation with MRI–SiB parameters.

Figure 4.12: Similar to Figure 4.10 but for investigating the impacts of considering hydraulic diffusion for calculating subsurface runoff.

4.5.6 Impacts of changing all model structures

Adopting all structures of MRI–SiB (A4 and B4) has resulted in the decrease of surface runoff and increase of subsurface runoff compared to original structures of SiBUC (control and B0) as seen in Table 4.11. It is due to the impacts of each setting, as mentioned before. In experiment B4, the model structures and the soil parameters are set to be the same as MRI–SiB. However, the runoff characteristics of this experiment are different from the MRI–SiB results. Surface runoff by B4 is much higher than the subsurface runoff than MRI–SiB's runoff, which shows the dominant subsurface runoff.

The estimated soil moisture between experiment B4 and MRI–SiB is evaluated to figure out the reason. Simulated soil moisture by MRI–SiB is available in GCM and RCM output datasets. Figure 4.13 shows a comparison of time series of surface runoff, soil moisture of each layer, and subsurface runoff estimated by the two LSMs.

The year 1991 was selected for MRI–AGCM 3.2S and the year 1990 was for NHRCM05 because it had the highest rainfall amount (annual basin average is 1378 mm) among simulation period. Overall, the fluctuation of soil moisture between both LSMs is similar. However, the soil moisture of the surface soil layer is significantly different in near saturation conditions, such as in rainfall events between August and November. In the near saturation, soil moisture estimated by SiBUC tends to keep saturated, while MRI–SiB does not show such tendency. This difference in soil moisture has impacts on the generated surface and subsurface runoff.

Surface runoff by MRI–SiB was generated when soil moisture of both surface layer and root zone had saturated. It is due to the incorporation of P_2 structure. In experiment B4, P_2 structure was also adopted, but surface runoff was generated when soil moisture of surface layer reached saturation. As a result, the surface runoff estimated by the experiment B4 was more frequent than MRI–SiB.

Using both GCM and RCM forcing, annual surface runoff simulated by MRI–SiB is lower, and subsurface runoff is higher than experiment B4. These results show that the difference in soil moisture can have impacts on the generated surface and subsurface runoff.

Table 4.11: Mean annual runoff components (unit: mm). Experiment 4 is considering all MRI–SiB's structures.

Forcing	MRI–AGCM 3.2S					NHRCM05				
Experiment	MRI–SiB	Control	A4	B0	B4	MRI–SiB	Control	A4	B0	B4
Qs	3	58	37	201	126	1	56	24	83	50
Qsb	143	136	109	86	98	46	11	10	28	29

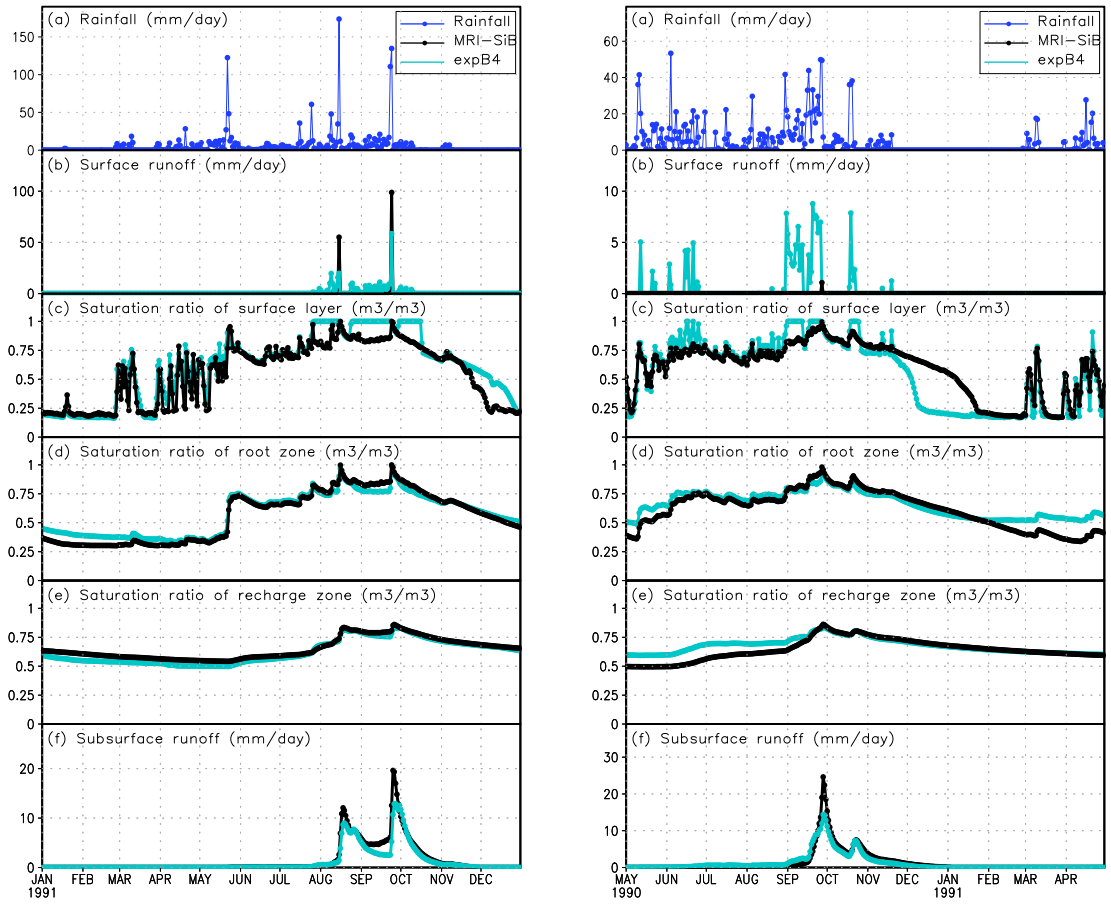

(a) Simulation results by using atmospheric output data from MRI–AGCM 3.2S in 1991.

(b) Simulation results by using atmospheric output data NHRCM05 in 1990.

Figure 4.13: Time series of daily rainfall (a), surface runoff (b), saturation ratio of each layer (c-e), and subsurface runoff (f). Black and light blue represent simulation by MRI–SiB and experiment B4, respectively.

Table 4.12: Mean annual runoff components (unit: mm). Experiment 5 is applying a semi–implicit method.

Forcing	MRI–AGCM 3.2S					NHRCM05				
Experiment	MRI–SiB	Control	A5	B0	B5	MRI–SiB	Control	A5	B0	B5
Qs	3	58	56	201	13	1	56	57	83	22
Qsb	143	136	137	86	257	46	11	11	28	73

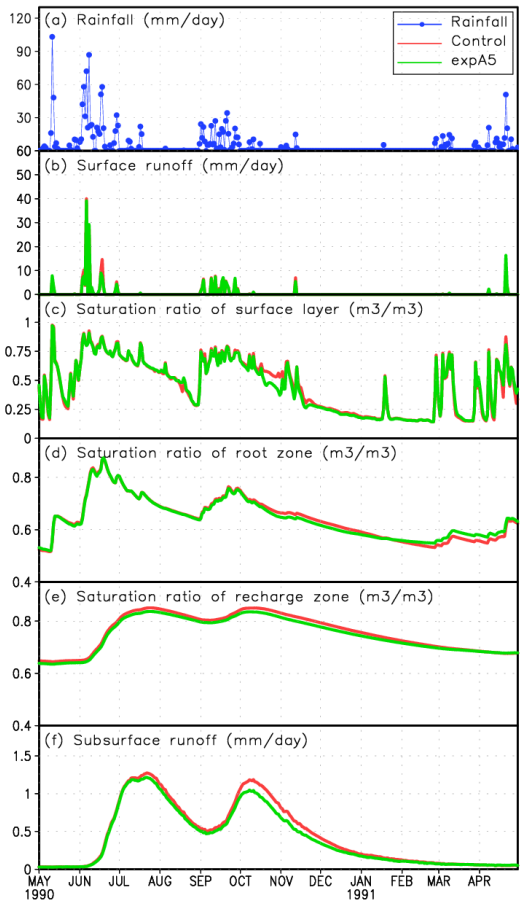

(a) Similar to Figure 4.10(a). A5 is simulation by applying semi–implicit method with SiBUC parameters.

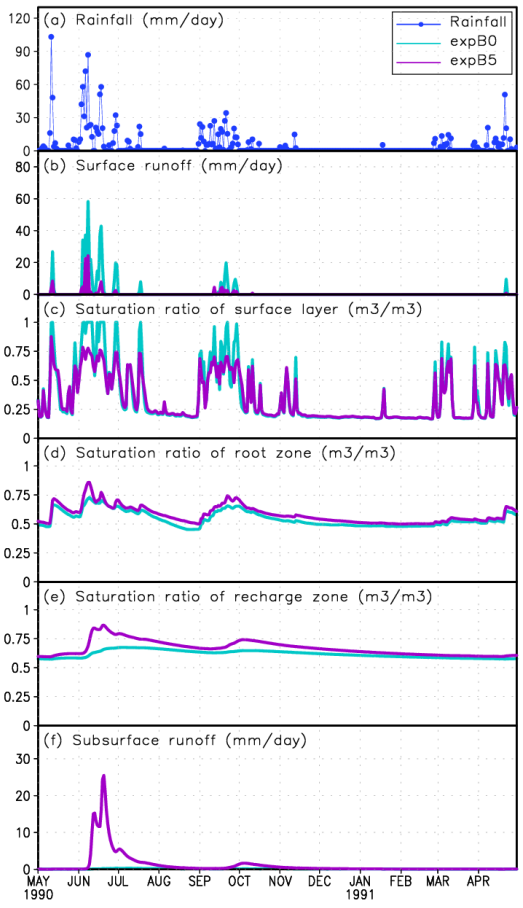

(b) Similar to Figure 4.10(b). B5 simulation by applying semi–implicit method (B5) with MRI–SiB parameters.

Figure 4.14: Similar to Figure 4.10 but for investigating the impacts of different time integration methods.

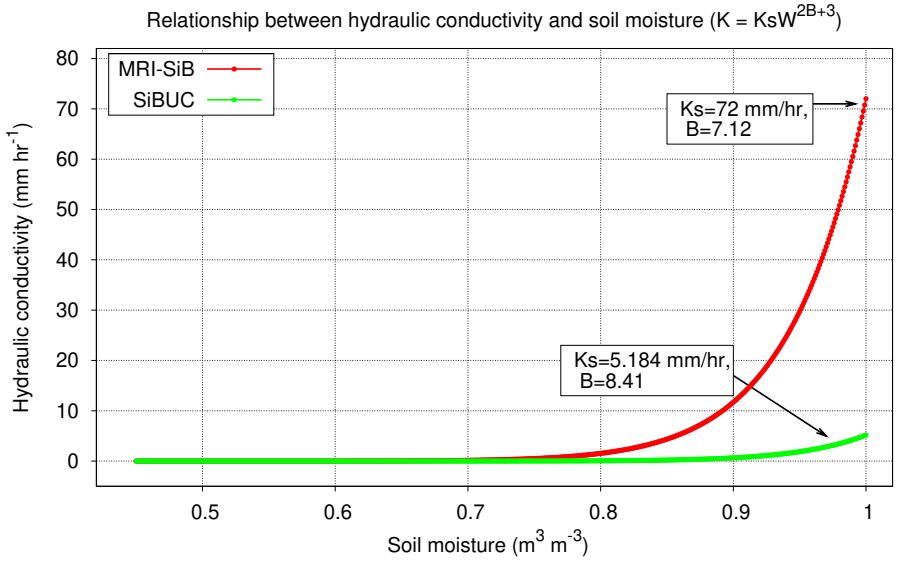

Figure 4.15: Relationship between hydraulic conductivity (y–axis) and soil moisture (x–axis) based on Clapp and Hornberger (1978). Red and green lines are estimated by using soil parameters of MRI–SiB (broadleaf–evergreen forest type) and SiBUC (clay loam), respectively.

4.5.7 Impacts of different time integration methods for soil schemes

Previous results have shown the difference in soil moisture estimation between SiBUC and MRI–SiB. That might be caused by different time integration methods for updating soil moisture in both LSMs: an explicit–midpoint method in SiBUC and a semi–implicit method in MRI–SiB. Table 4.12 shows the impacts of different time integration methods on runoff estimation by using different soil parameters. When SiBUC soil parameters were used (control and A5), even if the numerical scheme was changed, the runoff components did not show a significant difference. However, the runoff characteristics showed a remarkable change when the different time integration was applied by using MRI–SiB soil parameters (B0 and B5).

Figure 4.14 shows a comparison of soil moisture estimated by the explicit and implicit method by using SiBUC and MRI–SiB parameters. In general, both methods do not significantly differ in soil moisture estimation. However, soil moisture estimated by different schemes shows a clear difference when MRI–SiB parameters were utilized during rainfall events. The difference in the soil moisture estimation between the two methods is mainly affected by the saturated hydraulic conductivity (K_s) setting between the two LSMs.

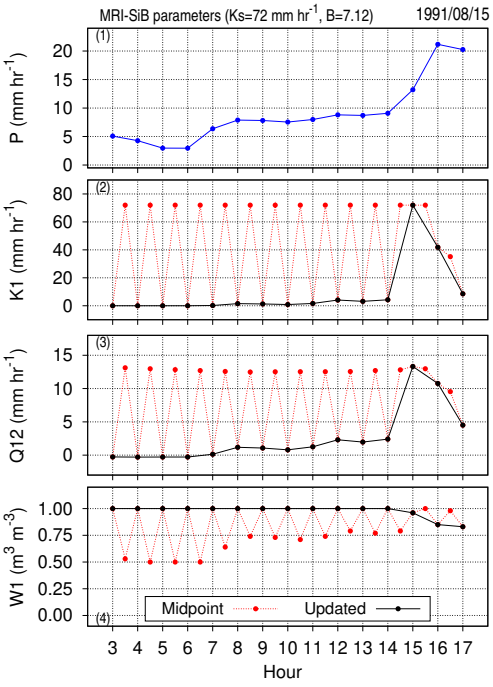

(a) Midpoint–explicit by MRI–SiB parameters.

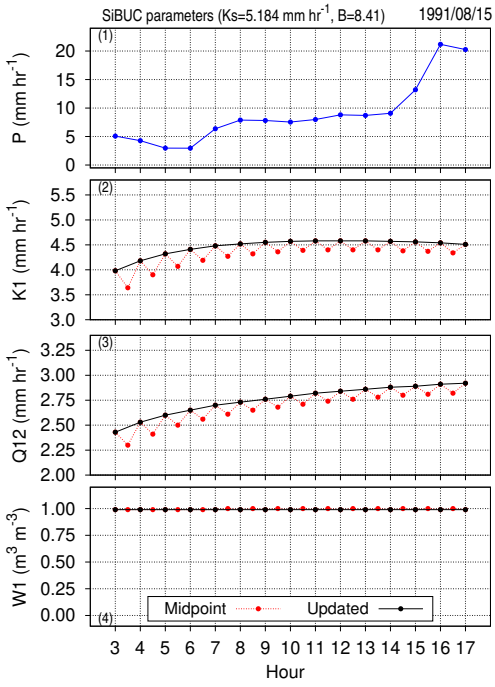

(b) Midpoint–explicit by SiBUC parameters.

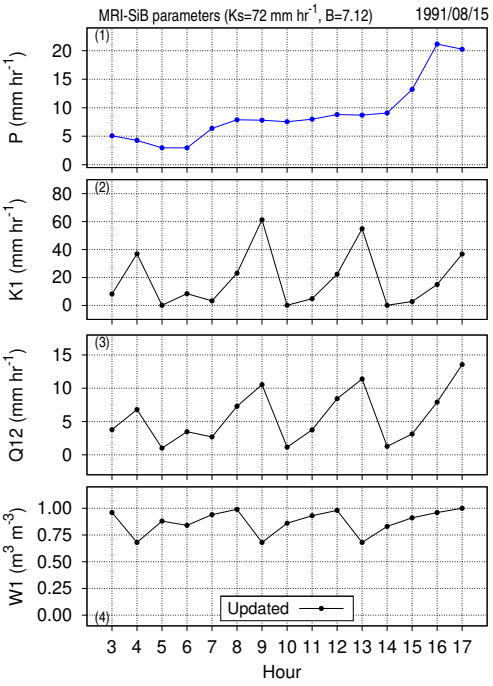

(c) Semi–implicit by MRI–SiB parameters.

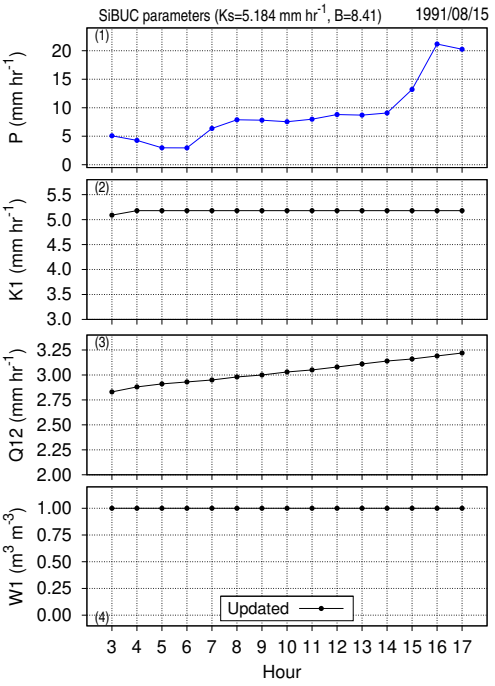

(d) Semi–implicit by SiBUC parameters.

Figure 4.16: Impacts of different time integration methods by different parameters on soil moisture estimation. (1) P (mm hr^{-1}), (2) K_1 (mm hr^{-1}), (3) $Q_{1,2}$ (mm hr^{-1}), (4) W_1 (m^3 m^{-3}). Red and black dots represent midpoint and updated variables for each time step.

The relationship between hydraulic conductivity and soil moisture (based on Clapp and Hornberger, 1978) estimated by SiBUC and MRI–SiB parameters is shown in Figure 4.15. This plot used the parameters of clay loam soil in SiBUC and broadleaf–evergreen forest in MRI–SiB. As seen from this figure, hydraulic conductivity estimation between the two parameters is similar during the unsaturated condition. However, it shows a clear difference as the soil moisture reaches saturation. This difference in the behavior of hydraulic conductivity significantly affects the calculation of soil–water transfer between the adjacent soil layers $Q_{i,i+1}$ as well as the soil moisture updates, particularly during heavy rainfall as the soil moisture tends to reach saturated condition.

Figure 4.16 shows a time series of hourly precipitation P, hydraulic conductivity of surface soil layer K_1, soil–water transfer between top and second soil layer ($Q_{1,2}$, and soil moisture of surface soil layer W_1, between different time integration methods and soil parameters. In this figure, the output of MRI–AGCM 3.2S was utilized as forcing. And similarly, the parameters of clay loam soil in SiBUC and broadleaf–evergreen forest in MRI–SiB were used in this plot. The results of several hours during August 15, 1991, are plotted here, as quite intense rainfall events could be captured during this period. The W_1 is plotted in this figure, because it significantly affects the runoff characteristics: if the W_1 tends to be saturated, the surface runoff will be high, and the subsurface runoff will be low, and vice versa. The updated W_1 in each time step depends on initial soil moisture (estimated from the previous time step), precipitation P (as input), and water transfer within the soil ($Q_{i,i+1}$), as drainage or output). The actual mechanisms of soil moisture update in the model are more complex, such as, at first the rainfall should be intercepted by canopy before it reaches to the ground, and the amount of water reaches on the ground should be first reduced by surface runoff (depending on W_1) before it is infiltrated in the soil. However, for simplicity, only the relation between P and $Q_{i,i+1}$ is used for describing the difference in soil moisture update for each time step among different numerical schemes and soil parameters.

As mentioned earlier, the hydraulic conductivity is estimated based on soil moisture: the higher the soil moisture, the higher the hydraulic conductivity. The hydraulic conductivity is also directly proportional to the soil–water transfer $Q_{i,i+1}$. Here, the ratio between precipitation and soil–water transfer will affect the soil moisture update. If the precipitation is higher than the drainage $Q_{i,i+1}$, the estimated soil moisture in the next time will become higher than the initial soil moisture. Oppositely, if the drainage $Q_{i,i+1}$ is higher than the input precipitation, the updated

soil moisture will be lower than the initial soil moisture, as more rainwater could be infiltrated into a deeper soil layer. That is the basic concept to understand the results of Figure 4.16.

For the midpoint–explicit method, there are two calculation steps for updating the soil moisture in each time step. Using initial soil moisture value, midpoint soil moisture is first calculated, then the midpoint value is used to update the soil moisture for the next step. On the other hand, in the semi–implicit method, the initial soil moisture value is used to update the soil moisture in the next step.

First, let's focus on the results by using the explicit–midpoint method by MRI–SiB parameters, shown in Figure 4.16(a). Let's assume that the estimated W_1 at time t = 3 (in hour) as initial condition for the next time step t = 4. The W_1 at t = 3 is first used to calculate hydraulic conductivity K_1 and $Q_{1,2}$ at midpoint (shown in the red dots). As $W_{1,t=3}$ is equal to 1 (saturated condition), the estimated K_1 becomes equal to K_{s} (hydraulic conductivity at saturation), and thus the $Q_{i,i+1}$ is also high (note that $Q_{i,i+1}$ also depends on soil moisture of second soil layer). As the rainfall P at t = 4 is lower than $Q_{1,2}$ at midpoint ($P_{t=4} < Q_{1,2,t=3,\mathrm{midpoint}}$), the change of soil moisture of top layer becomes negative due to more drainage into a deeper soil layer, resulting in the midpoint soil moisture of top layer becomes lower than the initial value ($W_{1,t=3,\mathrm{midpoint}}$ = 0.5 $<$ $W_{1,t=3}$ = 1.0). The midpoint soil moisture ($W_{1,t=3,\mathrm{midpoint}}$) is then used for calculating K_1 and $Q_{1,2}$ at next time step (in this case, t = 4, shown in the black dots). Since the $W_{1,t=3,\mathrm{midpoint}}$ is low (=0.5, unsaturated condition), the estimated $K_{1,t=4}$ and $Q_{1,2,t=4}$ are also low (both values are close to 0). Now, the P at t = 4 is higher than the drainage $Q_{1,2,t=4}$, resulting in the increase of soil moisture compare to the midpoint value ($W_{1,t=3,\mathrm{midpoint}}$ = 0.5 $< W_{1,t=4}$ = 1.0). As mentioned before, the hydraulic conductivity using MRI–SiB parameters significantly differs when the soil moisture changes from unsaturated to saturated condition. It resulted in soil moisture oscillation calculated at the midpoint and next step (red and black dots). For calculating the surface runoff, only the updated soil moisture value (black dot) is considered. The updated soil moisture using the explicit–midpoint method (two–step calculations) with MRI–SiB parameters tend to be saturated, therefore, the generated surface runoff is also high.

In the case of explicit–midpoint method with SiBUC parameters (Figure 4.16(b)), oscillation of hydraulic conductivity and soil–water flow were also captured at the midpoint and in the next time step. In the SiBUC parameters, the change of hydraulic conductivity from unsaturated to saturated condition is less significant than the MRI–SiB soil parameters. Therefore, the difference in K_1 and $Q_{1,2}$ estimation between the midpoint and updated value is very small

compared to that of MRI–SiB parameters. As the hydraulic conductivity at saturation in SiBUC is set relatively small (about 5 mm hr^{-1}), the infiltration rate also tends to be low. Therefore, the updated soil moisture tends to be saturated, resulting in high surface runoff generation.

When the semi–implicit method was applied by using MRI–SiB parameters (Figure 4.16(c)), the updated soil moisture tends to be less saturated than by the midpoint–explicit method. As mentioned earlier, in contrast to the midpoint–explicit method that implements two–step calculations, the semi–implicit method updates the soil moisture directly by using the initial soil moisture estimated from the previous time step. Therefore, the oscillation of soil moisture can be seen clearly, due to the behavior of hydraulic conductivity when the soil moisture change from unsaturated to saturated condition. Due to the high value of saturated hydraulic conductivity (about 72 mm hr^{-1}), the infiltration rate also tends to be high, causing less saturated soil moisture and less surface runoff generation.

In the case of semi–implicit method was applied with SiBUC parameters (Figure 4.16(d)), the updated soil moisture also tends to be saturated, similar to the result by the explicit–midpoint method. Slightly different estimations of K_1 and $Q_{1,2}$ were found compared to the explicit method. However, it does not significantly affect the soil moisture and surface runoff generation due to small infiltration rates affected by the hydraulic conductivity setting.

In summary, time integration methods impact soil moisture estimation and runoff generation, depending on which soil parameters are used, particularly during intense rainfall events. Applying the explicit–midpoint method for updating the soil moisture seems to have uncertainty, particularly when the change of hydraulic conductivity is significant during unsaturated to saturated conditions (such as in MRI–SiB parameters setting). Therefore, selecting which time integration method for updating the soil moisture is essential as the soil moisture estimation significantly affects the runoff generation.

4.5.8 Impacts of considering all MRI–SiB settings in SiBUC

By considering all MRI–SiB settings in SiBUC, total runoff by these experiments (A6 and B6) are lower, and the evapotranspiration are higher than the original SiBUC structures (control and B0), as seen in Table 4.13. Surface runoff decreases significantly than the original results. In particular, the surface runoff estimated by MRI–SiB parameters shows a higher reduction compared to that by SiBUC parameters. In MRI–SiB, soil characteristics parameters are set to be higher, and soil depth is thinner than that in SiBUC. It caused higher infiltration rates and higher reduction of surface runoff in the MRI–SiB.

Figure 4.17 shows a comparison of soil moisture estimated by the adopting all MRI–SiB settings using SiBUC and MRI–SiB parameters.

Figure 4.18 shows time series of runoff components and soil moisture of each layer by MRI–SiB and the experiment B6. The grid cell within the basin, which showed significant impacts of changing time integration methods on surface runoff and soil moisture of the topsoil layer, was selected in this plot. As seen, the timing of surface runoff by the B6 is similar to MRI–SiB.

In this cell, annual surface runoff forced by GCM output by MRI–SiB and B6 is 160 and 176 mm, respectively. Not only the timing but also the amount of surface runoff by B6 is close to MRI-SiB.

Both results show the surface runoff was generated when soil moisture of the first and second layers reached saturation. It is reasonable due to the incorporation of P_2 structure.

Annual subsurface runoff by MRI–SiB and B6 is 504 and 554 mm, respectively. This result shows the soil moisture, and the amount of runoff components by experiment B6 is close to the MRI–SiB. Overall, it shows that adopting MRI–SiB's soil parameters, model structures, and time integration methods in SiBUC can produce similar runoff characteristics and soil moisture to MRI–SiB. The setting of experiment B6 is set as MRI–SiB emulation model.

Table 4.13: Mean annual runoff components (unit: mm). Experiment 6 is employing all MRI–SiB's settings.

Forcing	MRI–AGCM 3.2S					NHRCM05				
Experiment	MRI–SiB	Control	A6	B0	B6	MRI–SiB	Control	A6	B0	B6
Qs	3	58	38	201	5	1	56	23	83	10
Qsb	143	136	109	86	205	46	11	10	28	57

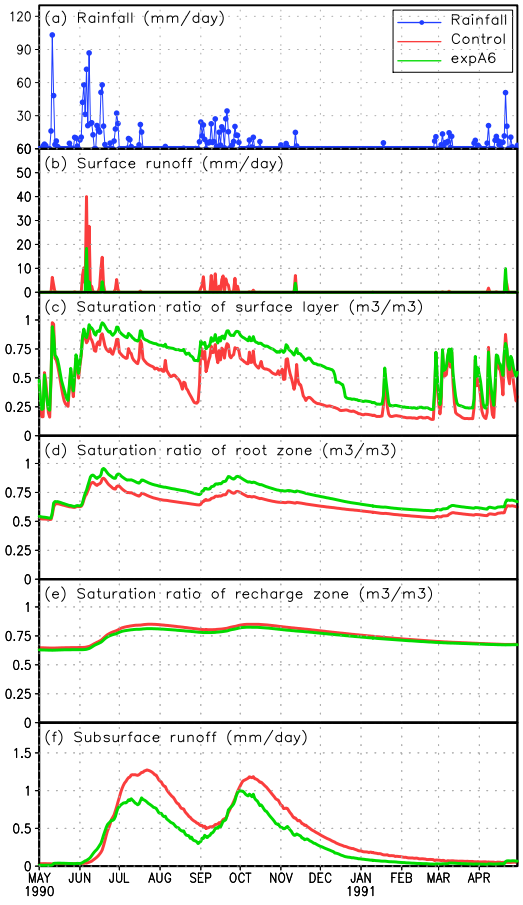

(a) Similar to Figure 4.10(a). A6 is simulation by applying all MRI–SiB settings with SiBUC parameters.

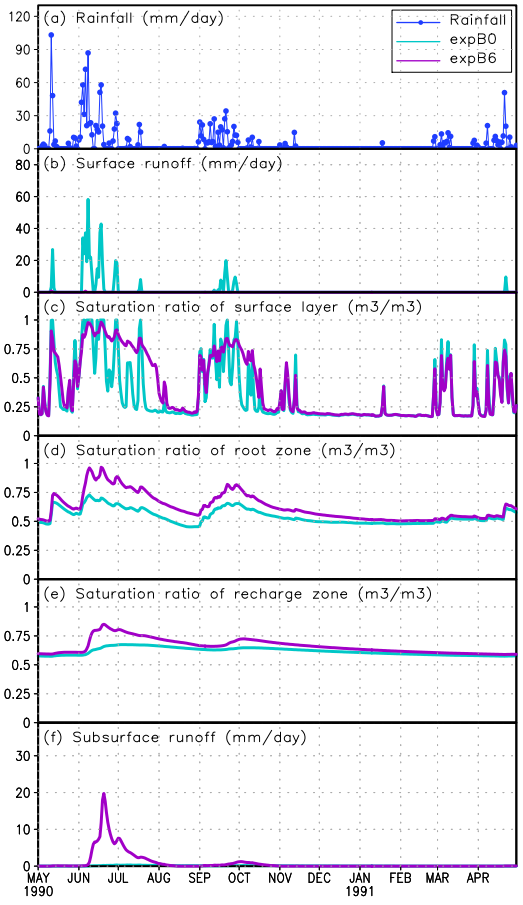

(b) Similar to Figure 4.10(b). B6 is simulation by applying all MRI–SiB settings with MRI–SiB parameters.

Figure 4.17: Similar to Figure 4.10 but for investigating the impacts of considering all MRI–SiB settings in SiBUC.

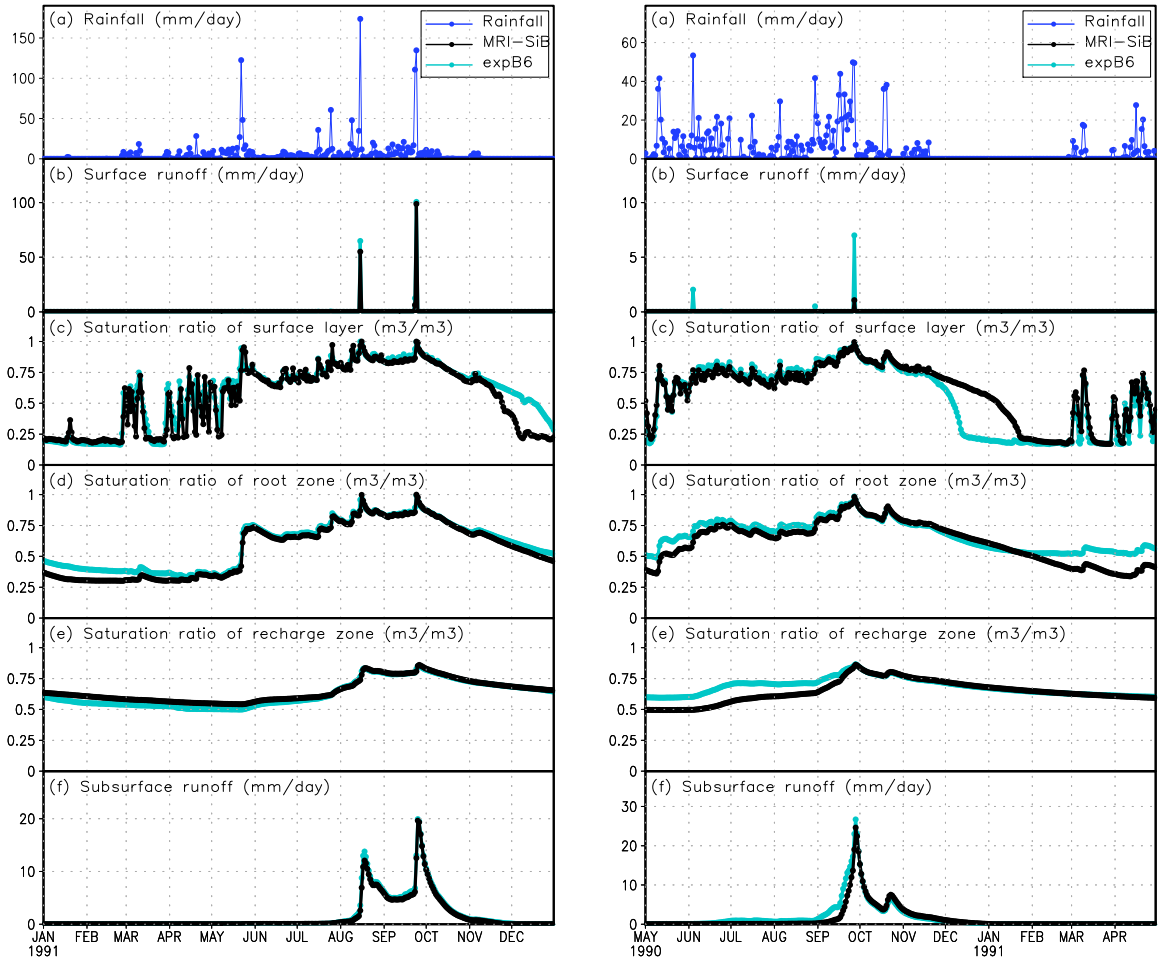

(a) Simulation forced by atmospheric data from MRI–AGCM 3.2S in 1991.

(b) Simulation forced by atmospheric data from NHRCM05 in 1990.

Figure 4.18: Time series of daily rainfall (a), surface runoff (b), saturation ratio of each layer (c-e), and subsurface runoff (f). Black and light blue represent simulation by MRI–SiB and experiment B6, respectively.

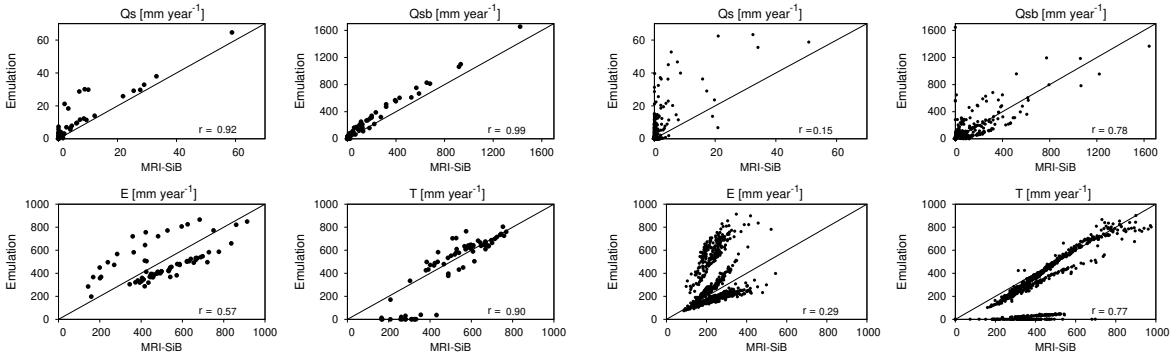

(a) 20–years–mean annual simulations forced by MRI–AGCM 3.2S atmospheric data.

(b) 10–years–mean annual simulations forced by NHRCM05 atmospheric data.

Figure 4.19: Scatter plot of mean annual water budget components (surface runoff (Qs), subsurface runoff (Qsb), evaporation (E), and transpiration (T)) by MRI–SiB and emulation model. Only grid cells within the target basin are plotted. r value is correlation coefficient.

4.6 Evaluation of MRI–SiB emulation model

4.6.1 Overall impacts

As mentioned earlier, MRI–SiB emulation model was developed by adopting MRI–SiB soil parameters, model structures, and time integration methods in SiBUC (experiment B6 setting). Mean annual water budget components was shown in the previous section in Figure 4.8 and Figure 4.9. Overall, the emulation model could reproduce similar runoff characteristics to MRI–SiB: low surface runoff and high subsurface runoff. However, the subsurface runoff estimated by the emulation model is much higher than MRI–SiB. This section investigates in detail why such differences happen.

4.6.2 Spatial distributions of water budget components

Figure 4.19 shows scatter plot of mean annual water budget components by emulation model and MRI–SiB, forced by MRI–AGCM 3.2S and NHRCM05. Figure 4.20 shows a difference of spatial pattern of mean annual water budget between emulation model and MRI–SiB. In general, the simulated water budget by the emulation model shows a good correlation with the results by MRI–SiB. However, surface and subsurface runoff by the emulation model is mostly

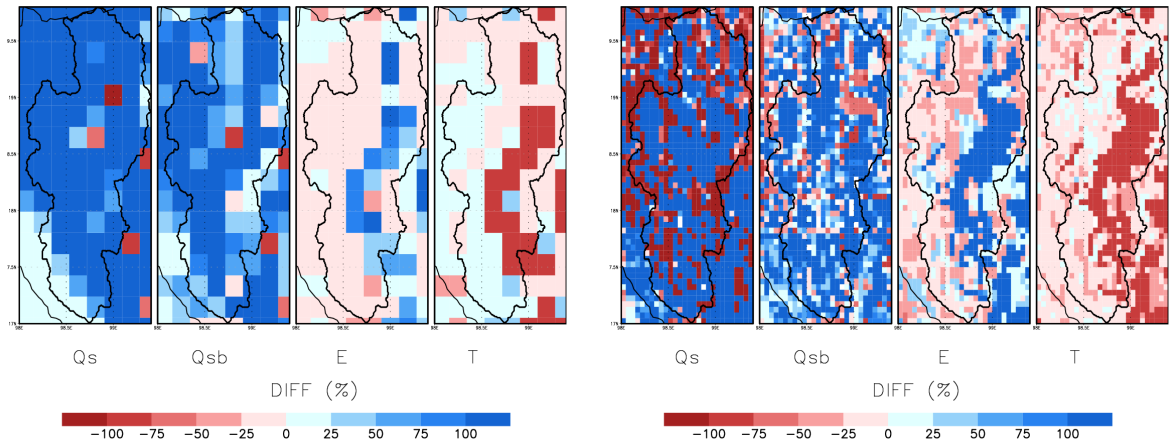

(a) Simulations by GCM forcing.

(b) Simulations by RCM forcing.

Figure 4.20: Difference in mean annual water budget components (surface runoff (Qs), sub-surface runoff (Qsb), evaporation (E), and transpiration (T)) by emulation model and MRI–SiB. Red and blue color represent lower and higher estimation by the emulation model compared to the MRI–SiB.

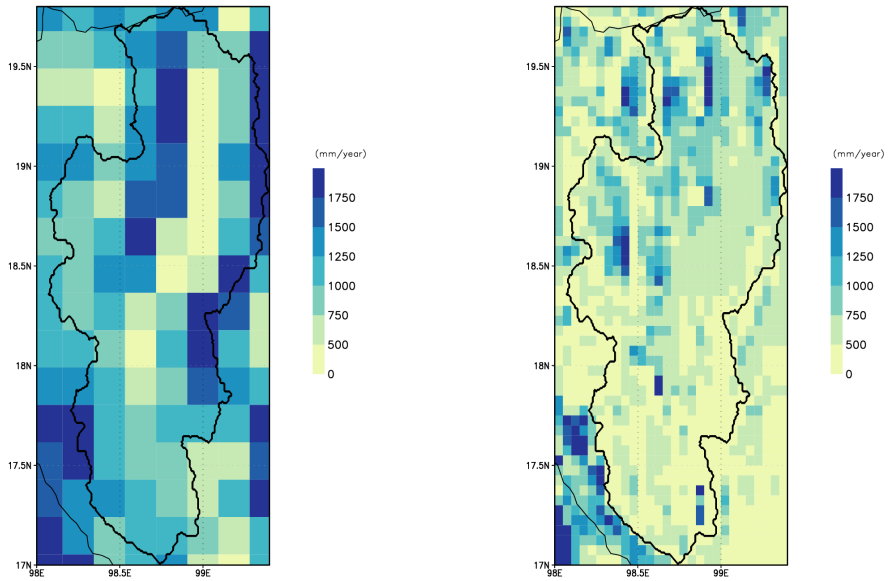

(a) 20–years–mean annual rainfall by MRI–AGCM 3.2S.

(b) 10–years–mean annual rainfall by NHRCM05.

Figure 4.21: Spatial pattern of climatological mean rainfall by climate models.

higher than MRI–SiB. The overestimation of surface runoff by the emulation model happens in most regions. However, the overprediction of subsurface runoff forced by the GCM seems to correlate with the rainfall. Figure 4.21(a) shows spatial distributions of climatological mean annual rainfall by the GCM. This comparison indicates that the grid cells that show very high overestimation of subsurface runoff correspond to those with low rainfall amounts. It is because the MRI–SiB estimated very low subsurface runoff in this region, thus the difference was quite high. The spatial pattern of the difference in surface and subsurface runoff by RCM forcing does not show a clear correlation with rainfall amount, as shown in Figure 4.21(b).

Evaporation and transpiration estimated by the emulation model do not show a high difference with MRI–SiB's results in most regions. However, the grid cells which show the high positive difference in evaporation show a high negative deviation in transpiration. It is due to vegetation parameter settings, such as greenness fraction, leaf area index, and a fraction of photosynthetically active radiation. As mentioned earlier, in MRI–SiB, the vegetation parameters are set for two vegetation layers: canopy and ground cover. In SiBUC, the vegetation scheme only consists of one layer: both canopy and ground cover are treated together as a canopy. The grid cells, which do not consider vegetation parameters for green cover in the emulation model, show much higher evaporation and lower transpiration than MRI–SiB. As seen, the grid cells which show a dominant canopy layer can well reproduce MRI–SiB's transpiration, and shows a high correlation in both simulations.

Evaporation estimated by the emulation model and MRI–SiB forced by GCM does not show a clear trend. However, the pattern can be seen obviously in the results by using RCM forcing. Three trends can be observed in the figure: very high estimation, high estimation, and low estimation of evaporation by the emulation model compared to MRI–SiB. These trends corresponds to vegetation types. As mentioned earlier, much higher evaporation estimated by the emulation model correspond to short–vegetation and cropland, which is dominated by ground cover than the canopy. In this simulation, only the parameters of the canopy layer are considered in the emulation model due to the simplified treatment of the ground cover layer in SiBUC. The grid cells which show higher evaporation estimated by the emulation model corresponds to broadleaf–needleleaf forest. And the cell which has lower evaporation simulated by the emulation model corresponds to broadleaf–evergreen forest. These differences might be due to different treatment of evaporation schemes in the two LSMs. However, further investigation is necessary to understand the reasons.

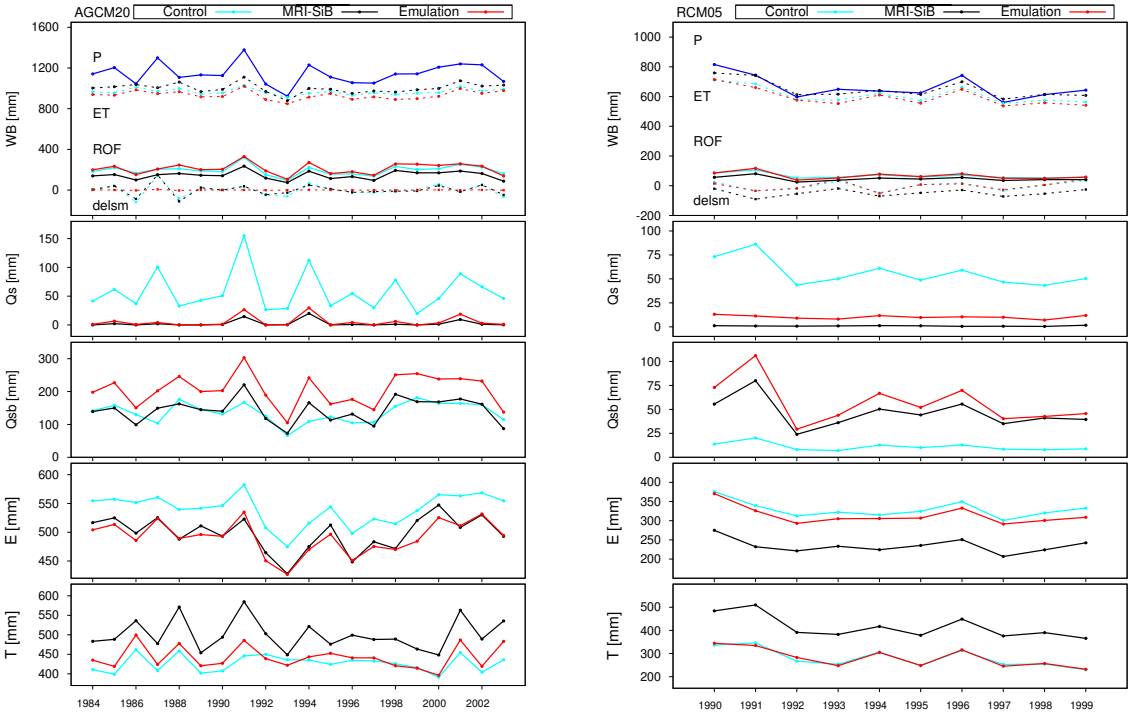

(a) Simulations by GCM forcing.

(b) Simulations by RCM forcing.

Figure 4.22: Time series of annual water budget components (precipitation (P), evapotranspiration (ET), runoff (ROF), change of soil moisture (delsm), surface runoff (Qs), subsurface runoff (Qsb), evaporation (E), and transpiration (T)). Light blue, black, and red lines represent simulation by original SiBUC (control), MRI–SiB, and emulation model, respectively.

4.6.3 Annual water budget

Figure 4.22(a) and Figure 4.22(b) show time series of annual water budget components forced by MRI–AGCM 3.2S (for 20 years) and NHRCM05 (for 10 years), respectively. In general, the emulation model estimates a lower evapotranspiration, and a higher runoff than MRI–SiB. Although the surface runoff and subsurface runoff by the emulation model are larger than MRI–SiB, the characterisitcs of runoff is very close to the MRI–SiB, compare to the results by the original SiBUC (control). The emulation model also could capture the increase or decrease of annual runoff similar to the MRI–SiB. The emulation model underpredicts the MRI-SiB's transpiration in both simulations. In contrast, evaporation by the emulation model is almost close to MRI–SiB in the simulation using GCM forcing, while it is higher when RCM forcing is used.

Table 4.14: Evaluation of daily discharge simulated by emulation model with respect to MRI–SiB for the whole simulation period.

Forcing	NSE	RMSE (m^3 s^{-1})	ERROR (%)	r
MRI–AGCM 3.2S (20 years)	0.83	89	47	0.99
NHRCM05 (10 years)	0.68	44	44	0.97

4.6.4 River discharge simulation

Figure 4.23 and Figure 4.24 shows daily discharge simulated by MRI–SiB and emulation model, forced by MRI–AGCM 3.2S and NHRCM05, respectively. Evaluation of daily discharge simulated by the emulation with respect to MRI–SiB is shown in Table 4.14. Performance of the emulation model to reproduce the discharge by MRI–SiB is evaluated by calculating Nash Sutcliffe Efficiency (NSE; Nash and Sutcliffe, 1970), Root Mean Square Error (RMSE), difference in the volume of discharge by the emulation model, and flow by MRI–SiB (ERROR in percentage), and Pearson correlation coefficient (r), as shown in Eq. (4.21), Eq. (4.22), Eq. (4.24), respectively.

$$NSE = 1 - \frac{\sum_{i=1}^{N} \left(M_{\mathrm{i}} - O_{\mathrm{i}}\right)^2}{\sum_{i=1}^{N} \left(O_{\mathrm{i}} - \overline{O}\right)^2} \tag{4.21}$$

$$RMSE = \sqrt{\frac{\sum_{i=1}^{N} \left(M_{\mathrm{i}} - O_{\mathrm{i}}\right)^2}{N}} \tag{4.22}$$

$$ERROR = \frac{\sum_{i=1}^{N} \left(M_{\mathrm{i}} - O_{\mathrm{i}}\right)}{\sum_{i=1}^{N} O_{\mathrm{i}}} \times 100 \tag{4.23}$$

$$r = \frac{\sum_{i=1}^{N} \left(M_{\mathrm{i}} - \overline{M}\right)\left(O_{\mathrm{i}} - \overline{O}\right)}{\sqrt{\sum_{i=1}^{N} \left(M_{\mathrm{i}} - \overline{M}\right)^2 \left(O_{\mathrm{i}} - \overline{O}\right)^2}} \tag{4.24}$$

with, r is correlation coefficient, M_{i} and O_{i} are discharge by the emulation model and MRI–SiB, respectively, and $\overline{M}$ and $\overline{O}$ are mean of simulated discharge by the emulation model and MRI–SiB, respectively.

As seen, the discharge by emulation model shows a very high correlation with the discharge by MRI–SiB (all r-value is higher than 0.95). This means the emulation model can well reproduce an increase or decrease of hydrograph similar to MRI–SiB, such as shown in Figure 4.25.

NSE index by emulation model also shows a high score, which is more than 0.5, indicating good model performance. By using GCM forcing, the performance of the emulation model is better than that of using RCM forcing. Nevertheless, the discharge by the emulation model shows higher volume than the MRI–SiB due to a higher estimation of runoff.

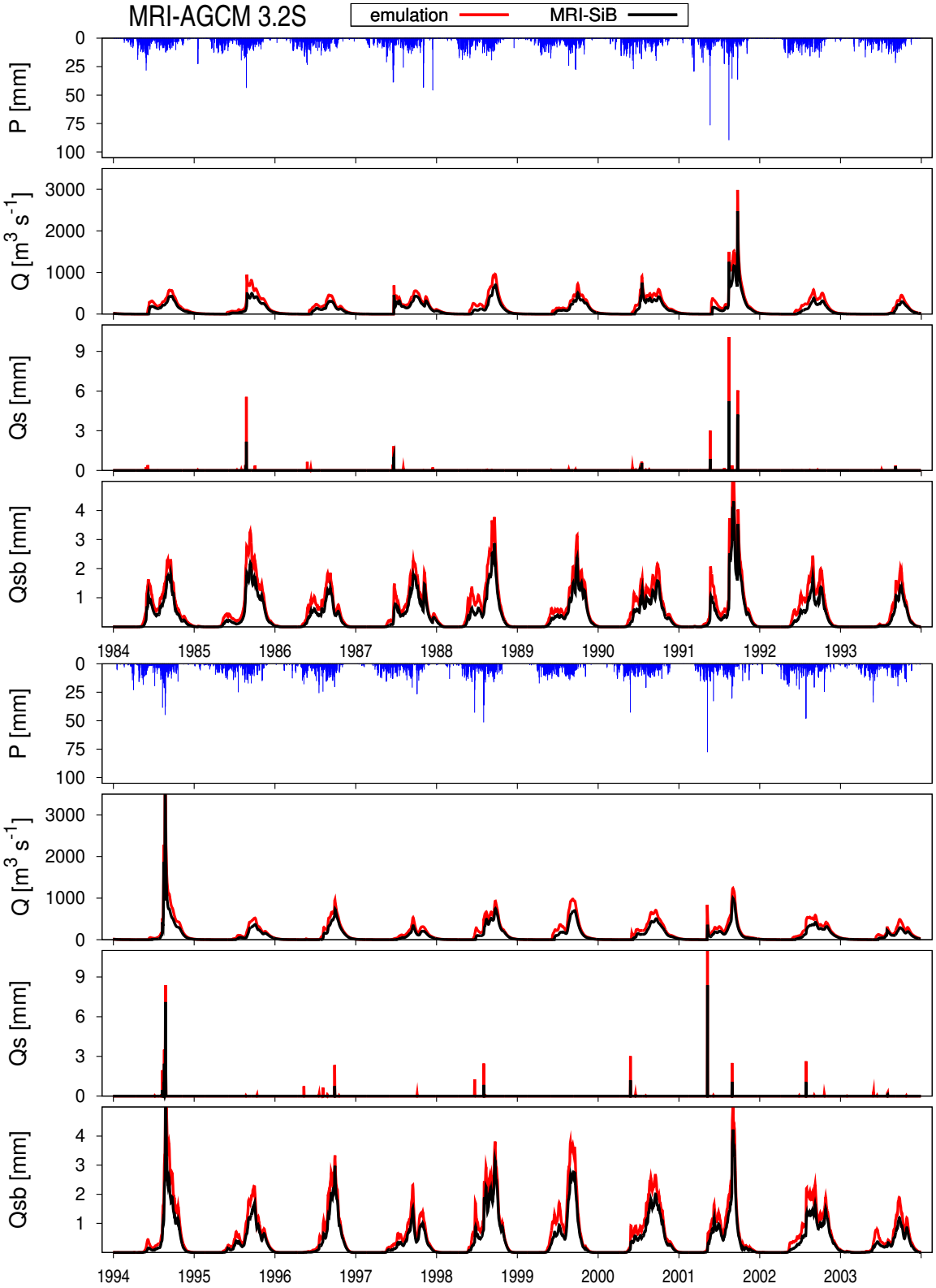

Figure 4.23: Daily discharge for 20 years forced by MRI–AGCM 3.2S. Black and red lines represent simulation results by MRI–SiB and emulation model, respectively. P, Q, Qs, and Qsb represent basin average of GCM precipitation, discharge, surface runoff, and subsurface runoff, respectively.

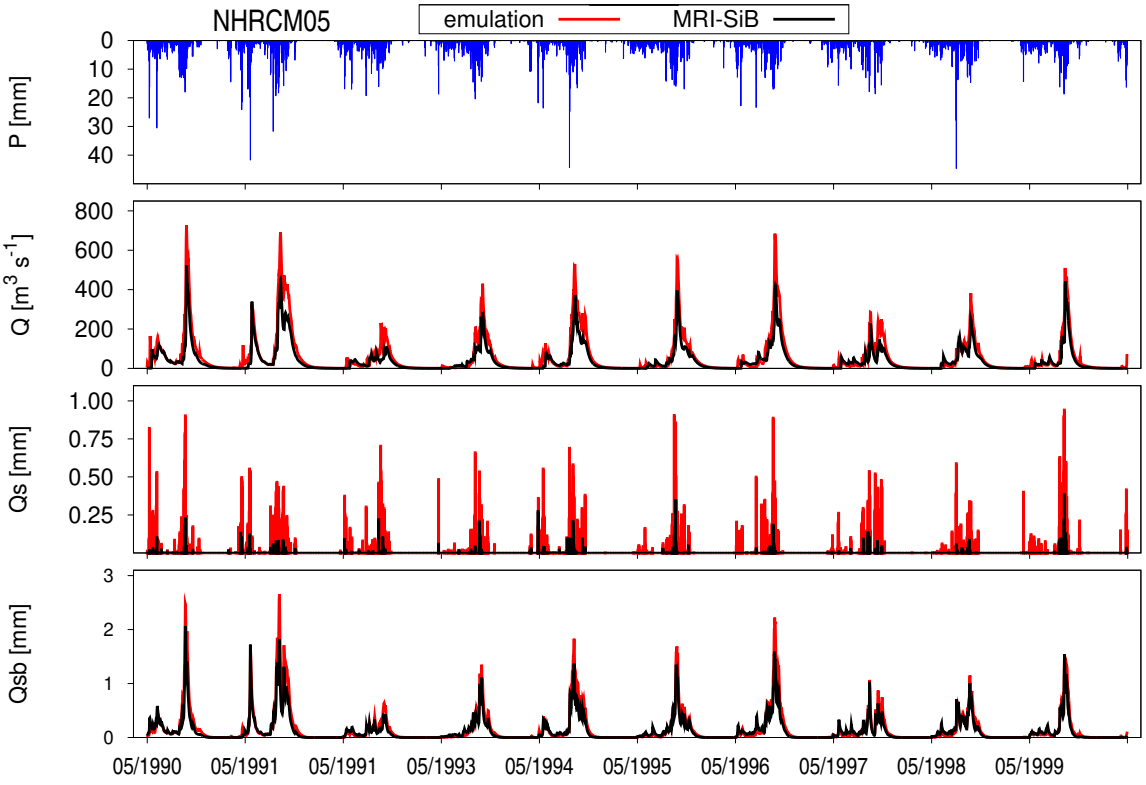

Figure 4.24: Similar to Figure 4.23 but for 10 years daily discharge forced by NHRCM05.

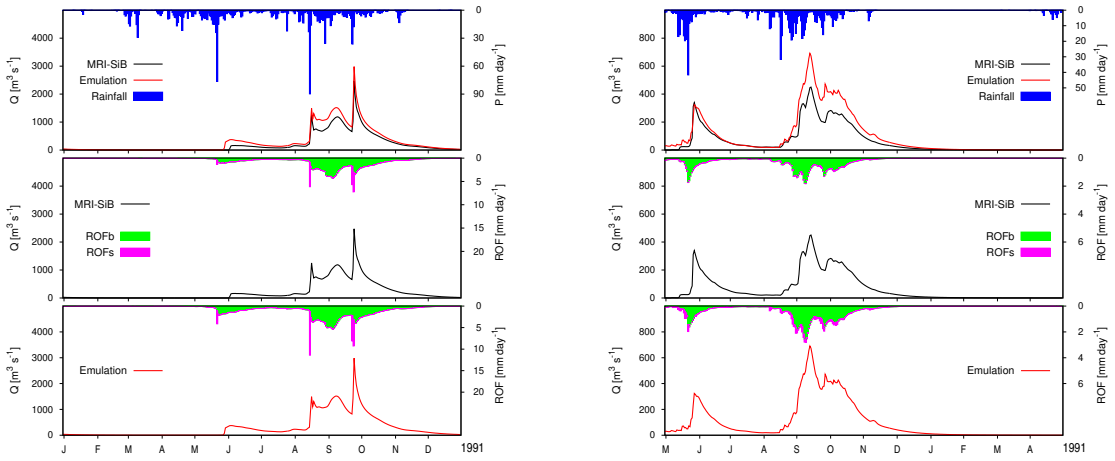

(a) Simulation by GCM forcing in 1991.

(b) Simulation by RCM forcing in 1991.

Figure 4.25: Daily discharge simulated by MRI–SiB and emulation model, represented by black and red lines, respectively. Blue bar shows basin average daily rainfall from MRI–AGCM 3.2S. Pink and green bar are surface and subsurface runoff, respectively.

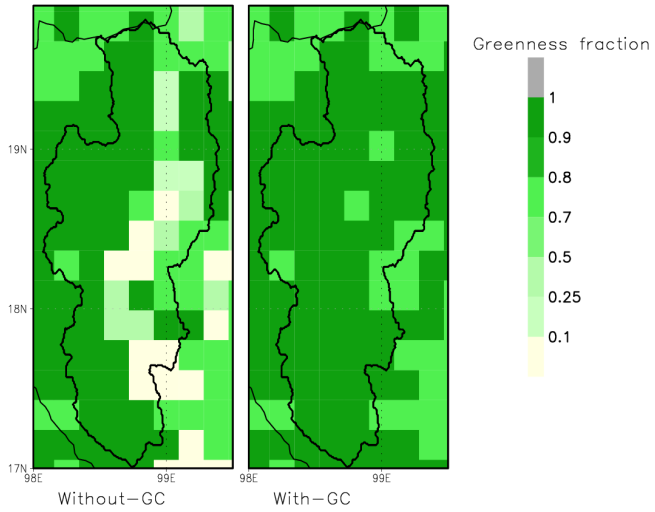

Figure 4.26: Comparison of greenness fraction without (left) and wit (right) considering ground cover parameters.

Table 4.15: 20–years–mean water budget components. Forcing is GCM output.

Mean annual (mm year^{-1})	ET	ROF	Qs	Qsb	E	T	delsm
MRI–SiB	999	146	3	143	498	501	1
Without ground cover (experiment B6)	934	210	5	205	491	442	0
With ground cover	890	254	6	248	370	520	0

4.7 Discussion

4.7.1 Parameters related to ground cover layer

As seen in the previous results, the grid cells in the emulation model, which did not consider parameters related to ground cover, showed lower transpiration than MRI–SiB. We also did an experiment to investigate the impacts of considering the parameters for the ground cover layer. Since SiBUC only has one vegetation layer, we selected only the maximum value between canopy and ground cover layers. For example, in cropland type, the greenness fraction parameter for a canopy is 0.075 and for ground cover is 1.0. The value of 0.075 was used in the emulation model, and in the current experiment, 1.0 is used. Comparison of greenness fraction by without and with considering ground cover parameters is shown in Figure 4.26. This method is also applied for other parameters related to vegetation, such as Leaf Area Index and

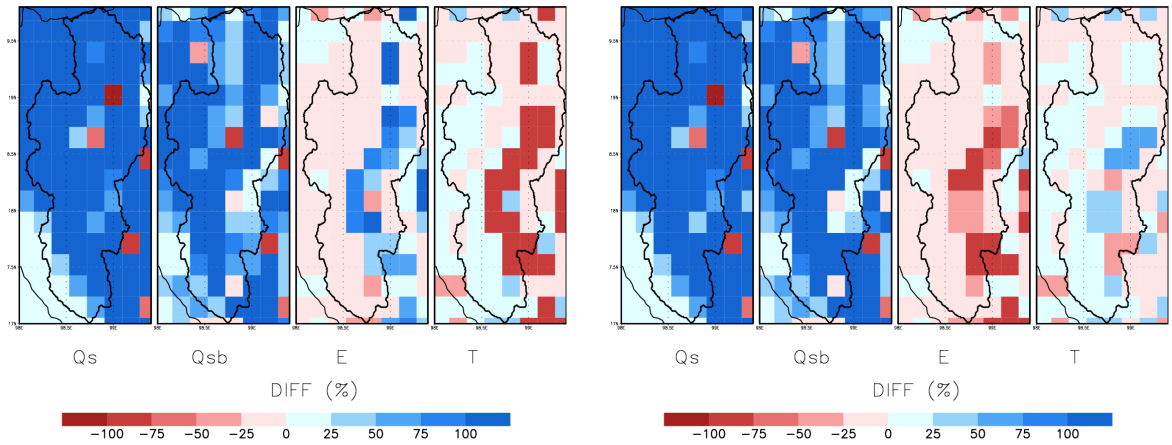

(a) Difference without ground cover parameters (B6).

(b) Difference by using ground cover parameters.

Figure 4.27: Difference in mean annual water budget components (surface runoff (Qs), subsurface runoff (Qsb), evaporation (E), and transpiration (T)) without (left) and considering (right) ground cover parameters. Forcing data is GCM output.

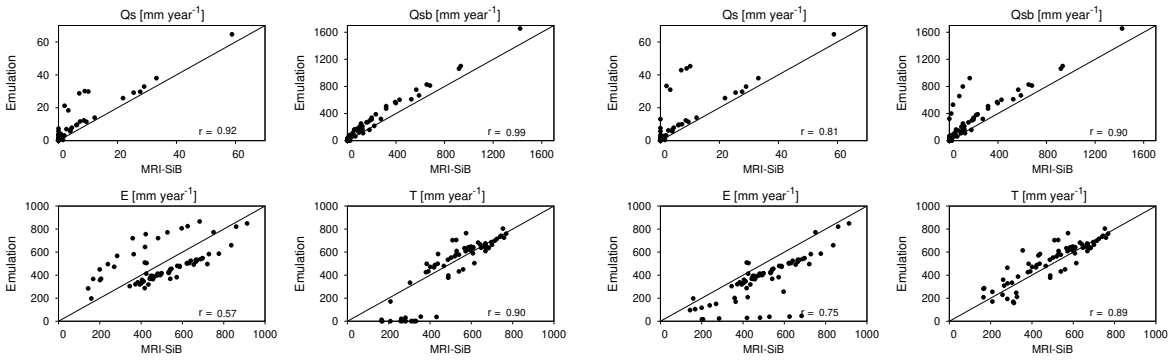

(a) Scatter plot without ground cover parameters (B6).

(b) Scatter plot by using ground cover parameters.

Figure 4.28: Similar to Figure 4.27 but for scatter plot of grid cells within the target basin. r value is correlation coefficient.

Fraction of Photosynthetically Active Radiation.

Table 4.15 shows a comparison of mean annual water budget between MRI–SiB, current emulation model (experiment B6, without considering ground cover), and the experiment which

considers parameters related to the ground cover. As seen, transpiration estimated by this experiment is closer to MRI–SiB result. However, evaporation is much underpredicted. In addition, subsurface runoff estimation is overestimated by this experiment.

Figure 4.27 shows the spatial pattern of differences in mean annual water budget by experiments without and with ground cover to MRI–SiB results. Spatial distributions of evaporation and transpiration between these two experiments show appearent differences. The differences in transpiration between simulation with ground cover and MRI–SiB is lower than that without ground cover. However, the evaporation in the grid cells, which considered ground cover parameters, underpredicted the evaporation by MRI–SiB.

Figure 4.28 show scatter plot of mean annual water budget by experiments without and with ground cover to MRI–SiB results. As seen, the correlation of surface and subsurface runoff by the simulation considering ground cover is worse than that without ground cover. The correlation of evaporation seems better, while there is not much difference in the correlation of transpiration.

In conclusion, this experiment shows that considering the parameters related to the ground cover layer does not seem to improve the results of the emulation model. It is because of the difference in vegetation schemes in the two models.

4.7.2 Transpiration schemes

Another difference between the two LSMs is the treatment of abstraction of soil moisture by transpiration. In SiBUC, reduction of soil moisture by transpiration is applied for soil moisture of the first and second soil layer only, as shown in the following equations.

$$E_{\mathrm{dc},1} = E_{\mathrm{dc}} \times \frac{D_1}{D_1 + D_2} \tag{4.25}$$

$$E_{\mathrm{dc},2} = E_{\mathrm{dc}} \times \frac{D_2}{D_1 + D_2} \tag{4.26}$$

$$\tag{4.27}$$

with, E_{dc}, $\mathrm{E}_{\mathrm{dc},1}$, $\mathrm{E}_{\mathrm{dc},2}$ corresponds to total transpiration rates, rate of extraction of transpired water from first and second soil layers, respectively.

On the other hand, in MRI–SiB, all three soil layers implement the abstraction of soil moisture by transpiration.

$$E_{dc,i} = \frac{D_i}{z_d} \left(\frac{\psi_i - \psi_l - Z_T}{\overline{r_{\mathrm{p}lant}} + \overline{r_{\mathrm{s}oil}}} \right) \rho_{\mathrm{w}} \tag{4.28}$$

with, $\mathrm{E}_{\mathrm{dc},}i$, ψ_l, z_d, z_T, $\overline{r_{\mathrm{p}lant}}$, and $\overline{r_{\mathrm{s}oil}}$ corresponds to rate of extraction of transpired water from all three layers, leaf water potential (m), rooting depth (m) , height of transpiration source (m), area–average resistance imposed by the plant vascular system (s), and area–average resistance of soil and root system (s) respectively.

Eq. (4.7.2) is applied with values of the parameters related to canopy and ground covers, and are performed in both vegetation layers.

That difference in the transpiration treatment might have an impact on the water budget estimation. However, a more detailed analysis is necessary to investigate the impacts.

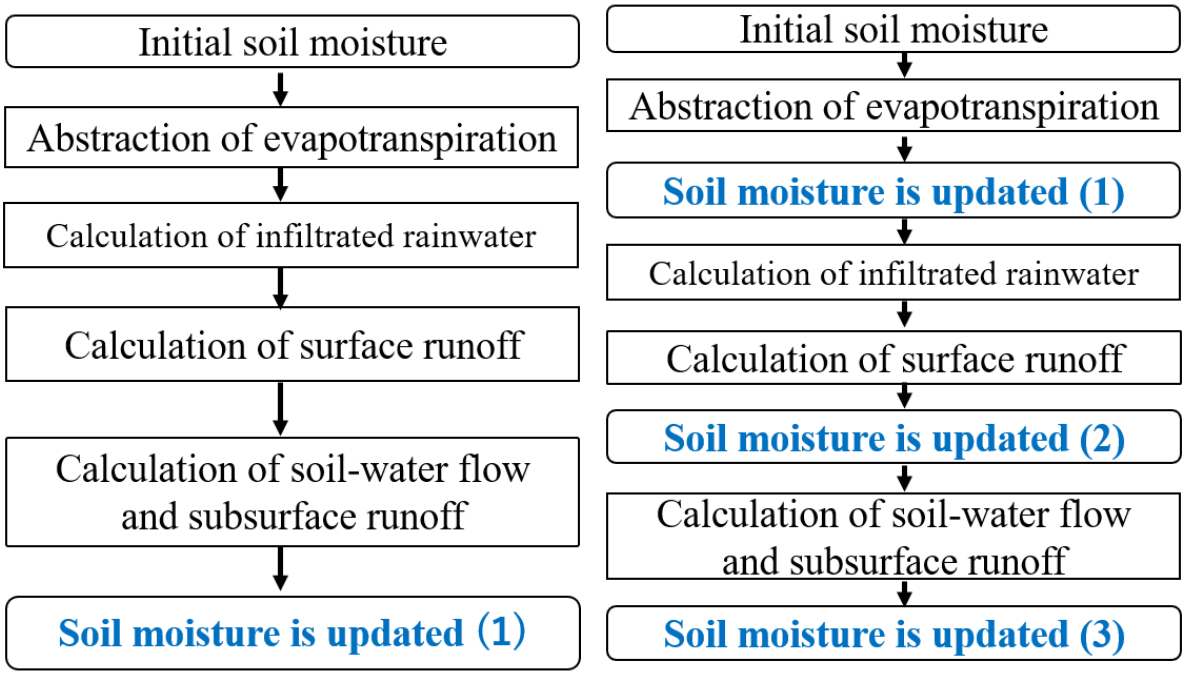

(a) Method in SiBUC.

(b) Method in MRI-SiB.

Figure 4.29: Algorithm of soil moisture update for each time step.

4.7.3 Initial value of soil moisture

Differences in the runoff estimated by MRI–SiB and SiBUC might also be affected by the soil moisture value used for the runoff calculation. In SiBUC, the surface and subsurface runoff are calculated by using the initial soil moisture value of each time step. In one time step, the soil moisture is updated only once for the next time step, as shown in Figure 4.29(a).

Figure 4.29(b) shows the algorithm of soil moisture updates in each time step in MRI–SiB. As seen, the initial soil moisture of each time step is first reduced by evapotranspiration components before the runoff is calculated. After that, the soil moisture is updated due to the impacts of infiltrated rainwater and surface runoff estimation. Next, it is updated for the next time step by considering the soil–water flow and subsurface runoff. Based on this algorithm, the soil moisture value used in MRI–SiB for calculating the runoff should be lower than that in SiBUC, which might impact the lower runoff estimation. However, a detailed analysis is necessary to figure out how much impacts such differences on runoff calculation.

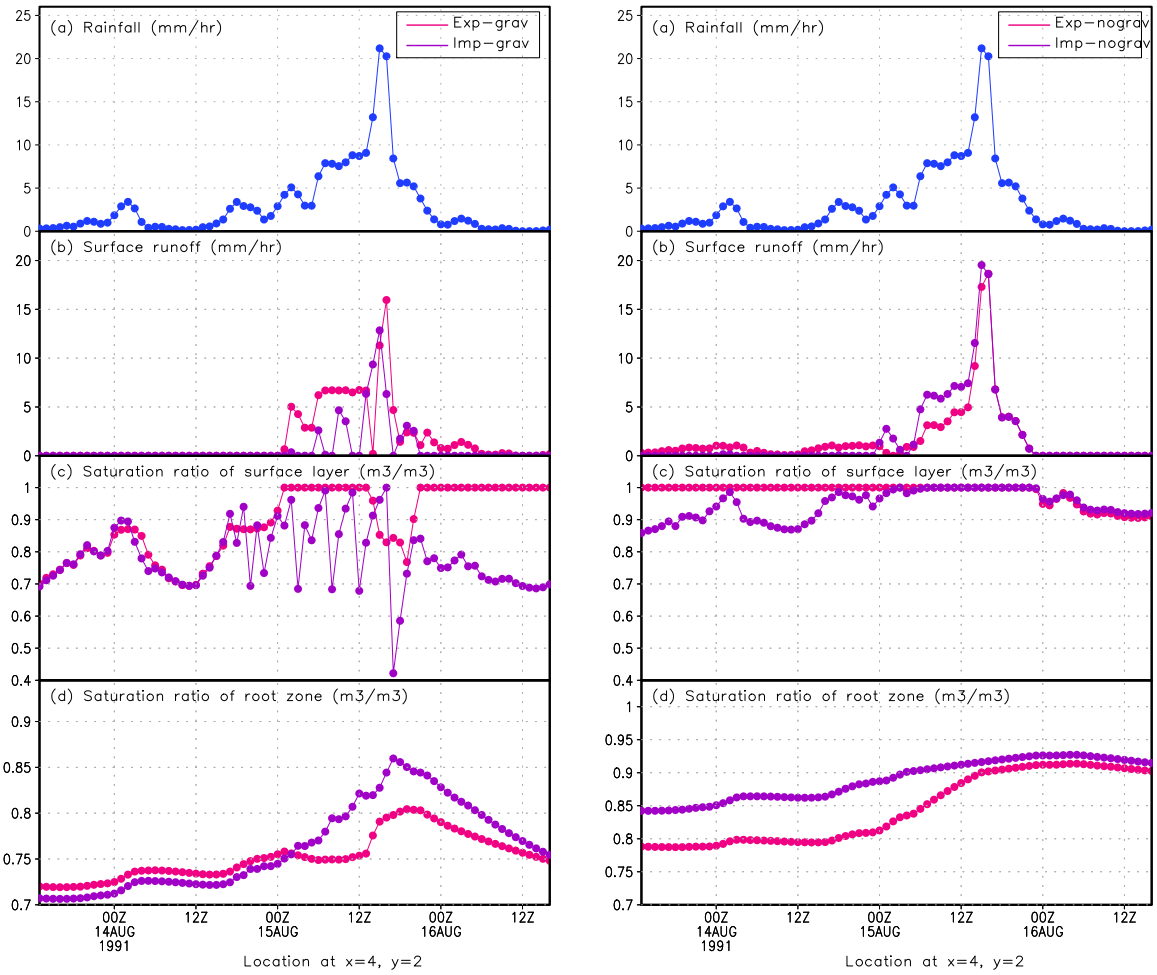

(a) Simulation by considering gravitational drainage for calculating soil–water flow.

(b) Simulation without considering gravitational drainage for calculating soil–water flow.

Figure 4.30: Time series of rainfall, surface runoff, soil moisture of surface layer and recharge zone, respectively. Pink and purple lines represent an explicit–midpoint and semi–implicit methods, respectively.

4.7.4 Time integration methods for solving Richards equation

As mentioned earlier, SiBUC and MRI–SiB apply different time integration methods to solve the Richards equation. Impacts of the different methods have been investigated on soil moisture estimation. It is noticed that in MRI–SiB, the gravitational drainage term is not considered for calculating soil–water flow between adjacent soil layers. However, this term should not be negligible in the Richards equation.

Here, we analyzed in detail the impacts of considering gravitational drainage on soil moisture estimation. The timestep is set as hourly for input and output files.

Figure 4.30(a) shows a comparison of soil moisture between an explicit–midpoint method (in SiBUC) and a semi–implicit method (in MRI–SiB). Soil parameter of this cell is: $K_{\rm s}$ is 2.00$\times$ 10^{-5} m s^{-1}, $\psi_{\rm s}$ is -0.086 m, $\theta_{\rm s}$ is 0.42, and B is 7.12. These cells were selected as the impacts of changing different methods are significant in estimating soil moisture of the surface layer. By using the semi–implicit method, the soil wetness of the top layer shows some oscillations. While the estimated soil moisture seems more stable by using the explicit method.

Figure 4.30(b) shows a comparison of soil moisture between both methods by neglecting the gravitational flow in the Richards equation. As seen, the estimated soil moisture of surface layer by the implicit method seems more stable than that by considering the gravitational drainage. On the other hand, the estimated result by the explicit method also shows stable results.

From this comparison, it is thought that a more detailed investigation may be necessary to evaluate the current methods in both LSMs. For instance, by performing a benchmark test by comparing the estimated soil moisture by each method with a Richards equation model (such as HYDRUS (Simunek *et al*.,2008), etc.), as a reference model. Evaluation of calculation method for soil moisture is essential as water balance and energy partitioning strongly depend on the soil moisture.

4.8 Conclusions

In this study, we investigated runoff generation schemes in two LSMs: SiBUC and MRI–SiB. Throughout our investigation, we found different settings in both LSMs, which mainly affected runoff and river discharge estimation. To investigate the impacts on those settings in a controlled manner, we developed MRI–SiB emulation model by adopting MRI–SiB's settings in SiBUC. By incorporating MRI–SiB's land surface parameters, model structures, and time integration methods for soil schemes, the runoff characteristics could be well emulated by SiBUC. The findings of this study provide a better understanding of the physical representation of runoff processes in both LSMs and identify the potential bias of the underlying runoff generation mechanisms in the LSMs, as has been suggested by Fallon *et al*., 2011. However, it is beyond the scope of this study to determine which model settings are better among both LSMs since the simulated discharge by both models has not yet been evaluated against observed river flow. The next chapter evaluates the model performance and proposes better settings for their reproducibility of observed flow.

Chapter 5

Improvement of land surface models to reproduce long–term observed river flow

Abstract

In this chapter, simulated discharge forced by the runoff from the SiBUC and MRI–SiB emulation models was evaluated by comparing it with 30 years of observed river flow data. The two LSMs were forced by the observed rainfall and reanalysis of atmospheric data. For long–term evaluation, the discharge simulated by the SiBUC performed better than the flow estimated by the MRI-SiB to reproduce the monthly observed discharge. In particular, the SiBUC performed well at reproducing the discharge observed during wet years (when annual rainfall is higher than the climatological mean). In contrast, the discharge simulated by the MRI–SiB was better than the flow estimated by the SiBUC during dry years (when annual rainfall is lower than the climatological mean). Therefore, using some SiBUC settings in the MRI–SiB, and vice versa, could enhance the performance of each model at reproducing the long–term observed river flow.

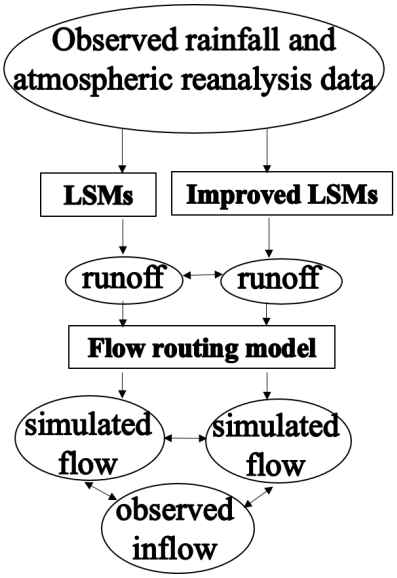

Figure 5.1: Framework in this study to evaluate and improve LSMs's performance. LSMs used in this study are SiBUC and MRI–SiB emulation model.

5.1 Introduction

The original purpose of developing land surface models (LSMs) is to provide boundary conditions for climate models or numerical prediction models. The LSMs now has an increasing scope; it is not only utilized by meteorologists but also hydrologists. It is widely used as an efficient tool to project hydrological changes under current and future climate conditions in the hydrologic field. Several studies have pointed out the bias of runoff from the LSMs for simulating river discharge. Investigation of the runoff generation processes plays an essential role in understanding the sources of uncertainty in the model. Sensitivity analysis for analyzing the LSMs' behavior on runoff generation has been conducted in previous studies. For example, a study by Takata and Hanasaki (2021) analyzed the behavior of MATSIRO on runoff generation mechanisms. This study aimed to evaluate the performance of two LSMs: SiBUC and emulation of MRI–SiB (developed in the previous section) on reproducing observed river discharge and propose better settings for their improvement.

5.2 Methodology

Figure 5.1 shows a methodology in this study to evaluate and improve the LSMs' performance. Both SiBUC and MRI–SiB emulation models were forced with observed rainfall and atmospheric reanalysis data. Streamflow simulated by both LSMs was evaluated by comparing it with observed river flow. Rainfall data from CHIRPS dataset , and reanalysis atmospheric data were obtained from JRA–55, are used in this study.

Numerical simulations in both LSMs were performed from 1981–2013. The first–three years' results were discarded as spin–up, and the last 30 years' results were used for analysis. Both LSMs were developed with a 5 km mesh size, the same as the spatial resolution of the rainfall dataset.

First, the water budget estimated by both LSMs was analyzed. Next, simulated streamflow forced by runoff from both LSMs was evaluated by comparing it with the observed inflow into Bhumibol Dam. The advantages and limitations of each LSM were analyzed with respect to the reproducibility of observed streamflow. Some strategies of improvement were proposed to enhance their performance in reproducing the observed inflow.

Performance indices to evaluate the simulated discharge are Nash–Sutcliffe Efficiency (NSE), Root Mean Square Coefficient–observations standard deviation ratio (RSR), and percent bias (PBIAS), as shown in Eq. (5.1), Eq. (5.2), Eq. (5.3).

$$NSE = 1 - \frac{\sum_{i=1}^{N} \left(M_{\mathrm{i}} - O_{\mathrm{i}}\right)^2}{\sum_{i=1}^{N} \left(O_{\mathrm{i}} - \overline{O}\right)^2} \tag{5.1}$$

$$RSR = \frac{\sqrt{\sum_{i=1}^{N} \left(M_{\mathrm{i}} - O_{\mathrm{i}}\right)^2}}{\sqrt{\sum_{i=1}^{N} \left(O_{\mathrm{i}} - \overline{O}\right)^2}} \tag{5.2}$$

$$PBIAS = \frac{\sum_{i=1}^{N} \left(M_{\mathrm{i}} - O_{\mathrm{i}}\right)}{\sum_{i=1}^{N} O_{\mathrm{i}}} \times 100 \tag{5.3}$$

with, M_{i} and O_{i} are discharge by the emulation model and MRI–SiB, respectively, and $\overline{M}$ and $\overline{O}$ are mean of simulated discharge by the emulation model and MRI–SiB, respectively.

NSE values range between negative infinity to 1, with being equal to 1 is the perfect fit, and the values lower than 0 are generally assumed as poor performance. RSR is calculated as

Table 5.1: Performance ratings for a monthly time step (based on Moriasi *et al*. 2007).

Performance ratings	NSE	RSR	PBIAS
Very good	$0.75 < \text{NSE} < 1.00$	$0.00 < \text{RSR} < 0.50$	$\text{PBIAS} < \pm 10$
Good	$0.65 < \text{NSE} < 0.75$	$0.50 < \text{RSR} < 0.60$	$\pm 10 < \text{PBIAS} < \pm 15$
Satisfactory	$0.50 < \text{NSE} < 0.65$	$0.60 < \text{RSR} < 0.70$	$\pm 15 < \text{PBIAS} < \pm 25$
Unsatisfactory	$\text{NSE} < 0.50$	$\text{RSR} > 0.70$	$\text{PBIAS} > \pm 25$

the ratio of root mean square error (RMSE) to the standard deviation of the observed data. In fact, the RMSE is more commonly used for evaluating the model performance, with the lower the RMSE value, the better the model performance. However, in this study, RSR was selected because there is a guideline based on the recommendation from Singh *et al*. (2004) to qualify what is considered as a low RMSE. PBIAS measures the accumulation of differences in the predicted and observed streamflow, and it indicates the tendency of the simulated value to be larger or smaller than the reference value. The optimum value of PBIAS is 0. Similar to RSR, the lower the scores, the more accurate the model performance.

In this study, a guideline based on Moriasi *et al*. (2007) is used to evaluate the model performance for a monthly time step, as shown in Table 5.1. Generally, lower scores are estimated for evaluation on shorter steps than longer ones (for instance, daily vs. monthly). Therefore, they recommend to modify this guideline accordingly for evaluating the simulated discharge with shorter time steps (such as daily streamflow).

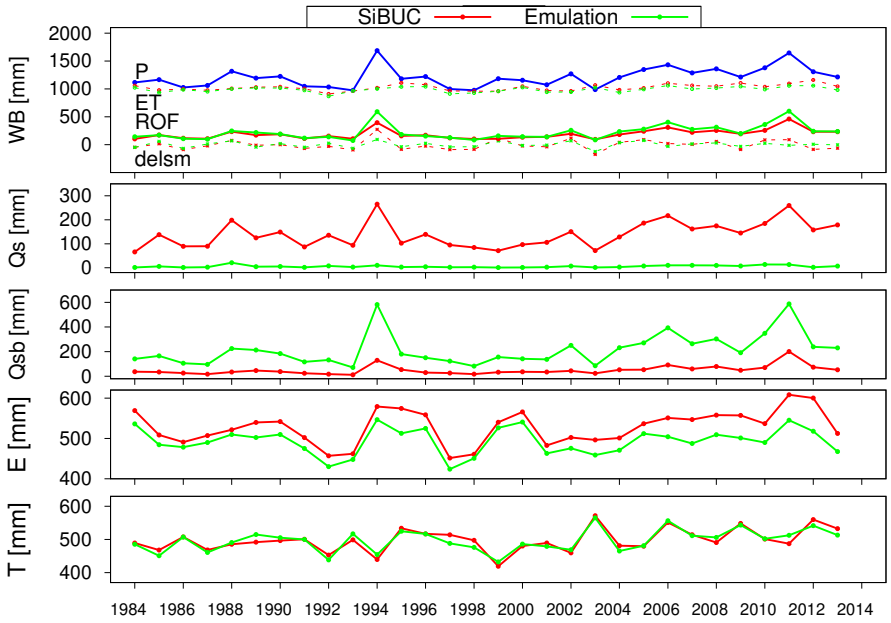

Figure 5.2: Time series of annual water budget components estimated by SiBUC (red line) and MRI–SiB (green line) forced by observed hydrometeorological data. P, ET, ROF, delSM, Qs, Qsb, E, and T represents precipitation, evapotranspiration, runoff, change of soil moisture, surface runoff, subsurface runoff, evaporation, and transpiration, respectively.

Table 5.2: Similar to Figure 5.2 but for 30–years–mean water budget components (unit: mm year^{-1}).

LSM	P	ET	ROF	Qs	Qsb	E	T	delsm
SiBUC	1209	1025	189	138	50	527	498	-4
MRI–SiB emulation model		990	219	6	213	493	496	0

5.3 Comparison of water budget estimated by SiBUC and MRI–SiB emulation model

Figure 5.2 shows a comparison of annual water budget by SiBUC and MRI–SiB emulation model. Table 5.2 shows 30–years–mean of water budget from both LSMs. In general, evapotranspiration and runoff estimated by SiBUC were close to the emulation model. However, the emulation model estimated lower evapotranspiration and higher runoff than SiBUC in some years, such as 1994, 2011, etc. In those years, the annual rainfall was higher than the climatological mean.

Both LSMs have shown opposite runoff characteristics. SiBUC generated high surface runoff and low subsurface runoff. In contrast, the subsurface runoff was dominant in the emulation model. These differences are owing to different settings in both LSMs have already been analyzed in the previous chapter.

Transpiration estimated by both LSMs was close. While evaporation calculated by SiBUC was higher than the emulation model.

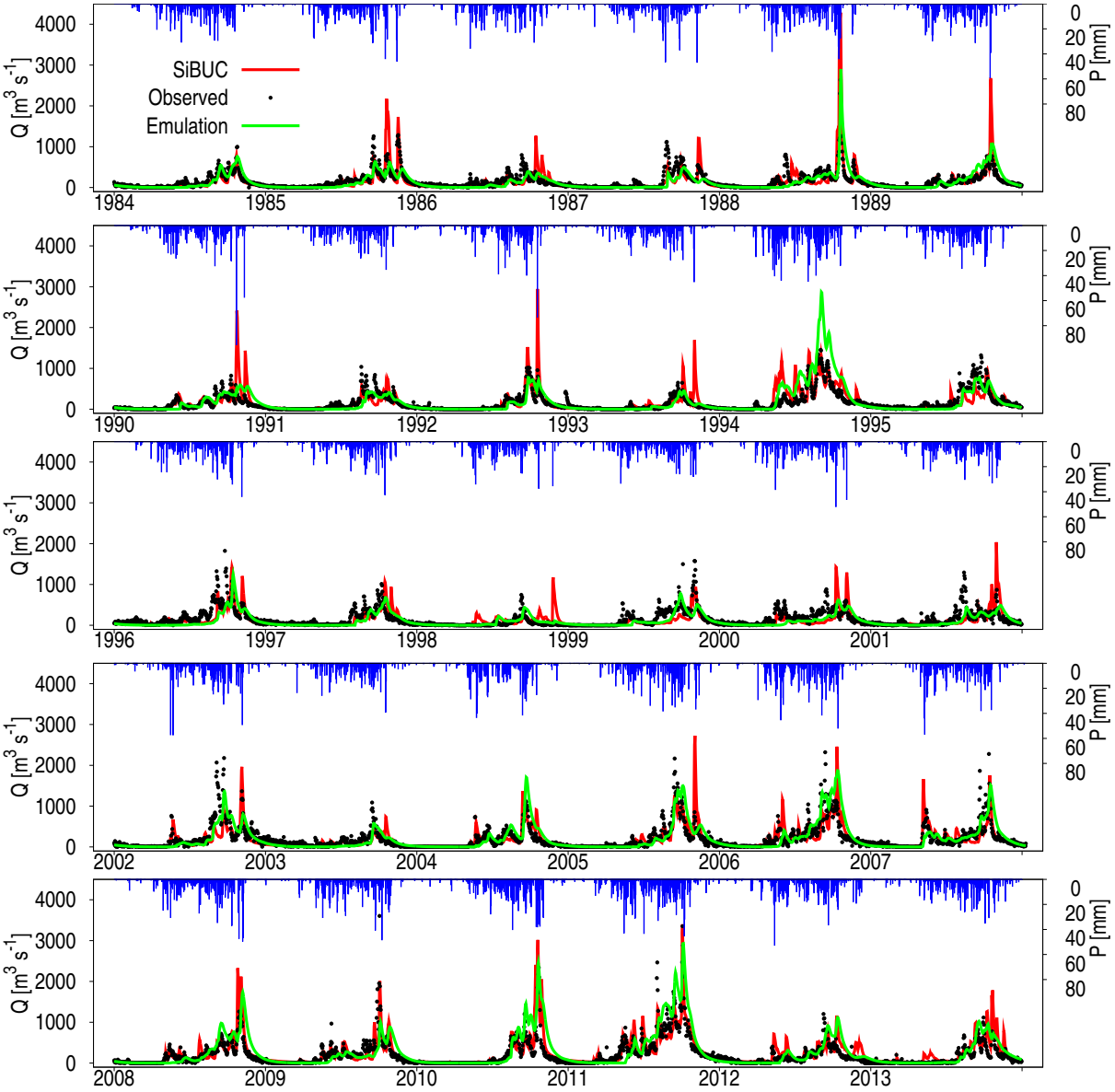

Figure 5.3: Comparison of daily discharge from observation (black dot) and simulation by SiBUC (red line) and MRI–SiB emulation (green line) from 1984–2013.

5.4 Evaluation of river discharge simulated by runoff from SiBUC and MRI–SiB emulation model

Figure 5.3 shows a comparison of daily discharge from observation and simulation by SiBUC and MRI–SiB emulation model for 30 years. Figure 5.3 shows an evaluation of the simulated daily discharge by both LSMs for the whole period with respect to the observed streamflow. Based on the results of performance indices, overall, SiBUC shows slightly better performance

Table 5.3: Evaluation of 30–years daily discharge.

LSM	NSE	RSR	PBIAS
SiBUC	0.35	0.81	-0.14
Emulation	0.32	0.82	2.87

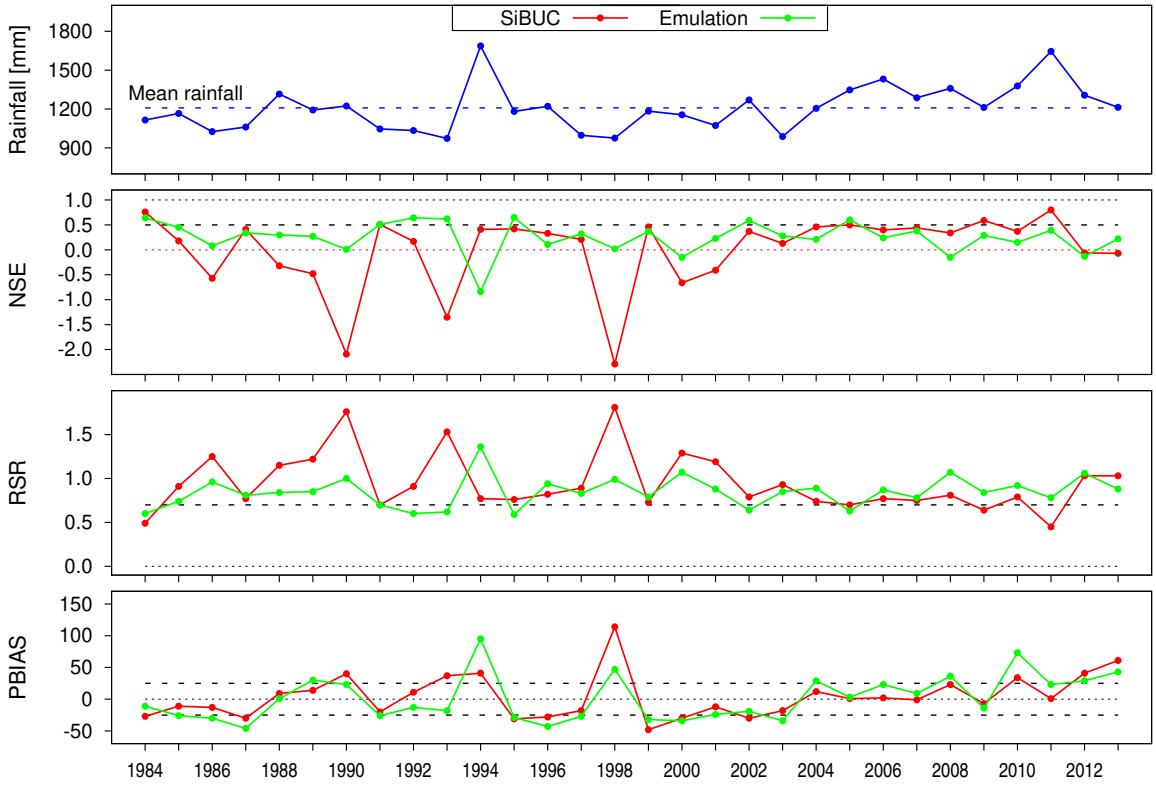

Figure 5.4: Evaluation of indices performance of daily discharge simulated by SiBUC (red line) and MRI–SiB (green line) for each year. Black dash line indicates a limit of each index for 'satisfactory' performance. Negative value of NSE means 'poor' performance. Optimum value of NSE is 1, while that of RSR and PBIAS is 0.

than the emulation model. Except for PBIAS, NSE and RSR scores by both LSMs seem acceptable, although not much adequate. The low scores of PBIAS in the two LSMs are owing to high variations of positive and negative bias.

We also analyzed the performance of each model for each year. In this analysis, annual rainfall was categorized into the wet and dry years. For simplicity, the climatological mean of 30 years annual rainfall was used as a threshold to determine wet and dry years. Wet years were defined as the years with annual precipitation exceeding climatological mean rainfall, and

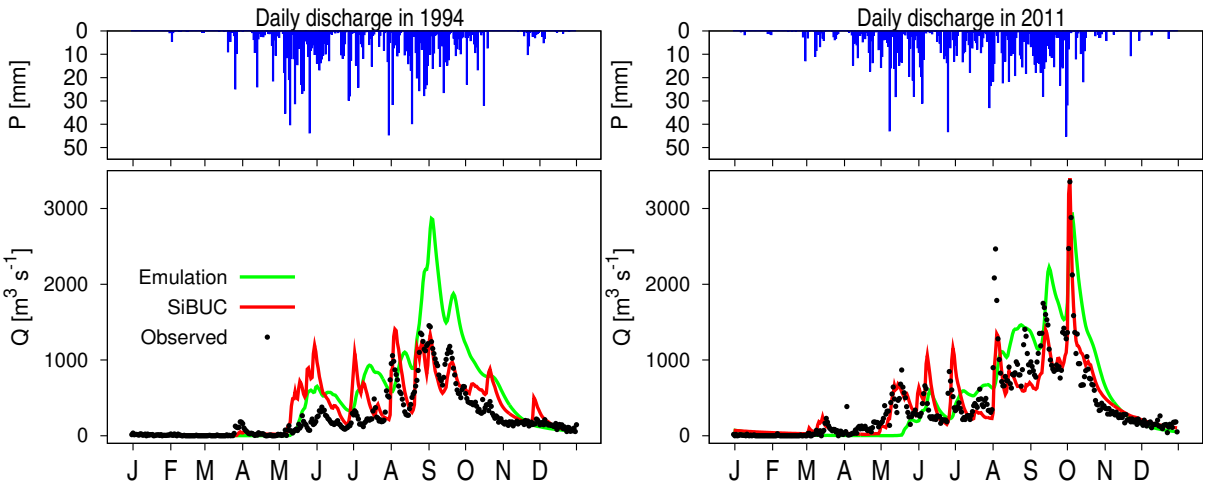

Figure 5.5: Daily discharge from observation (black dot) and simulation by SiBUC (red line) and MRI–SiB (green line) in 1994 and 2011.

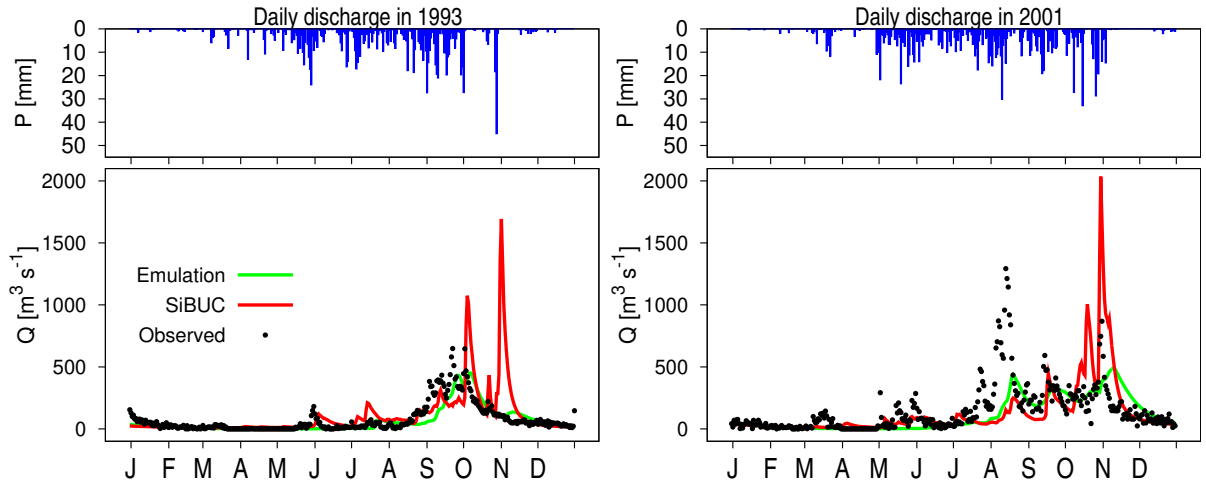

Figure 5.6: Daily discharge from observation (black dot) and simulation by SiBUC (red line) and MRI–SiB (green line) in 1993 and 2001.

those with less than the threshold were identified as dry years. Based on this definition, the simulation periods were divided into 14 wet and 16 dry years.

Figure 5.4 shows an evaluation of model performance for daily discharge in each year. It seems both LSMs show different performances depending on rainfall amount, although the correlation is not so clear. Reproducibility of the observed streamflow by SiBUC seems to be better than the emulation model in wet years, such as in 1994 and 2011. The simulated discharge in these years is shown in Figure 5.5. In both years, the estimated flow by the emulation

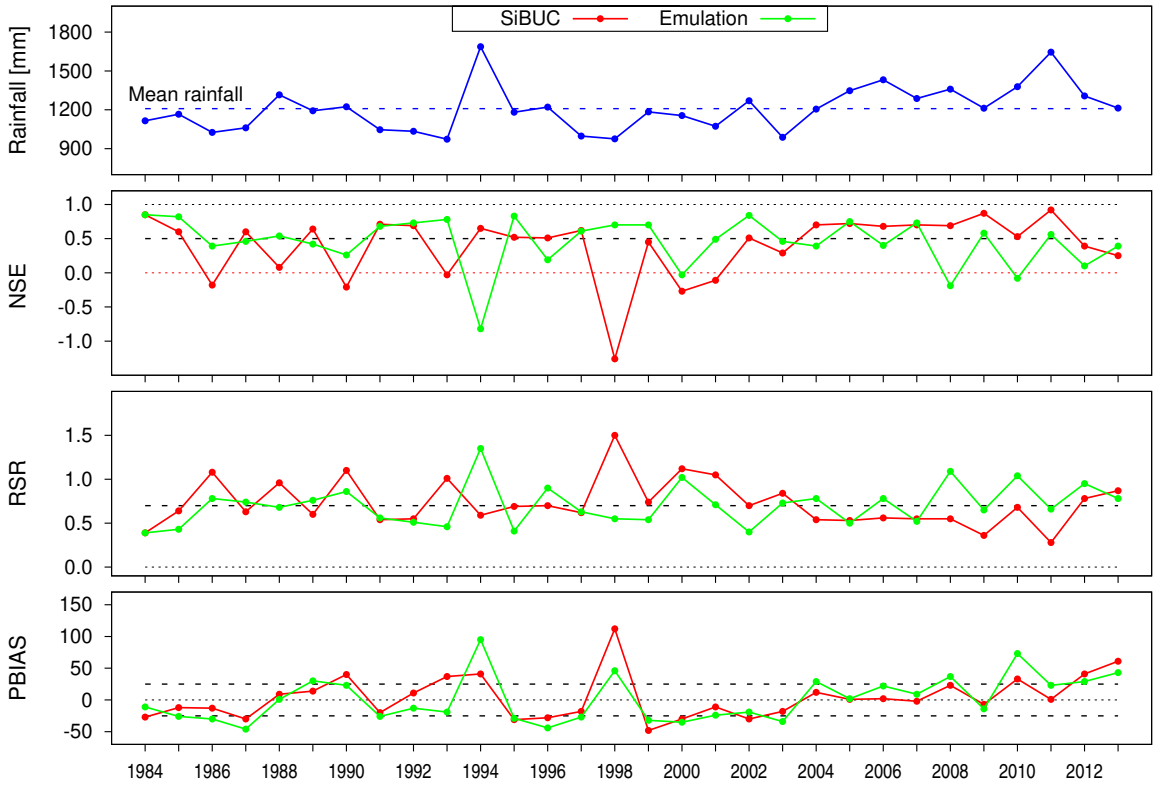

Figure 5.7: Similar to Figure 5.4 but for evaluation of monthly discharge.

model shows significantly overpredicted the observed discharge, which resulted in poor performance scores. The discharge by the emulation model also failed to reproduce the observed peak flow in 2011, in contrast to SiBUC, which showed an excellent performance.

On the other hand, reproducibility of observed flow by the emulation model seems better than SiBUC in dry years, for instance, in 1993 and 2001. Figure 5.6 shows the simulated streamflow in these years As seen, the discharge by SiBUC has overestimated the observed flow due to the high intensity of rainfall. In contrast, the discharge by the emulation model does not show such a high response. The performance indices by SiBUC show negative NSE scores, which indicate a poor model performance. In comparison, the emulation model shows positive NSE scores in these years, indicating an acceptable performance.

Evaluation for monthly discharge simulated by both LSMs is also analyzed. Comparison of monthly streamflow from observation and simulation by SiBUC and MRI–SiB emulation is shown in Figure 5.8. Table 5.4 shows an evaluation of 30 years monthly discharge simulated by SiBUC and the emulation model with respect to observed river flow. Based on the performance ratings shown in Table 5.1, except for PBIAS, SiBUC delivers satisfactory performance, while

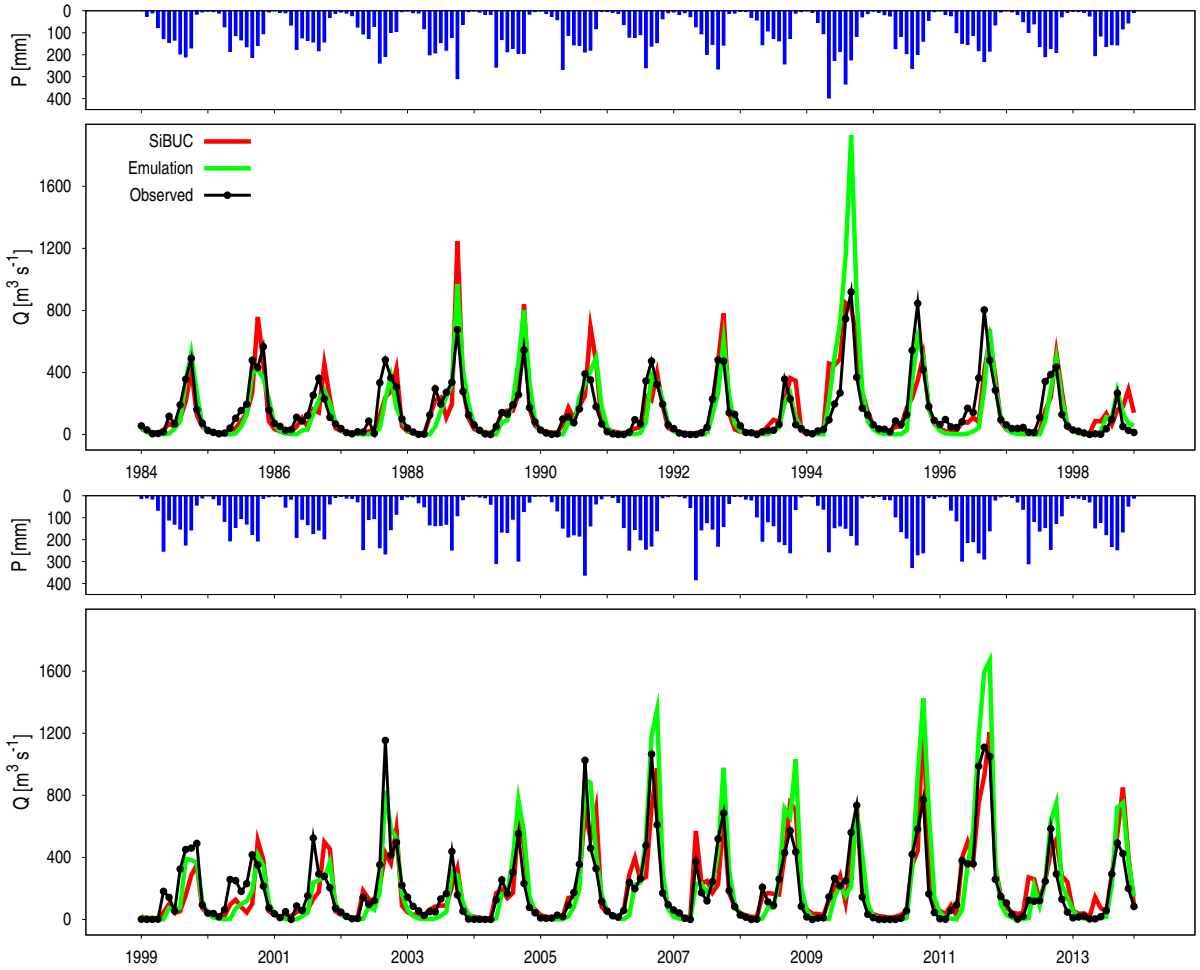

Figure 5.8: Time series of monthly discharge by SiBUC (red line) and MRI–SiB emulation (green line) from 1984–2013.

Table 5.4: Evaluation of 30–years monthly discharge.

LSM	NSE	RSR	PBIAS
SiBUC	0.62	0.62	-0.27
Emulation	0.49	0.72	2.85

the emulation model is less adequate.

Similar to the evaluation of the daily discharge, performance by each LSM varies depending on the year. Figure 5.7 shows the evaluation of simulated monthly discharge for each year. Even though SiBUC shows better scores for the whole simulation period, it has more negative NSE scores for the individual year than the emulation model, indicating poor performance. How-

ever, both LSMs have their advantages and limitations in reproducing the long–term observed streamflow. For example, SiBUC shows a good ability in reproducing high flow. However, it sometimes estimates too high discharge during intense rainfall events. On the other hand, the performance of the emulation model on reproducing high flow needs to be improved. However, the emulation model does not show such overestimation of discharge during high rainfall events. From this analysis, it is thought that the advantages of one LSM are the limitations of another LSM. Therefore, improving the performance of both LSMs can be proposed by adopting some settings of one LSM to another LSM.

Table 5.5: Experimental designs for improving MRI–SiB emulation model.

Experiment	Revised settings
1	soil characteristics parameters
2	soil depth
3	both soil characteristics parameters and soil depth
4	neglecting P_2 structure
5	considering gravitational drainage for soil–water flux equation
6	combine experiment 3 and 4
7	combine experiment 3 and 5

Table 5.6: Comparison of original and revised soil parameters in emulation model. The revised values are based on SiBUC parameters.

Parameters	Original	Revised
Saturation ratio $\theta_{\rm s}$ ($\rm m^3\ m^{-3}$)	0.42	0.478
B power	7.12	8.41
Saturated hydraulic conductivity $K_{\rm s}$ (m $\rm s^{-1}$)	2.00×10^{-5}	1.440×10^{-6}
Saturated matric potential $\psi_{\rm s}$ (m)	-0.086	-0.63
Depth of root zone D_2 (m)	1.5	2.5
Depth of recharge zone D_3 (m)	3.5	5.0

5.5 Improvement strategies for MRI–SiB emulation model

5.5.1 Overview

In this analysis, we proposed some improvement strategies for MRI–SiB emulation model, focusing on the reproducibility of observed streamflow in wet years. As shown earlier, the emulation model shows too much overprediction of observed flow during these years. Therefore, the improvement is proposed to reduce the high positive bias by the emulation model.

5.5.2 Experimental designs

Figure 5.5 shows experimental designs to improve the performance of the emulation model. Seven experiments were conducted by revising soil parameters, model structures, and both soil parameters and model structures. In particular, all settings in MRI–SiB emulation were revised

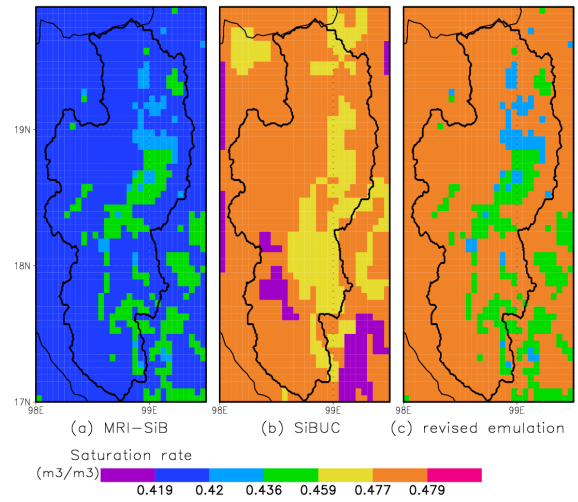

(a) Saturation rate $\theta_{\rm s}$ (m^3 m^{-3}).

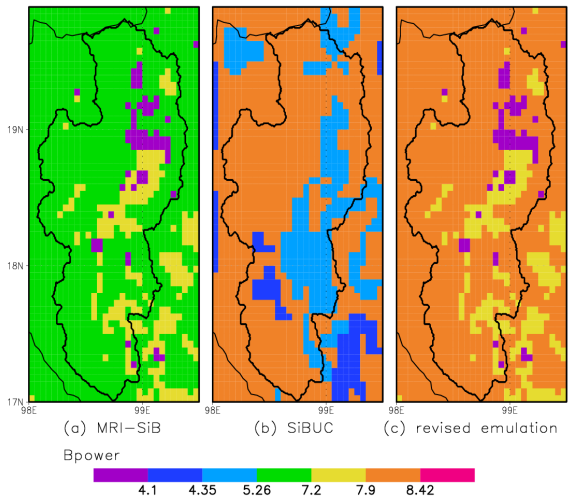

(b) B power.

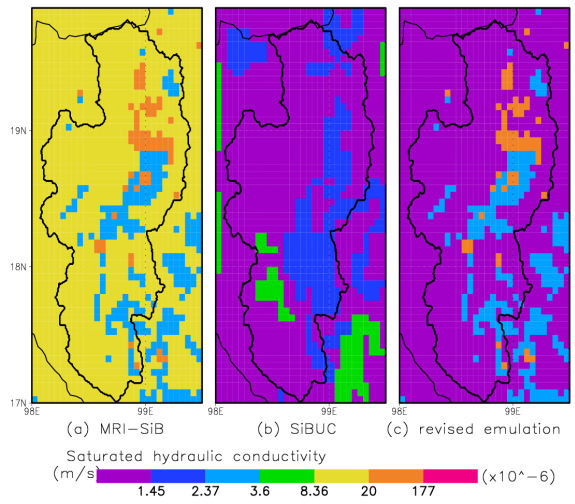

(c) Saturated hydraulic conductivity $K_{\rm s}$ (m s^{-1}).

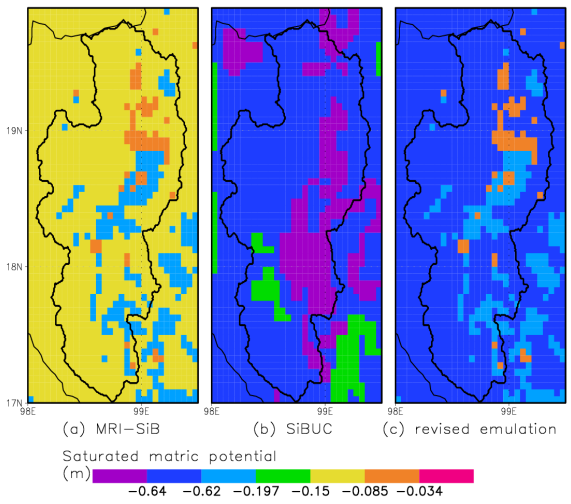

(d) Saturated matric potential $\theta_{\rm s}$ (m).

Figure 5.9: Spatial pattern of soil characteristics parameters in (a) emulation model (based on MRI–SiB parameters), (b) SiBUC, and (c) revised emulation.

by adopting settings in SiBUC.

For revising the soil parameters, among 15 variables used, only the most sensitive parameters related to runoff generation were modified to improve the emulation model. Those parameters were divided into two groups: soil characteristics parameters (saturated hydraulic conductivity $K_{\rm s}$, saturated matric potential $\psi_{\rm s}$, saturation ratio $\theta_{\rm s}$, and B power), and parameters related to soil depth (depth of root zone D_2 and recharge zone D_3). The soil depth of the surface layer is

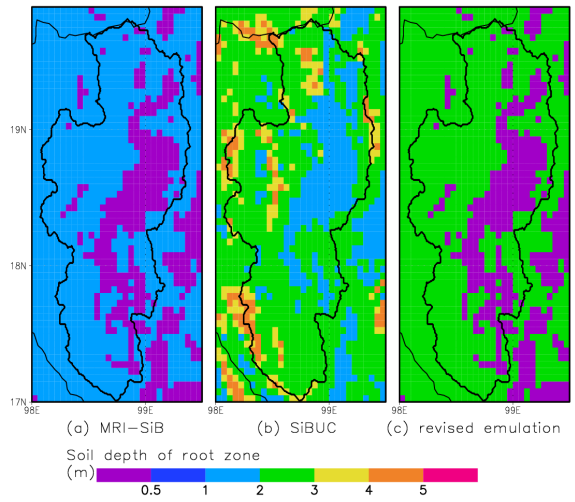

(a) Depth of root zone D_2 (m).

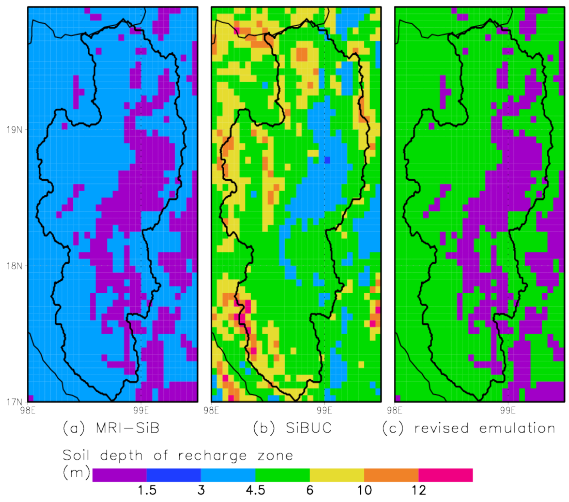

(b) Depth of recharge zone D_3 (m).

Figure 5.10: Spatial pattern of soil depth in (a) emulation model (based on MRI–SiB parameters), (b) SiBUC, and (c) revised emulation.

the same in both LSMs (=0.02 m), and it is not changed for the improved emulation model.

We also considered spatial distributions of the soil parameters. As mentioned in the previous chapter, the soil parameter in SiBUC is set based on soil types, while in the emulation model, it is dependent on vegetation types. To address such differences, we revised only the parameter values of the dominant vegetation types in the emulation model and incorporated the parameter settings of major soil types in SiBUC.

Figure 5.9 shows the spatial pattern of soil characteristics parameters in the emulation model (based on MRI–SiB parameters), SiBUC, and revised emulation model (based on SiBUC parameters). For instance, as shown in Figure 5.9(a), the dominant value of saturation ratio in MRI–SiB is 0.42, and SiBUC is 0.478. For the sensitivity experiments, that value of the emulation model was revised from 0.42 to 0.478. All soil characteristics parameters in the emulation model were modified in a similar manner. Adjusting the parameters for minor vegetation types might not be necessary as the impacts may be less dominant on the water budget estimation.

Figure 5.10 shows spatial distributions of soil depth of root zone and recharge zone in the emulation model, SiBUC, and revised emulation. As seen, SiBUC shows various depths regardless of the soil class. Soil depth in the emulation model was revised by selecting a representation of dominant depth in SiBUC. For example, the dominant depth of root zone in MRI–SiB

is 1.5 m, and in SiBUC is 2.5 m. Therefore, soil depth of the second layer in emulation model was revised from 1.5 to 2.5 m.

Table 5.6 shows a comparison of original and revised parameters in the emulation model based on SiBUC parameters. Experiments 1–3 and 6–7 were conducted using the revised parameters to investigate whether it could improve the emulation model's ability to reproduce observed discharge.

As seen in Table 5.5, first, the impact of changing soil parameters was investigated. Experiments 1, 2, and 3 were performed by modifying soil characteristics parameters, soil depth, and the combination of both groups. Next, impacts of neglecting P_2 structure and incorporating gravitational drainage for soil–water flux calculation was analyzed in experiments 4 and 5, respectively. Experiments 5 and 6 were performed to examine the effects of changing both soil parameters and model structures.

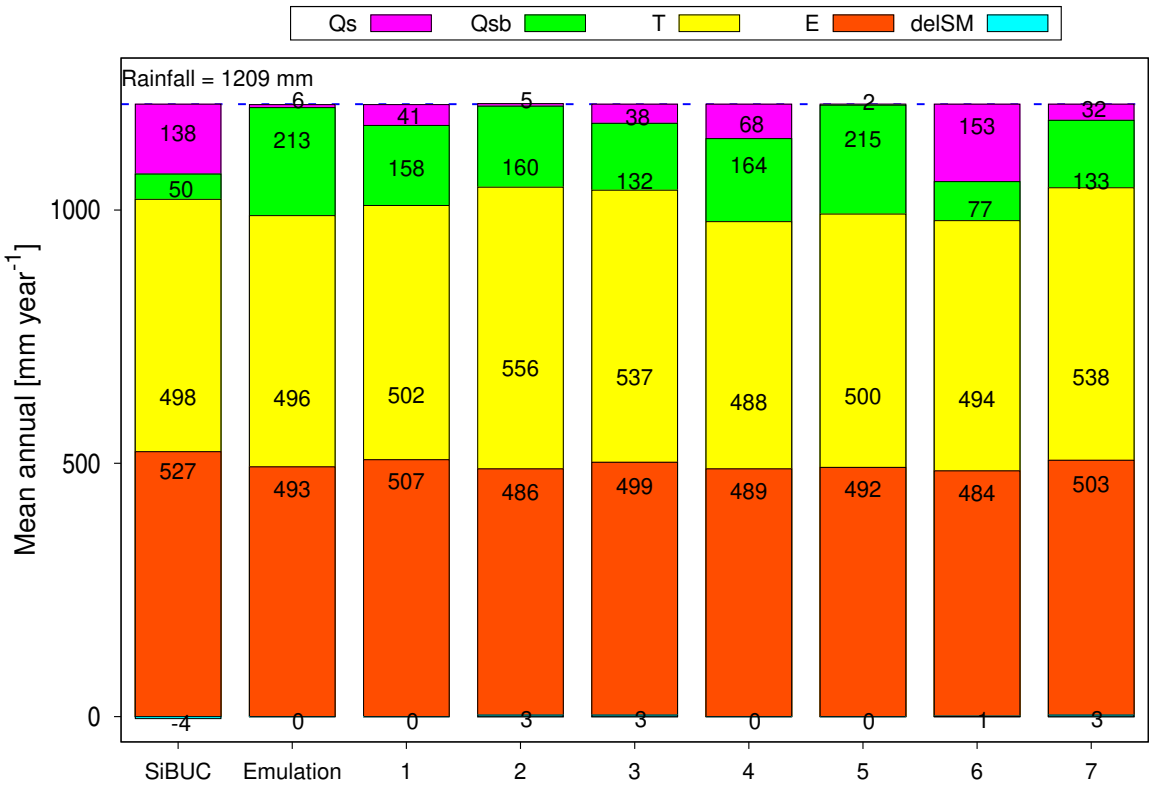

Figure 5.11: Comparison of water budget components (surface runoff (Qs), subsurface runoff (Qsb), evaporation (E), transpiration (T), and change of soil moisture (delSM)) between SiBUC, MRI–SiB emulation, and each experiment of revised emulation model. Blue dash–line represents a 30–years-mean annual rainfall.

5.5.3 Changes of water budget by revised emulation model

Figure 5.11 shows a comparison of water budget components between SiBUC, MRI–SiB emulation, and each experiment of revised emulation model. Experiment 1–3 was performed to investigate the impacts of changing soil characteristics, soil depth, and both parameters. In experiment 1, performed by adopting SiBUC's soil characteristics parameters, surface runoff increased, and subsurface runoff decreased compared to MRI–SiB. It is because of lower infiltration rates caused by SiBUC's parameters settings (lower saturated hydraulic conductivity, lower saturated matric potential, etc.). In experiment 2, subsurface runoff is significantly lower than the emulation model. As the soil depth of the third layer is deeper, the soil saturation is more delayed, resulting in the lower subsurface runoff. By changing both soil characteristics and soil depth, surface runoff increased and subsurface runoff decreased, similar to the exper-

iment 1. However, the estimated subsurface runoff is much lower because the soil takes a long time to reach saturation than in thinner soil.

In experiments 4–5, model structures were revised to be the same as SiBUC: without incorporating P_2 structure, and considering gravitational drainage term in the Richards Equation, respectively. When P_2 structure is not considered, surface runoff is higher, and subsurface runoff is lower than the emulation model. The increase of surface runoff is due to lower infiltrated rainwater. As some of the rainwater has already been generated as surface runoff, the subsurface runoff becomes lower. By considering the gravitational flow in the Richards Equation, the estimated water budget is almost similar to the emulation model.

Experiment 6–7 was conducted to analyze the impacts of changing both parameters (in experiment 5) and model structures. The experiment with revised soil parameters and without considering P_2 structure shows high surface runoff and low subsurface runoff, similar to SiBUC's runoff characteristics. However, the amount of the estimated runoff is higher than SiBUC. One of the reasons is due to lower soil depth in the revised emulation model. On the other hand, revising soil parameters and incorporating gravitational drainage shows no significant change in the water budget compared to experiment 3.

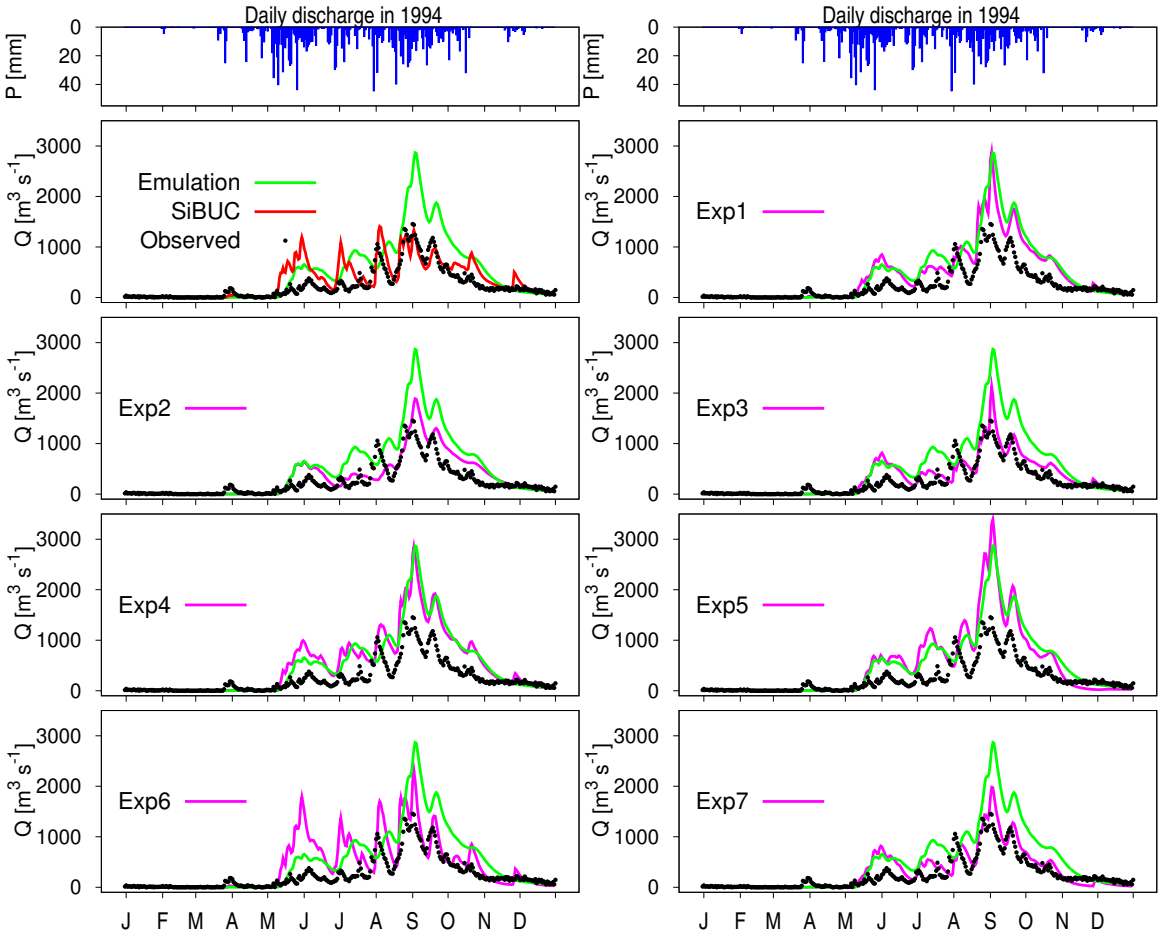

Figure 5.12: Time series of daily discharge in 1994 from observation (black dot) and simulation by SiBUC (red line), MRI–SiB emulation (green line), and revised emulation model (pink line).

5.5.4 Evaluation of streamflow simulated by revised emulation model

Figure 5.12 and Figure 5.13 shows a comparison of daily discharge between observation and each simulation in 1994 and 2011, which is considered as wet years. As mentioned earlier, the discharge by the emulation model has overestimated the observed streamflow. In contrast, the streamflow estimated by SiBUC is closer to the observed flow.

Experiment 1, conducted by changing the soil characteristics parameters, has shown an increasing surface runoff. As a result, the simulated discharge shows a slightly faster timing of increasing and recession of the hydrograph. Experiment 2, performed by increasing the soil depth, shows a reduction of the overestimated discharge by the emulation model. In the emulation model, the runoff is mostly generated as subsurface runoff. The estimated discharge decreased owing to a lower subsurface runoff because the soil takes a longer time to reach

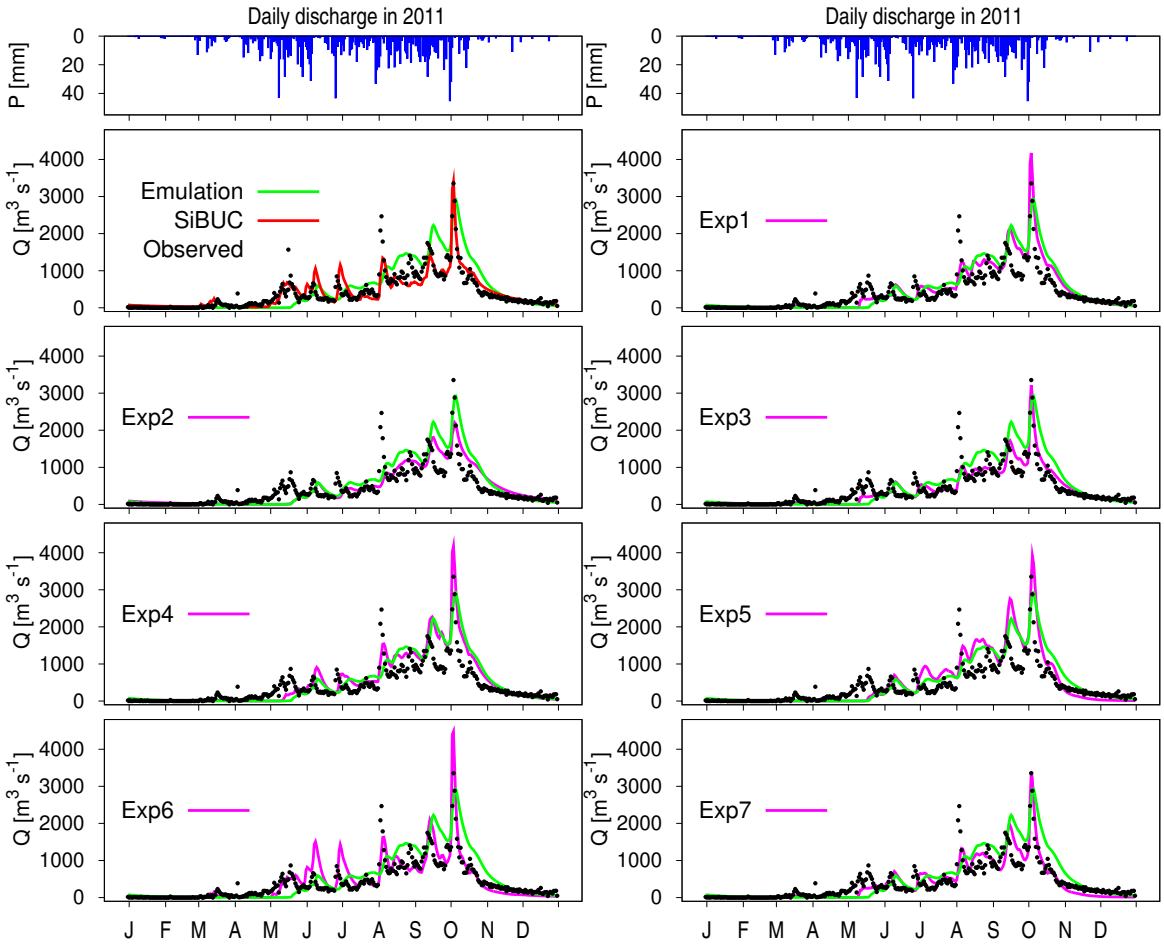

Figure 5.13: Similar to Figure 5.12 but for daily discharge in 2011.

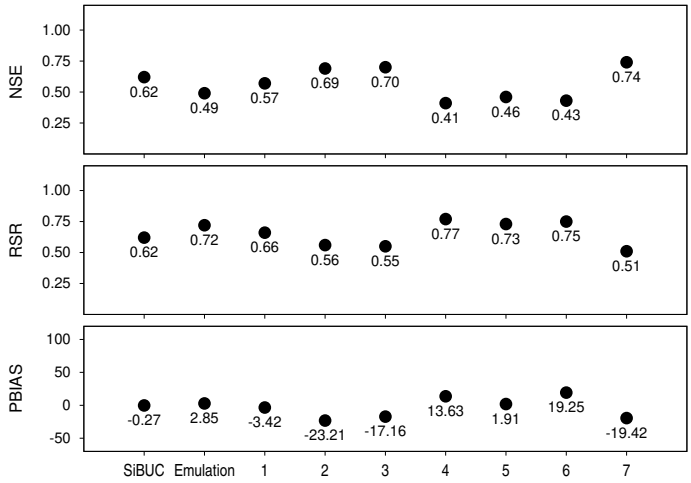

Figure 5.14: Evaluation of 30–years simulated monthly discharge by SiBUC, MRI–SiB emulation, and each experiment of revised MRI–SiB emulation model.

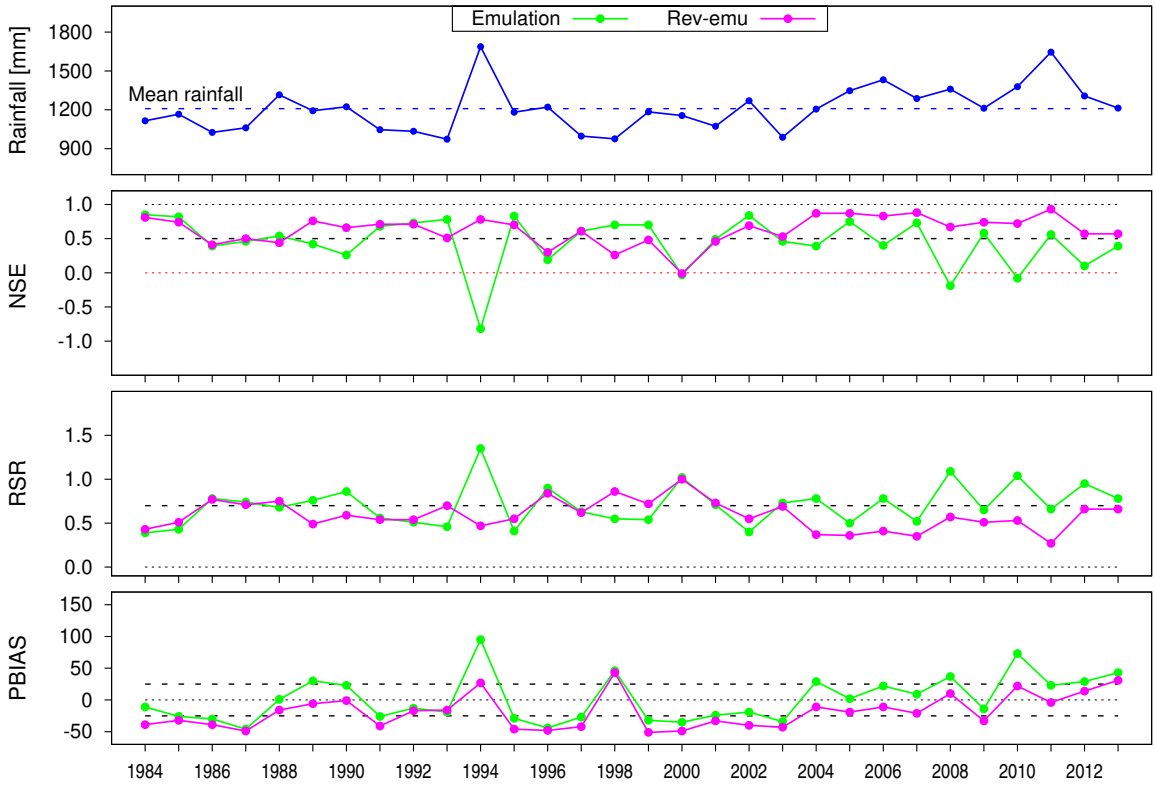

Figure 5.15: Evaluation of simulated monthly discharge in each year by MRI–SiB emulation (green line) and revised emulation model (pink line).

saturation in a deeper soil depth. Experiment 3, carried out by both revised soil characteristics parameters and soil depth, shows a closer reproducibility of discharge than the emulation model.

By neglecting P_2 structure, in experiment 4, the estimated discharge is similar to the emulation model. However, the overestimated discharge at the beginning of rainy seasons on May to June is worse in this experiment. Experiment 5 was performed by considering gravitational drainage for calculating soil–water flow. Even though the estimated water budget components are similar to the emulation model, the simulated discharge is a slightly different. In particular, the discharge by experiment 5 tends to increase and decrease more quickly than the emulation model.

In experiment 6, the soil parameters were revised to be the same as experiment 3, and P_2 structure is neglected. It shows a good improvement in reproducing the observed discharge in the later rainy season. However, the simulated discharge in the early rainy season is worse. Among all experimental cases, experiment 7, which used revised soil parameters and consid-

Table 5.7: Settings of original and revised (experiment 7) emulation model.

Settings	Original	Revised
Soil parameters	MRI–SiB original	based on SiBUC's parameters
P_2 structure	incorporated	incorporated
Soil–water flow	$Q_{i,i+1} = K\left[\frac{\partial\psi}{\partial z}\right]$	$Q_{i,i+1} = K\left[\frac{\partial\psi}{\partial z} + 1\right]$
Subsurface runoff	$Q_3 = \sin\oslash_s K_s W_3^{2B+3} + \frac{\psi_2 - \psi_3}{D_3}$	$Q_3 = \sin\oslash_s K_s W_3^{2B+3} + \frac{\psi_2 - \psi_3}{D_3}$
Time integration method	semi–implicit	semi–implicit

ered gravitational flow for the soil–water flow calculation, seems to have the best reproducibility of the observed discharge. This experiment has shown that using soil parameters according to soil types seems to have improved the simulated discharge, particularly for this basin. Incorporating gravitational drainage for calculating the soil–water flow also seems to enhance the reproducibility of discharge.

Figure 5.14 indicates performance scores for evaluating the 30–years monthly simulated discharge for each experiment. The scores of all indices by experiment 7 are the highest among all experimental cases. Therefore, the emulation model can be revised to follow the settings of experiment 7 for improving its performance. Table 5.7 is a summary of original and revised settings of the emulation model. According to the performance ratings, the emulation model's ability to reproduce the observed flow has improved from 'unsatisfactory' to 'good' performance.

Figure 5.15 shows a comparison of evaluation scores by original settings of MRI–SiB emulation model and the revised one for each year. Figure 5.16 shows monthly discharge between MRI–SiB emulation model and the revised model. Overall, the revised settings by experiment 7 have shown a better performance than the original model. In particular, the original model shows negative NSE scores in some wet years, such as in 1994, 2008, 2010, indicating poor performance. These negative scores, in general, have been improved by the revised settings. In particular, the bias of overestimated discharge could be reduced by adopting soil parameters based on soil types and incorporating the gravitational drainage in the soil–water flows calculation.

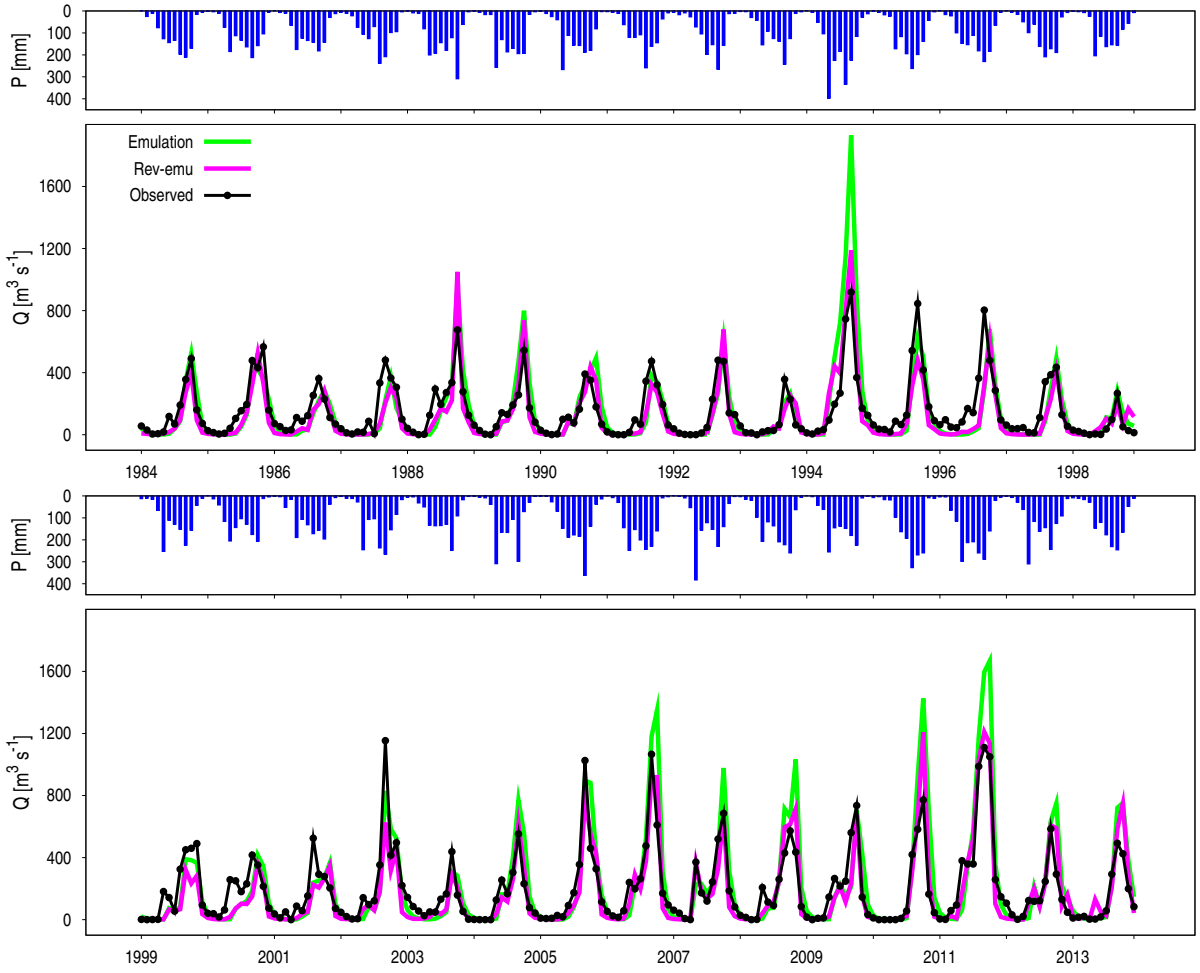

Figure 5.16: Time series of monthly discharge by MRI–SiB emulation (green line) and revised emulation model (pink line) from 1984–2013.

Table 5.8: Experimental designs for improving SiBUC.

Experiment	Revised settings
1	incorporating P_2 structure
2	reducing half depth of recharge layer
3	reducing half depth of both root zone and recharge layer
4	applying same soil depth as the revised emulation model
5	combine experiment 1 and 2
6	combine experiment 1 and 3
7	combine experiment 1 and 4

5.6 Improvement strategies for SiBUC

5.6.1 Overview

In this analysis, improvement strategies were proposed for SiBUC to reproduce the observed streamflow, particularly in the dry years, such as 1993 and 2001. As shown earlier, SiBUC shows too high discharge due to extreme rainfall events in these years. Therefore, the improvement is proposed to reduce that overestimated flow by SiBUC.

5.6.2 Experimental designs

Figure 5.8 shows experimental designs to improve SiBUC's performance. In total, seven experiments were conducted; some of them were performed by adopting some MRI–SiB's settings. As the overestimated discharge due to high generation of surface runoff by SiBUC is the current focus, improvement is proposed to lower the surface runoff and increase the subsurface runoff by SiBUC.

Experiment 1 was conducted by incorporating P_2 structure. As surface runoff is the dominant component in SiBUC; the runoff is generated soon after soil moisture of top soil is saturated. Adopting the P_2 structure can increase infiltrated rainwater into the soil, thus can reduce the overestimated discharge.

Experiment 2–4 was performed by reducing soil depth. Current soil depth in SiBUC was set too deep, up to 12 m. A lower soil depth setting contribute to higher soil–water flow, and thus subsurface runoff increases. However, surface runoff is expected to increase because of

lower capacity of soil to store the rainwater. Experiment 2 and 3 were carried out by reducing the current depth of recharge zone (third soil layer) by half, and depth of both root zone and recharge layer (second and third layer) by half. Experiment 4 was performed by adopting the same soil depth of the revised MRI–SiB emulation model, shown in Figure 5.10. As seen, the D_2 and D_3 ranges between 0.5 m–2.5 mm, and 1.5 m–5.0 m, respectively.

Experiment 5–7 was carried out by both incorporating P_2 structure and reducing soil depth at various settings. The overestimated streamflow due to high generation of surface runoff by SiBUC maybe improved by adopting these settings, by generating lower surface runoff and more subsurface runoff.

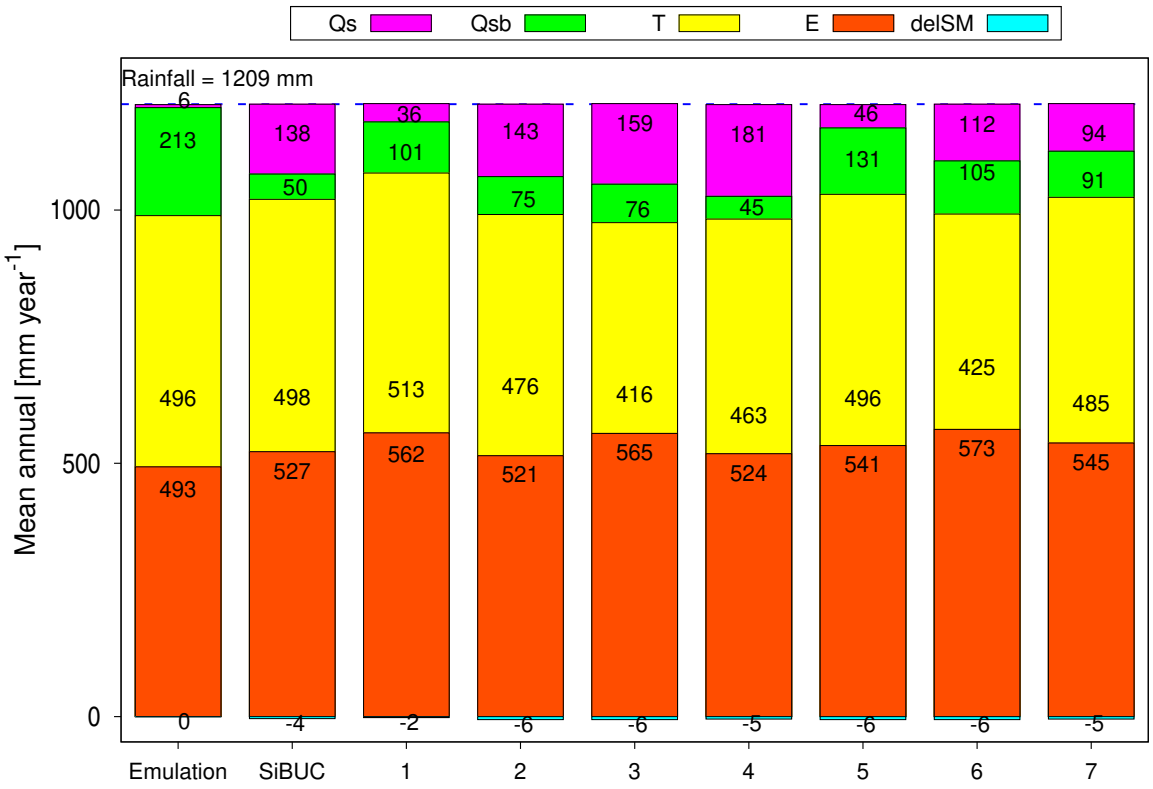

Figure 5.17: Comparison of water budget components (surface runoff (Qs), subsurface runoff (Qsb), evaporation (E), transpiration (T), and change of soil moisture (delSM)) between SiBUC, MRI–SiB emulation, and each experiment of revised SiBUC. Blue dash–line represents a 30–years-mean annual rainfall.

5.6.3 Changes of water budget by revised SiBUC

Figure 5.17 shows a comparison of water budget components between SiBUC, MRI–SiB emulation, and each experiment of revised SiBUC. Experiment 1 was performed to investigate the impact of adopting P_2 in SiBUC. By incorporating this structure, surface runoff is significantly lower, and subsurface runoff is much higher than the original SiBUC. That is reasonable because more rainwater can be infiltrated into a deeper soil layer. However, total runoff is lower, and evapotranspiration is higher than in the original setting. That might be due to affects of the soil depth, which is set quite deep, resulting in a low soil–water flow, and thus the subsurface runoff generation.

Experiment 2–4 was carried out by reducing soil depth at various settings. In experiment 2, the soil depth of the third layer was reduced by half, and in experiment 3, the soil depth of

both the second and third layers was half thinner than the original setting. In experiment 4, the soil depth of the revised emulation model was applied. As the soil depth became lower, surface runoff in both experiments was higher than SiBUC. That is because the soil has a lower capacity to store the rainwater for a thinner soil depth. In addition, the subsurface runoff is also increasing. The primary source of subsurface runoff is the saturation rate of the third soil layer. Thinner soil depth impacts a faster saturation than that in a deeper depth.

In experiments 5–7, both P_2 structure and lower depth settings were applied. Experiment 5 was performed by adopting P_2 and applying half depth of D_3. As expected, thinner depth of the third soil layer impacts on increasing subsurface runoff; it has more subsurface runoff compared to experiment 1, which was performed by only introducing P_2. The total runoff between SiBUC (control) and experiment 5 are close, but they show opposite runoff components. Experiment 6 was conducted by incorporating P_2 and applying half depth of D_2 and D_3. The reduction of surface runoff is less significant compared to experiment 5 due to a lower capacity of the second soil layer to store the water. Subsequently, the generated subsurface runoff is lower than the experiment 5 due to higher surface runoff. In experiment 7, the surface runoff is higher than experiment 5, but lower than experiment 6, and subsurface runoff is the vice versa. That is mainly due to the soil depth setting; in general, the total soil depth of this experiment is higher than experiment 6 but lower than experiment 5.

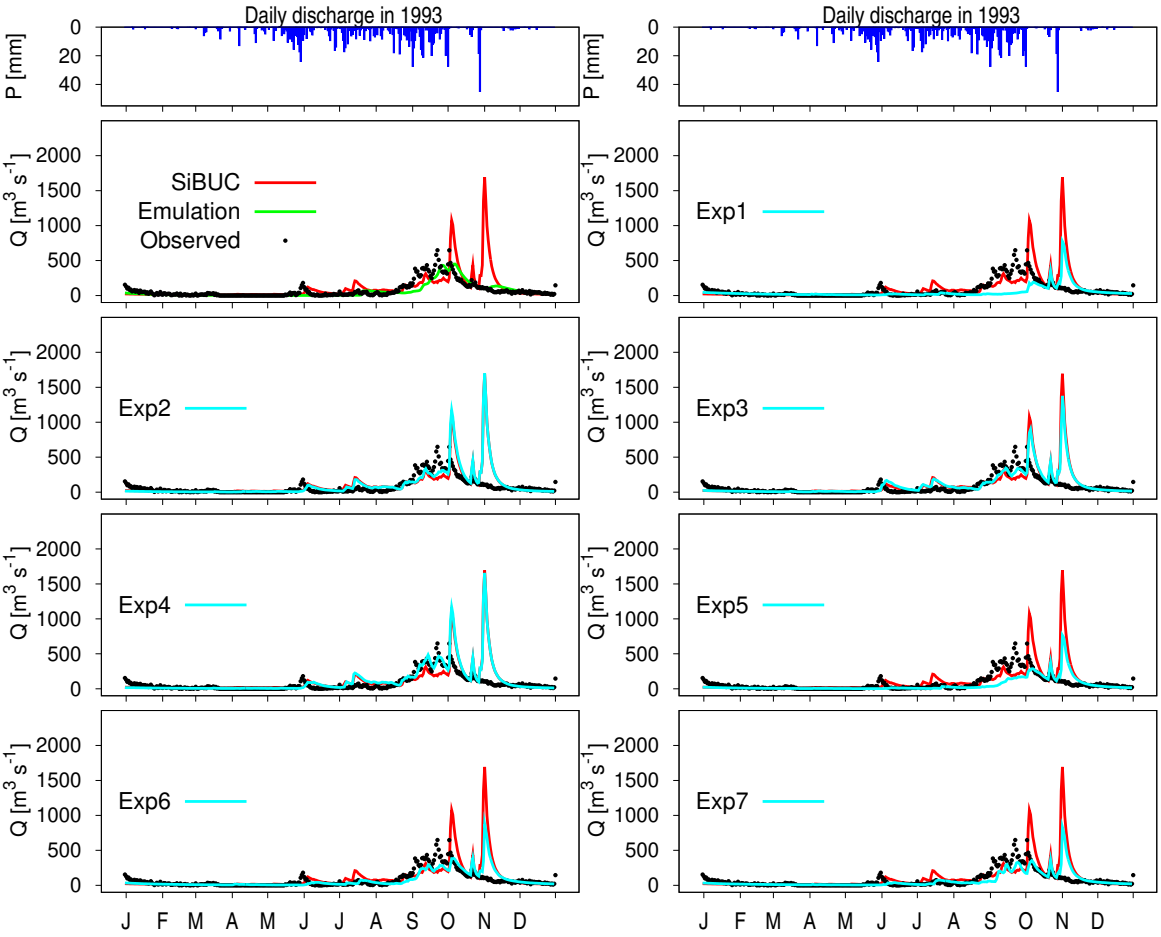

Figure 5.18: Time series of daily discharge in 1993 from observation (black dot) and simulation by SiBUC (red line), MRI–SiB emulation (green line), and revised SiBUC (light blue line).

5.6.4 Evaluation of streamflow simulated by revised SiBUC

Figure 5.18 and Figure 5.19 show a comparison of daily discharge between observation and each simulation in 1993 and 2001, which is considered as dry years. As pointed out earlier, SiBUC estimated too high discharge during extreme rainfall events. In contrast, the streamflow estimated by the emulation model is closer to the observed flow.

Simulated discharge by experiment 1, performed by adopting P_2, shows a significant reduction of the overestimated flow in the original SiBUC settings. Incorporating the P_2 structure seems to provide a good direction of improving SiBUC performance. However, the estimated volume of discharge by the experiment 1 is much lower than the original SiBUC, such as during September to November in 1993. As mentioned earlier, the decrease of the streamflow is due to lower runoff and higher evapotranspiration, cause by too deep soil depth setting, which

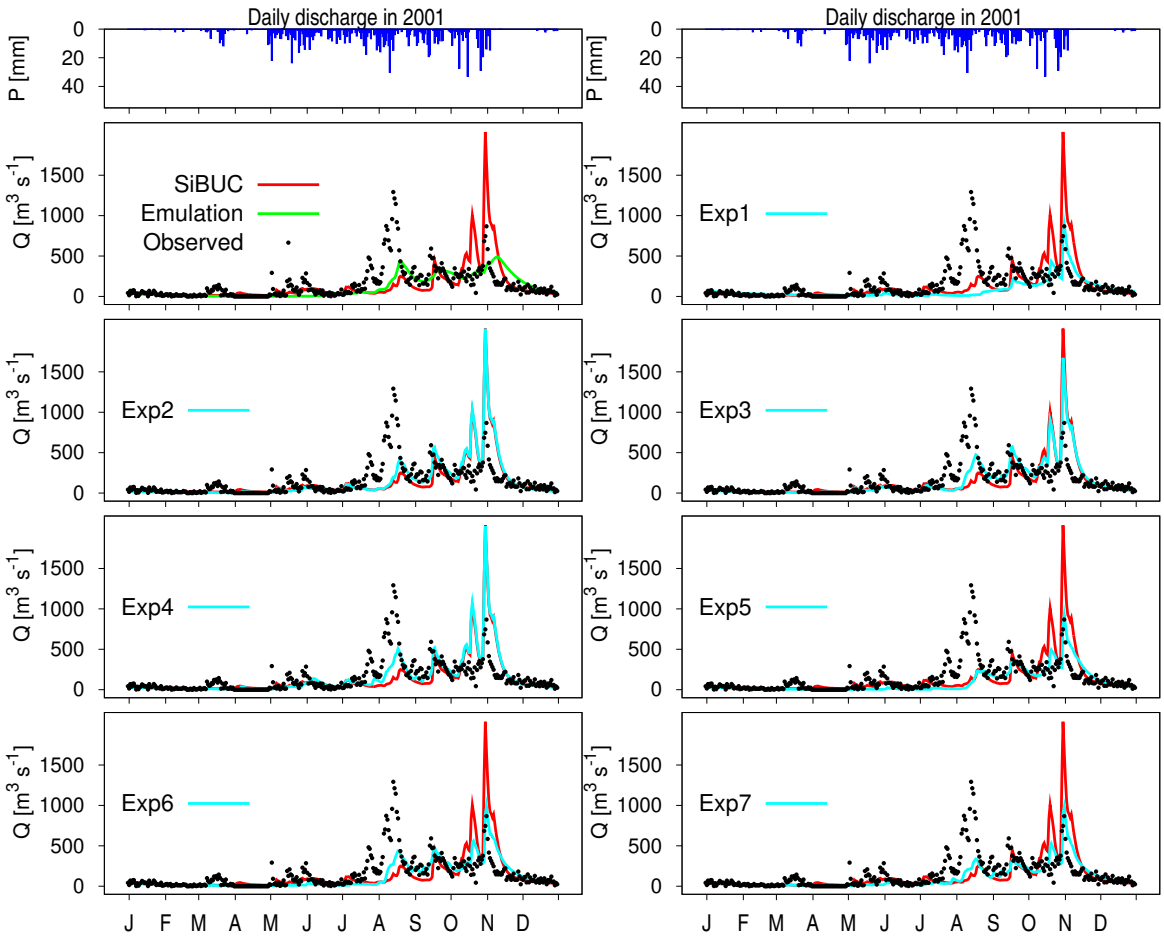

Figure 5.19: Similar to Figure 5.18 but for daily discharge in in 2001.

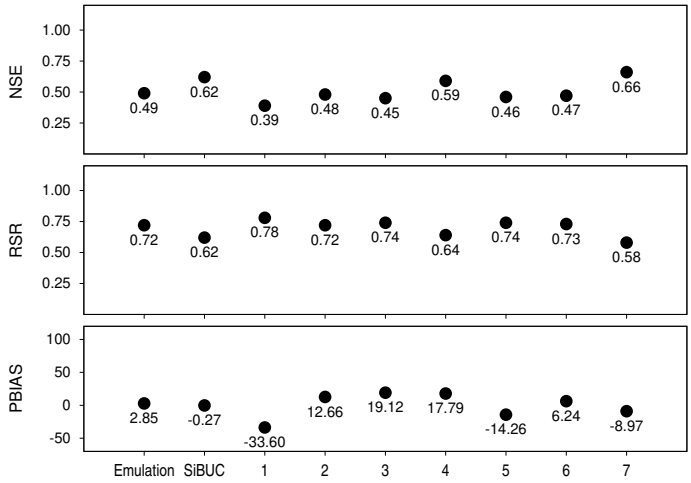

Figure 5.20: Evaluation of 30–years simulated monthly discharge by MRI–SiB emulation, SiBUC and each experiment of revised SiBUC.

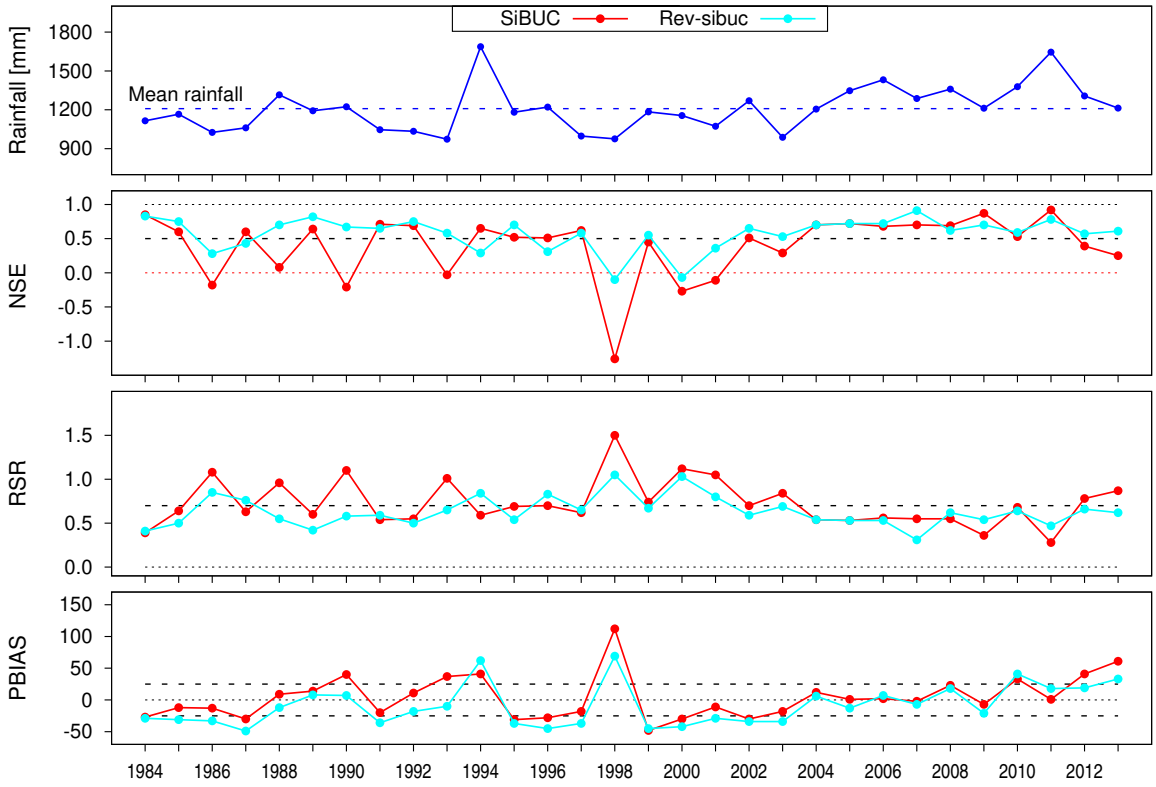

Figure 5.21: Evaluation of simulated monthly discharge in each year by SiBUC (red line) and revised SiBUC (light blue line).

contribute to a low soil–water flow, and thus the subsurface runoff generation.

Simulated discharge by experiment 2–4, carried out by lowering the soil depth, shows not significant reduction of the overestimated flow. However, the simulated flow by these experiments during August to September are closer to the observed discharge, compared to the original SiBUC which show underestimation.

Streamflow estimated by experiment 5–7, conducted by incorporating P_2 and setting a lower soil depth, shows a good performance to reproduce the observed river flow. In particular, it could reduce the overestimated discharge by SiBUC. From these results, adopting P_2 structure and reducing the soil depth provide a good direction in improving SiBUC's performance.

Figure 5.20 shows performance scores for evaluating the 30–years monthly simulated discharge for each experiment. The scores of all indices by experiment 7 are the highest among all experiments. Therefore, the settings of experiment 7 can be proposed to improve SiBUC's performance. Table 5.9 is a summary of original and revised settings of SiBUC. Based on the performance ratings, SiBUC's ability for reproducing observed discharge has improved from

Table 5.9: Settings of original and revised (experiment 7) SiBUC.

Settings	Original	Revised
Soil characteristics parameters	based on Ecoclimap	based on Ecoclimap
Soil depth	based on Ecoclimap	based on revised MRI–SiB emulation
P_2 structure	not incorporated	incorporated
Soil–water flow	$Q_{i,i+1} = K\left[\frac{\partial \psi}{\partial z} + 1\right]$	$Q_{i,i+1} = K\left[\frac{\partial \psi}{\partial z} + 1\right]$
Subsurface runoff	$Q_3 = \sin \oslash_s K_{\mathrm{s}} W_3^{2\mathrm{B}+3}$	$Q_3 = \sin \oslash_s K_{\mathrm{s}} W_3^{2\mathrm{B}+3}$
Time integration method	explicit–midpoint	explicit–midpoint

'satisfactory' to 'good' performance.

Figure 5.21 shows a comparison of evaluation scores by original settings of SiBUC and the revised model for each year. In general, revised settings by experiment 7 could improve overall performance than the original model. In particular, it improved most of the negative NSE to positive scores, indicating acceptable performance, such as in 1986, 1988, 1990, etc.

Figure 5.22 shows a comparison of monthly discharge simulated by SiBUC and revised SiBUC. As seen, in general, the overestimated peak discharge by original SiBUC could be reduced by the revised setting (experiment 7).

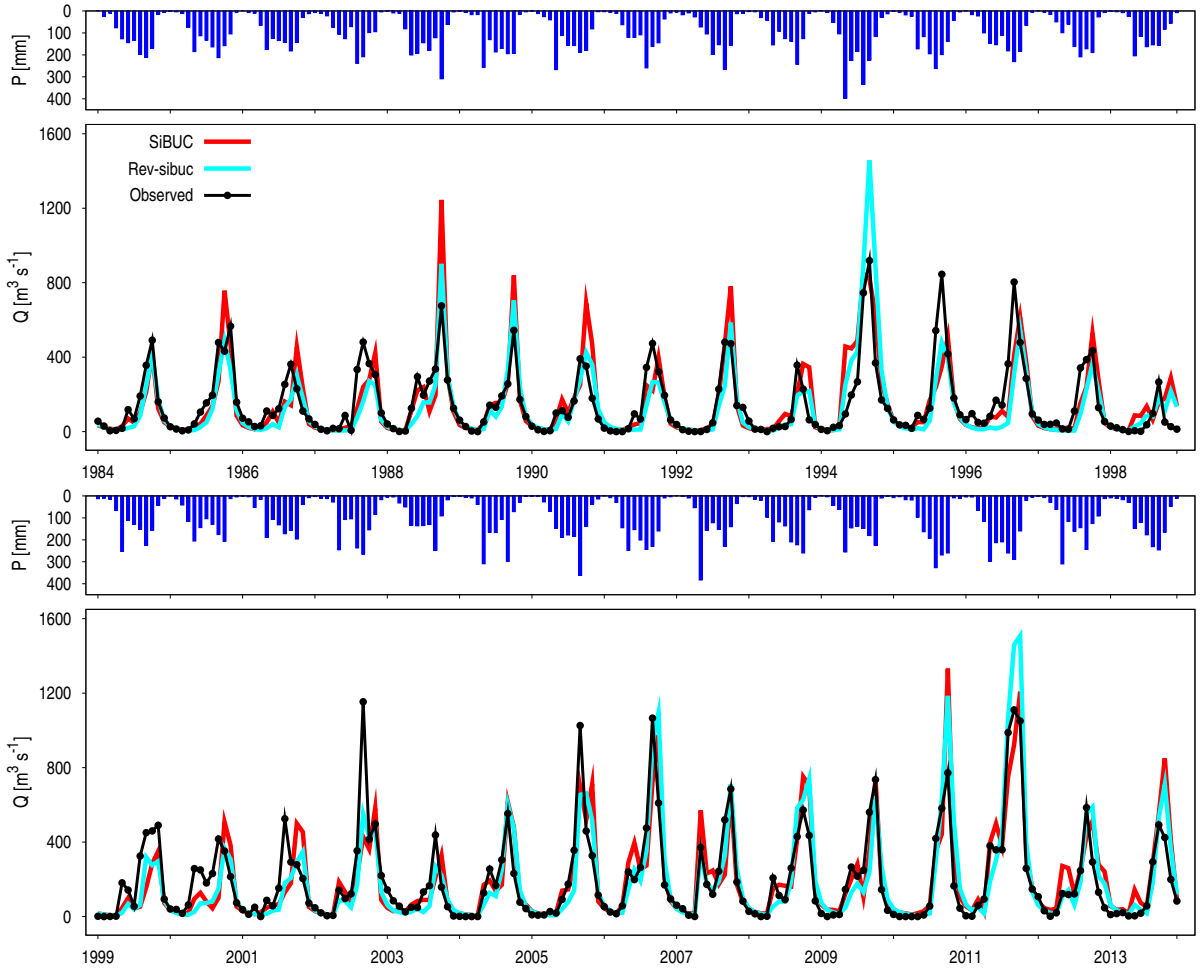

Figure 5.22: Time series of monthly discharge by SiBUC (red line) and revised SiBUC (light blue line) from 1984–2013.

5.7 Discussion

In this study, improvement strategies for SiBUC and MRI–SiB emulation models have been proposed for their reproducibility of observed discharge. The proposed improvement has shown a better reproducibility of observed streamflow by both LSMs compared to their original settings. However, there are still limitations to the current proposals.

First, this study utilized the emulation of the MRI–SiB model to improve the MRI–SiB. The developed emulation model has shown an excellent performance to reproduce runoff and river discharge by the MRI–SiB. However, it tended to overestimate MRI–SiB's runoff and the simulated streamflow. The bias shown by the emulation model in this study might also come due to the different performance of the emulation model and the original MRI–SiB. Therefore, further analysis is required to confirm the impacts of the proposed improvement in the original MRI–SiB embedded in the climate models (MRI–AGCM 3.2S and NHRCM).

Second, the sensitivity analysis for the improvement proposals in this study was only applied to the Thailand region. Consequently, the results might be different if the model is applied in the river basin of other regions or climate conditions.

Third, improvement for SiBUC has been proposed only to reduce the overestimation of peak flow, particularly during high–intense rainfall. Still, SiBUC shows some weakness in reproducing observed flow. For example, it failed to reproduce the observed discharge in most of the late rainy seasons, from August to October (such as in 2001). Numerous experiments have been done by changing soil depth in SiBUC to improve its performance, but still, no better result than this study has shown can be achieved at the moment. It is thought that changing parameters only may not be enough to have a robust performance of both LSMs. Therefore, future studies should focus on improving the runoff generation schemes, particularly on the model structures, such as to include lateral flow or other types of preferential flow.

5.8 Conclusions

In this study, the performance of two LSMs: SiBUC and MRI–SiB emulation model, was evaluated for their reproducibility of long–term observed river discharge. Both LSMs were forced by observed rainfall and atmospheric reanalysis data. They were simulated for 30 years. Based on performance ratings, in general, SiBUC showed a better performance than the emulation model on reproducing observed monthly flow. However, their ability differed depending on the rainfall amount. SiBUC tended to have a better reproducibility in wet years. However, it estimated too high rainfall during extreme rainfall events. On the other hand, the emulation model could well reproduce the observed discharge during heavy rainfall. Yet, it tended to overestimate observed flow in the wet years.

As the advantages of one model are the limitations of another model, improvement strategies were proposed by adopting settings of one model to another model. In particular, the emulation model was improved by adopting SiBUC's soil parameters and including gravitational drainage. SiBUC's performance became better when P_2 structure of MRI–SiB was adopted, and the soil depth was reduced. Based on these proposals, all LSMs have improved to perform well in reproducing the long-term observed discharge.

Chapter 6

Conclusions

This study aimed to evaluate the runoff generation schemes in LSMs and propose strategies to improve their reproductions of long–term observed streamflow. The two LSMs utilized in this study were the Simple Biosphere including Urban Canopy (SiBUC) and the Meteorological Research Institute–Simple Biosphere Model (MRI–SiB). Numerical experiments for both LSMs were conducted in the upper part of the Ping River Basin in northern Thailand.

First, the applicability of runoff generated by both LSMs was investigated to streamflow simulation. Comparisons of the water budget showed that the SiBUC tended to estimate higher evapotranspiration and lower runoff than the MRI-SiB. Each LSM generated different runoff characteristics. The SiBUC estimated higher surface runoff and lower subsurface runoff than the MRI–SiB. Subsurface runoff was the dominant runoff component in the MRI–SiB. Different runoff characteristics impact the simulated streamflow in differing ways. The peak discharge determined by the SiBUC, attributed primarily to surface runoff generation, was produced soon after the peak rainfall. In contrast, peak flow in the MRI–SiB showed a significant delay compared to peak rainfall. As the MRI–SiB is dominated by subsurface runoff, rainwater first infiltrates into the soil before it flows into a river, resulting in long lag times. In general, the discharge simulated by the SiBUC was of a higher volume than that simulated by the MRI–SiB because of the higher estimation of runoff. This study showed that even though the same forcing data was imposed on both LSMs, the estimated runoff and simulated discharge differed for each LSM.

Next, the runoff generation schemes in the two LSMs were analyzed in detail to determine the reasons for the different runoff characteristics. We investigated which settings were treated differently in the two land surface models (LSMs). The different settings between both LSMs were adopted in SiBUC to evaluate their impacts on runoff generation. SiBUC that incorporated

MRI–SiB's settings is called as MRI–SiB emulation model. Our investigation identified some different settings in both LSMs that mainly affected the runoff generation and the simulated discharge. We found that by adopting the same soil parameters, model structures, and time integration method for soil schemes, the runoff characteristics from the MRI–SiB can be emulated well by the SiBUC. The findings of this study provide insights into identifying the sources of runoff uncertainty in LSMs.

Finally, the simulated discharge forced by the runoff from both LSMs was evaluated by comparing it with 30 years of observed streamflow. The two LSMs were forced by the observed rainfall and reanalysis of atmospheric data. For long–term evaluation, the discharge simulated by the SiBUC performed better than the flow estimated by the MRI-SiB to reproduce the monthly observed discharge. In particular, the SiBUC performed well at reproducing the discharge observed during wet years (when annual rainfall is higher than the climatological mean). In contrast, the discharge simulated by the MRI–SiB was better than the flow estimated by the SiBUC during dry years (when annual rainfall is lower than the climatological mean). Our analysis shows that using some SiBUC settings in the MRI–SiB, and vice versa, could enhance the performance of each model at reproducing the long–term observed river flow. However, some limitation still exists in the two LSMs for reproducing the observed discharge. Thefore, future studies should focus on improving the runoff generation schemes, particularly on the model structures, such as to include lateral flow or other types of preferential flow.

Bibliography

An, H. and Noh, S. J.: High–order averaging method of hydraulic conductivity for accurate soil moisture modelling, *Journal of Hydrology*, Vol. 516, pp. 119–130, 2014.

Balsamo G., Beljaars, A., Scipal, K., Viterbo, P., van den Hurk, B., Hirschi, M., and Betts, A. K.: A revised hydrology for the ecmwf model: verification from field site to terrestrial water storage and impact in the integrated forecast system, *Journal of Hydrometeorology*, Vol. 10, No. 623–643, 2009.

Best, M. J., Pryor, M., Clark, D. B., Rooney, G. G., Essery, R. L. H., Mnard, C. B., Edwards, J. M., Hendry, M. A., Porson, A., Gedney, N., Mercado, L. M., Sitch, S., Blyth, E., Boucher, O., Cox, P. M., Grimmond, C. S. B., and Harding, R. J.: The Joint UK Land Environment Simulator (JULES), model description : Part 1: Energy and water fluxes, *Geoscientific Model Development*, Vol. 4, No. 677–699, 2011.

Chilkoti, V., Bolisetti, T., and Balachandar, R.: Diagnostic Evaluation of Hydrologic Models Employing Flow Duration Curve, *Journal of Hydrological Engineering*, Vol. 24, No. 6, 2019.

Clapp, R. B., and Hornberger, G. M.: Empirical Equations for Some Soil Hydraulic Properties, *Water Resources Research*, Vol. 14, No. 4, pp. 601–604, 1978.

Cosbyg, B. J., Hornberger, M., Clapp, B., and Ginn, T. R.: A StatisticaEl xplorationo f the Relationshipos f Soil Moisture Characteristicsto the PhysicalP ropertieso f Soils–, *Water Resources Research*, Vol. 20, No. 6, pp. 682–690, 1984.

Cox, P. M., Betts, R. A., Bunton, C. B., Essery, R. L. H., Rowntree, P. R., and Smith, J.: The impact of new land surface physics on the GCM simulation of climate and climate sensitivity, *Climate Dynamics*, Vol. 15, pp. 183–203, 1999.

Dai, Y., Zeng, X., Dickinson, R. E, Baker, I., Bonan, G. B., Michael, G. B, Denning, A. S., Dirmeyer, P. A., Houser, P. R., Niu, G., Oleson, K. W., Schlosser, C. A., and Yang, Z. L.: The Community Land Model Coupled, *Bulletin of the American Meteorological Society*, Vol. 84, Issue 8, pp. 1013–1024, 2003.

Davis, R. O. E., and Bennett, H. H.: Grouping of soils on the basis of mechanical analysis, *United States Department of Agriculture*, 1927.

Dickinson, RE.: Land-surface processes and climate, surface albedos and energy balance, *Advances in Geophysics*, Vol. 25, pp. 305–353, 1983.

Dirmeyer P. A., Dolman, A. J., Sato N.: The pilot phase of the global soil wetness project. , *Bulletin of the American Meteorological Society*, Vol. 80, pp. 851–878, 1999.

Essery, R., Best, M., Betts, R. A., Cox, P., and Taylor, C. M.: Explicit representation of subgrid heterogeneity in a GCM land surface scheme, *Journal of Hydrometeorology*, Vol. 4, pp. 530–543, 2003.

Loveland, T. R., Reed, B. C., Brown, J. F., Ohlen, D. O., Zhu, Z., Yang, L., and Merchant, J. W.: Development of a global land cover characteristics database and IGBP DISCover from 1 km AVHRR data, *International Journal of Remote Sensing*, Vol. 21, Issue 6–7, pp. 1303–1330, 2000.

Funk, C., Peterson, P., Landsfeld, M., Pedreros, D., Verdin, J., Shukla, S., Husak, G., Rowland, J., Harrison, L., Hoell, A., and Michaelsen, J.: The climate hazards infrared precipitation with stations–a new environmental record for monitoring extremes, *Scientific Data 2*, 150066, 2015.

Falloon, P., Betts, R., Wiltshire, A., Dankers, R., Mathison, C., McNeall, D., Bates, P., and Trigg, M.: Validation of river flows in HadGEM1 and HadCM3 with the TRIP river flow model, *Journal of Hydrometeorology*, Vol. 99, pp. 685–695, 2011.

Gale, E. L. and Saunders, M. A.: The 2011 Thailand flood: climate causes and return periods, *Weather*, Vol. 68, Issue 9, pp. 233–237, 2013.

Getirana, A., Boone, A., Peugeot, C., and ALMIP2 WORKING GROUP: Streamflows over a West African Basin from the ALMIP2 Model Ensemble, *Journal of Hydrometeorology*, 2017.

Gordon,C., Cooper, C., Senior, C. A., Banks, H., Gregory, J. M., Johns, T. C., Mitchell, J. F. B., and Wood, R. A.: The simulation of SST, sea ice extents and ocean heat transports in a version of the Hadley Centre coupled model without flux adjustments, *Climate Dynamics*, Vol. 16, pp. 147–168, 2000.

Graham, L. P., and Bergstrom, S.: Land surface modeling in hydrology and meteorology–lessons learn from the Baltic Basin, *Hydrology and Earth System Sciences*, Vol. 4, No. 1, pp. 13–22, 2000.

Henderson–Sellers A, Pitman AJ, Love PK, Irannejad P, Chen T.: The project for intercom-

parison of land surface parameterisation schemes (PILPS) phases 2 and 3, *Bulletin of the American Meteorological Society*, Vol. 76, pp. 489–503, 1995.

Hirabayashi, Y., Mahendran, R., Koirala, S., Konoshima, L., Yamazaki, D., Watanabe, S., Kim, H., and Kanae, S.: Global flood risk under climate change, *Nature Climate Change*, Vol. 3, pp. 816–821, 2013.

Hirai, M., and Ohizumi, M.: Development of a new land–surface model for JMA-GSM, *Bulletin of the American Meteorological Society*, Vol. 85, pp. 2737–2743, 2004.

Hirai, M., Sakashita, T., Kitagawa, H., Tsuyuki, T., Hosaka, M., Oh'izumi, M.: Development and Validation of a New Land Surface Model for JMA ' s Operational Global Model Using the CEOP Observation Dataset, *Journal of The Meteorological Society of Japan*, Vol. 85A, pp. 1–24, 2007.

Hunukumbura, P. B. and Tachikawa, Y.: River Discharge Projection under Climate Change in the Chao Phraya River Basin, Thailand, Using the MRI–GCM3.1S Dataset, *Journal of The Meteorological Society of Japan*, Vol. 90A, pp. 137–150, 2012.

Nakicenovic, N. and Swart, R. (Eds.): Special Report on Emissions Scenarios, IPCC, *Cambridge University Press*, Cambridge, UK, pp. 570, 2000.

IPCC, Intergovernmental Panel on Climate Change Climate Change: Climate Change 2014: Synthesis Report. Contribution of Working Groups I, II and III to the Fifth Assessment Report of the Intergovernmental Panel on Climate Change [Core Writing Team, R.K. Pachauri and L.A. Meyer (eds.)], *IPCC*, Geneva, Switzerland, 151 pp, 2014.

IPCC, Intergovernmental Panel on Climate Change Climate Change [Masson-Delmotte, V., P. Zhai, A. Pirani, S.L. Connors, C. Pean, S. Berger, N. Caud, Y. Chen, L. Goldfarb, M.I. Gomis, M. Huang, K. Leitzell, E. Lonnoy, J.B.R. Matthews, T.K. Maycock, T. Waterfield, O. Yelekci, R. Yu, and B. Zhou (eds.)]: The Physical Science Basis. Contribution of Working Group I to the Sixth Assessment Report of the Intergovernmental Panel on Climate Change, *Cambridge University Press*, In Press, 2021.

Kobayashi, C., and Iwasaki, T.: Brewer-Dobson circulation diagnosed from JRA–55, *Journal of Geophysical Research–Atmospheres*, Vol. 121, pp. 1493–1510, 2016.

Komori, D., Nakamura, S., Kiguchi, M., Nishijima, A., Yamazaki, D., Suzuki, S., Kawasaki, A., Oki, K., Oki, T.: Characteristics of the 2011 Chao Phraya River flood in Central Thailand, *Hydrological Research Letters*, Vol. 6, pp. 41–46, 2012.

Koster, R. D, and Milly, P. C. D.: Brewer-Dobson circulation diagnosed from JRA–55, *Journal*

of Climate, Vol. 10, pp. 1578–1591, 1996.

Kotsuki, S., Tanaka, K., and Komori, D.: Long–term water balance analysis using different precipitation products in Upper Chao Phraya River, Thailand, *Proceedings of the 6th conference of Asia Pacific Association of Hydrology and Water Resources (APWH)*, pp. 6, 2013.

Kyoto University Department of Civil and Earth Resources Engineering Hydrology and Water Resources Research Laboratory: 1K-FRM/1K-DHM, http://hywr.kuciv.kyoto–u.ac.jp/products/1K-DHM/1K–DHM.html [Access: December 8, 2021]

Lehner, B., Verdin, K., and Jarvis, A.: New global hydrography derived from spaceborne elevation data, *Eos, Transactions, AGU*, Vol. 89(10), pp. 93–94, 2008.

Myneni, R., Yuri, K., Park, T.: MOD15A3 MODIS/Combined Terra+Aqua Leaf Area Index/FPAR Daily L4 Global 1km SIN Grid, *Boston University and MODAPS SIPS - NASA*, NASA LP DAAC, 2015.

Manee, D., Tachikawa, Y., Ichikawa, Y., and Yorozu, K.: River discharge and reservoir operation assessment under a changing climate at the Sirikit Reservoir, *THA2017, International Conference on Water Management and Climate Change Towards Asia's Water-Energy-Food Nexus*, TA–003, 2017.

Manabe, S.: Climate and the ocean circulation' 1. The atmospheric circulation and the hydrology of the earth's surface, *Monthly Weather Review*, Vol. 97, No. 11, pp. 739–774, 1969.

Martin, G. M., Ringer, M. A., Pope, V. D., Jones, A., Dearden, C., and Hinton, T. J.: The physical properties of the atmosphere in the new Hadley Centre Global Environmental Model (HadGEM1).Part 1: Model description and global climatology *Journal of Climate*, Vol. 19, pp. 1274?-1301, 2006.

Masson, V., Champeaux, J.L., Chauvin, F., Meriguet, C., Pigeon, G.: A Global Database of Land Surface Parameters at 1-km Resolution in Meteorological and Climate Models, *Journal of Climate*, Vol. 16, No. 9, pp. 1261–1282, 2003.

Mizuta, R., Yoshimura, H., Murakami, H., Msatsueda, M., Endo, H., Ose, T., Kamiguchi, K. , Hosaka, M., Sugi, M., Yukimoto, S., Kusunoki, S., and Kitoh, A.: Climate simulations using MRI-AGCM with 20–km grid, *Journal of Meteorological Society Japan*, Vol. 90A, pp. 235–260, 2012.

Moriasi, D. N., Arnold, J. G., VanLiew, M. W., Bingner, R. L., Harmel, R. D., and Veith, T. L.: Model evaluation guidelines for systematic quantification of accuracy in watershed simula-

tions, *American Society of Agricultural and Biological Engineers*, Vol. 50(3), pp. 885–900, 2007.

Mueller, A., Dutra, E, Cloke, H., Verhoef, A., Balsamo, G., and Pappenberger, F.: Water infiltration and redistribution in Land Surface Models, *Technical Memorandum European Centre for Medium-Range Weather Forecast*, 2016.

Nakaegawa, T., and Sugi, M: Impact of soil moisture movement schemes in a SVATS on global climate of AGCM, *IAHS Red Book*, Vol. 270, pp. 47–51, 2001.

Nash, J.E and Sutcliffe, J. V.: River flow forecasting through conceptual models part I–A discussion of principles*, *Journal of Hydrology*, Vol. 10, pp. 282–290, 1970.

Niu, G.-Y., Yang, Z.-L, Mitchell, K. E., Chen, F., Ek, M. B., Barlage, M., Kumar, A., Manning, K., Niyogi, D., Rosero, E., Tewari, M., Xia, Y.: The community Noah land surface model with multiparameterization options (Noah–MP): 1. Model description and evaluation with local scale measurements, *Journal of Geophyscial Research–Atmospheres*, Vol. 116, D12109, 2011.

Nohara, D., Kitoh, A., Hosaka, M., Oki, T.: Impact of Climate Change on River Discharge Projected by Multimodel Ensemble, *Journal of Hydrometeorology*, Vol. 7, pp. 1076–1089, 2006.

Oki, T. and Sud, Y. C.: Design of Total Runoff Integrating Pathways (TRIP)–A global river channel network, *Earth Interactions*, Vol. 2, pp. 1–37, 1998.

Oki, T., Nishimura, T., and Dirmeryer, P.: Assessment of Annual Runoff from Land Surface Models Using Total Runoff Integrating Pathways (TRIP), *Journal of the Meteorological Society of Japan*, Vol. 77, No. 1B, pp. 235–255, 1999.

Pitman, A. J., and Coauthors: Project for Intercomparison of Land–surface Parameterization Schemes, Results from offline control simulations (Phase 1a): *International GEWEX Project Office Publication Series*, No. 7, GEWEX/WCRP, pp. 47, 1993.

Pitman, A. J.: Review the evolution of, and revolution in, land surface schemes designed for climate models: *International Journal of Climatology*, Vol. 23, pp. 475–510, 2003.

Sasaki, H., Kurihara, K., Takayabu, I., and Uchiyama, T.: Preliminary experiments of reproducing the present climate using the non-hydrostatic regional climate model, *SOLA*, Vol. 4, pp. 025–028, 2008.

Sasaki, H., Murata, A., Hanafusa, M., Oh'izumi, M., and Kurihara, K.: Reproducibility of present climate in a non-hydrostatic regional climate model nested within an atmosphere general

circulation model, *SOLA*, Vol. 7, pp. 173–176, 2011.

Sato, N., Sellers, P. J., Randall, D. A., Schneider, E. K., Shukla, J., Kinter III. J. L., Hou, Y–T., and Albertazzi, E.: Effects of implementing the simple biosphere model in a general circulation model, *Journal of the Atmospheric Sciences*, Vol. 46, no.18, pp. 2757–2782, 1989.

Sellers, P. J., Mintz, Y., Sud, Y. C., and Dalcher, A.: A simple biosphere model (SiB) for use within general circulation models, *Journal of the Atmosphere Science*, Vol. 43, No. 6, pp. 505–531, 1986.

Sellers, P. J.: Biophysical models of land surface processes, *In Climate System Modelling*, Trenberth KE (ed.). Cambridge University, Press, 1992.

Sellers, P. J., Dickinson, R. E., Randall, D. A., Denning, A. S., Betts, A. K., Hall, F. G., Berry, J. A., Collatz, G. J., Mooney, H. A., Nobre, C. A., Sato, N., Field, C. B., and Henderson-Sellers, A.: Modeling the exchanges of energy, water, and carbon between continents and the atmosphere, *Science*, Vol. 275, Issue 5299, pp. 502–509, 1997.

Simunek, J., van Genuchten, M. Th. and Sejna, M.: Development and applications of the HYDRUS and STANMOD software packages, and related codes, *Vadose Zone Journal*, Vol. 7, No. 2, pp. 782–797, 2008.

Singh, J., H. V. Knapp, and M. Demissie: Hydrologic modeling of the Iroquois River watershed using HSPF and SWAT, *Illinois State Water Survey*, CR 2004–08, 2004.

Tanaka, K.: Development of the new land surface scheme SiBUC commonly applicable to basin water management and numerical weathe prediction model, *doctoral dissertation*, Kyoto University, 2005.

Takata, K., Emori, S., and Watanabe, T.: Development of the minimal advanced treatments of surface interaction and runoff, *Global Planet Change*, Vol. 38, pp. 209–222, 2003.

Takata, K. and Hanasaki, N.: Investigating runoff sensitivity in the land-surface model MATSIRO to reduce low runoff bias, *Journal of Meteorological Society Japan*, Vol. 99 , No. 3 pp. 685–695, 2021.

Thai Meteorological Department: Annual weather summary of Thailand in 2011, http://www.tmd.go.th/programs

Tinumbang, A.F.A, Yorozu, K., Tachikawa, Y., Ichikawa, Y., Sasaki, H., and Nakaegawa, T.: Analysis of runoff characteristics generated by land surface models and their impacts on river discharge, *Journal of Japan Society of Civil Engineers*, Ser. B1 (Hydraulic Engineering),

Vol. 75, No. 2, pp. I_271–I_276, 2019.

Tinumbang, A.F.A, Yorozu, K., Tachikawa, Y., Ichikawa, Y.: Analysis of the applicability of nhrcm 2km output data and a distributed hydrologic model for river discharge estimation, *Proceedings of the 8th International Conference on Water Resources and Environment Research*, pp. 200–203, 2019a.

Tinumbang, A.F.A, Yorozu, K., Tachikawa, Y., Ichikawa, Y., Sasaki, H., and Nakaegawa, T.: Impacts of model structures and soil parameters on runoff characteristics in land surface models, *Journal of Japan Society of Civil Engineers*, Ser. B1 (Hydraulic Engineering), Vol. 76, No. 2, pp. I_217–I_222, 2020.

Tinumbang, A.F.A, Yorozu, K., Tachikawa, Y., Ichikawa, Y., Sasaki, H., and Nakaegawa, T.: Investigating the impacts of different time integration methods in land surface models on runoff estimation, *Journal of Japan Society of Civil Engineers*, Ser. B1 (Hydraulic Engineering), Vol. 77, No. 2, pp. I_271–I_276, 2021.

van Dam, J. C. and Feddes, R. A.: Numerical simulation of infiltration, evaporation and shallow groundwater levels with the Richards equation, *Journal of JHydrology* (Amsterdam), Vol. 233, pp. 72–85, 2000.

Xue Y, Sellers PJ, Kinter JL, Shukla J.: A simplified biosphere model for climate studies, *Journal of Climate*, Ser. B1 (Hydraulic Engineering), Vol. 4, pp. 345–364, 1991.

Yorozu, K. and Tachikawa, Y.: The effect on river discharge estimation by considering an interaction between land surface process and river routing process, *Proceedings of International Association of Hydrological Sciences*, Vol. 369, pp. 81–86, 2015.

Yorozu, K., Kurosaki, N., Ichikawa, Y., Kim, S., and Tachikawa, Y.,: A study on long-term river discharge data generation by distributed hydrologic model and recombination atmospheric data, *Journal of Japan Society of Civil Engineers*, Ser. B1 (Hydraulic Engineering), Vol. 74, pp. I_127–I_132, 2018 (in Japanese).